

**Characterization of effective hydraulic properties of  
unsaturated porous media using spectral induced  
polarization (SIP)**

**Dissertation**

**zur**

**Erlangung des Doktorgrades (Dr. rer. nat.)**

**der**

**Mathematisch-Naturwissenschaftlichen Fakultät**

**der**

**Rheinischen Friedrich-Wilhelms-Universität Bonn**

**vorgelegt von**

**Katrin Breede**

**aus**

**Hann. Münden, Deutschland**

**Bonn (September, 2012)**

**Angefertigt mit Genehmigung der Mathematisch-Naturwissenschaftlichen Fakultät der  
Rheinischen Friedrich-Wilhelms-Universität Bonn**

1. Gutachter: Prof. Dr. A. Kemna

2. Gutachter: Prof. Dr. H. Vereecken

Tag der Promotion: 11.12.2012

Jahr der Veröffentlichung: 2013

## Acknowledgements

I firstly thank my promoter Prof. Andreas Kemna, Chairman of Applied Geophysics, University of Bonn, and Prof. Harry Vereecken, head of IBG-3, Agrosphere, Forschungszentrum Jülich for the opportunity and support to do this research.

This Ph.D. project would have let to nowhere without the support of Dr. Johann Alexander Huisman.

I'm also very grateful for the support from the SIP workgroup of the IBG-3 institute. Our meetings and numerous discussions helped me to overcome some problems.

I would like to thank all the people who were involved in the set-up of the laboratory equipment as well as the measurements and analysis of the data. I especially thank Odilia Esser who helped me with the experiments and for many hours of discussion about the experiments and measurement results.

The support of Dr. Egon Zimmermann, Sander Huisman, Jürgen Höltkemeier, Dr. Roy Kasteel, Andreas Kemna, Ferdinand Engels, and the staff of the IBG workshop was crucial for constructing the measurement cells.

I'm thankful to Egon Zimmermann and Joachim Berwix for providing the electrical impedance spectrometer and the measurement software. Whenever there was a problem with the device or the software I could be sure that they would help me and solve the problem very quickly.

I thank Ansgar Weuthen and Jürgen Höltkemeier for the setup of the Multi Step Outflow device and programming the necessary software. Occurring problems with the equipment were quickly solved by both of them so that the experiments could proceed without greater interruptions.

I'm thankful to Prof. Dr. Jan Vanderborght for supporting me with help from the technical staff for the set-up of the Multi Step Outflow equipment.

I would like to thank Anke Langen for measurements of the water content.

I'm very grateful to Prof. Dr. Gioia Falcone who allowed me to work further on my Ph.D. thesis while I was starting my new job at the Clausthal University of Technology.

I especially thank Ansgar, Ferdi, Jutta, Odilia, Myriam and Jana for companionship.

Last but not least, a big thank-you to my husband, my family, and friends for their support and encouragement.



## Abstract

Groundwater is a life-sustaining but vulnerable resource which is endangered by contaminants. Soil acts as an important protective buffer for groundwater and, therefore, the understanding of flow and transport processes in soils is of utmost importance. However, the prediction capabilities of flow and transport models in the vadose zone are often limited due to an insufficient knowledge about the structural and textural heterogeneity of the soil. To obtain more information about soil structure, texture and heterogeneity, as well as hydraulic parameters, non-invasive electrical methods may be employed in laboratory and field-scale studies. One of the more promising electrical methods is spectral induced polarization (SIP), which measures the complex electrical conductivity in the low-frequency range from 1 mHz to 45 kHz. Recently, this method has been used to predict the saturated hydraulic conductivity of consolidated and unconsolidated porous media. To better understand the mechanisms causing polarization and to extend the range of SIP applications to the vadose zone, it is important to investigate how the SIP response is affected by water content. In addition, it might be possible to relate the SIP response to the unsaturated hydraulic conductivity. Therefore, the general aim of this thesis is the determination of effective hydraulic properties of unsaturated and unconsolidated porous media from SIP measurements.

In a first step, a laboratory measurement setup was developed that allows combined electrical and hydraulic measurements on unconsolidated porous media. The experimental design allows draining samples in various consecutive pressure steps and water outflow is automatically recorded to determine the water content. Measurements of the complex electrical conductivity are conducted using a high-accuracy electrical impedance spectrometer. Experiments were conducted on unconsolidated quartz sand and three sand-clay mixtures with 5, 10, and 20 weight-percent clay. The measured complex electrical conductivity was interpreted using a Debye decomposition approach that provides the DC resistivity, the total chargeability, and a distribution of relaxation times.

The influence of water content on electrical properties like real and imaginary part of the complex electrical conductivity, phase shift, and the parameters obtained from Debye decomposition was investigated for all four artificially mixed sediment samples. The measured resistivity magnitude and phase spectra and their dependence on water content are clearly different for each mixture. For pure sand, the phase values increased with decreasing water content over the entire frequency range and a phase peak appeared for moderate to low water content. The phase spectra of the sand-clay mixtures show the same behavior as the pure sand. In addition, a shift of the phase peak to higher frequencies with decreasing water saturation was observed for all samples. This shift suggests that relaxation time and length become smaller with decreasing water content, which is related to the smaller pores that are still saturated at lower water content.

The relationship between unsaturated hydraulic properties and SIP parameters was also investigated. The results show a clear power-law relationship between the matric potential and the peak relaxation time of the sand-clay mixtures. However, two different slopes were observed for this relationship, one for matric potentials greater than -120 cm and another one for smaller ones. The observed slope was quadratic for matric potentials  $> -120$  cm and linear for matric potentials below -120 cm. The quadratic relationship was attributed to diffusion processes, but the linear relationship indicates a hitherto unknown relaxation process. Using the empirical relationship between the relaxation time and the matric potential, respectively pore radius, and a simplified version of the Mualem-van Genuchten model, a relationship between the relaxation time and the unsaturated hydraulic conductivity was obtained. The

slope of this power-law dependence between unsaturated hydraulic conductivity and relaxation time depends on the width of the pore size distribution as expressed by the semi-empirical  $n$  parameter of the Mualem-van Genuchten model. It was concluded that the unsaturated hydraulic conductivity can be determined from spectral induced polarization using the relaxation time and additional information like the  $n$  parameter of the Mualem-van Genuchten model.

## Zusammenfassung

Grundwasser ist eine lebenserhaltende aber empfindliche Ressource, die durch Kontaminationen gefährdet ist. Boden ist ein wichtiger schützender Puffer für Grundwasser. Das Verständnis von Fließ- und Transportprozessen in Böden ist daher von besonderem Interesse. Die Vorhersagefähigkeiten von ungesättigten Fließ- und Transportmodellen in der ungesättigten Zone sind jedoch oft begrenzt aufgrund von ungenügender Kenntnis über die strukturelle und textuelle Heterogenität des Bodens. Um mehr Informationen über Bodenstruktur, -textur und -heterogenität, als auch hydraulische Parameter zu erzielen, können nicht-invasive geoelektrische Methoden in Labor- und Feldstudien angewendet werden. Eines der mehr versprechenden elektrischen Verfahren ist die Spektrale Induzierte Polarisation (SIP), die die komplexe elektrische Leitfähigkeit im Niederfrequenzbereich von 1 mHz bis 45 kHz misst. In der letzten Zeit wurde diese Methode verwendet um die gesättigte hydraulische Leitfähigkeit von verfestigten und unverfestigten porösen Medien vorherzusagen. Um die Polarisationsmechanismen besser zu verstehen und die Bandbreite der SIP-Anwendungen in der ungesättigten Zone zu erweitern, ist es wichtig die Beeinflussung der SIP Antwort vom Wassergehalt zu untersuchen. Des Weiteren ist es vielleicht möglich SIP Ergebnisse mit der ungesättigten hydraulischen Leitfähigkeit zu verknüpfen. Aus diesem Grund ist das Hauptziel dieser Doktorarbeit die Bestimmung von effektiven hydraulischen Eigenschaften von ungesättigten und unverfestigten porösen Medien mit Hilfe von SIP Messungen.

In einem ersten Schritt, wurde ein Labormessplatz entwickelt, der kombinierte elektrische und hydraulische Messungen an unverfestigten porösen Medien zulässt. Das experimentelle Design ermöglicht es Proben in mehreren aufeinander folgenden Druckstufen zu entwässern und den Wasserausfluss automatisch aufzuzeichnen um den Wassergehalt zu bestimmen. Messungen der komplexen elektrischen Leitfähigkeit werden mit Hilfe eines elektrischen Impedanzspektrometers mit hoher Messgenauigkeit durchgeführt. Experimente an einem unverfestigten Quarzsand und drei Sand-Ton-Gemischen mit 5, 10 und 20 Gewichtsprozent Ton wurden durchgeführt. Die gemessene komplexe elektrische Leitfähigkeit wurde mit Hilfe einer Debye-Zerlegung interpretiert, die DC Widerstand, Aufladbarkeit und Relaxationszeitverteilung zur Verfügung stellt.

Der Einfluss des Wassergehalts auf elektrische Parameter wie Real- und Imaginärteil der komplexen elektrischen Leitfähigkeit, Phasenverschiebung und Debye Parameter wurde für alle vier künstlich gemischten Sedimentproben untersucht. Die Amplitude des spezifischen elektrischen Widerstands, der Phasenspektren und deren Abhängigkeit vom Wassergehalt sind für jede Probe unterschiedlich. Im Falle des reinen Sandes nimmt die Phase mit abnehmendem Wassergehalt über den kompletten Frequenzbereich zu und ein Phasenmaximum ist bei mittleren bis niedrigen Wassergehalten vorhanden. Die Phasenspektren der Sand-Ton-Gemische zeigen das gleiche Verhalten wie der Sand; allerdings tritt zusätzliche eine Verschiebung des Phasenmaximums zu höheren Frequenzen auf. Diese Verschiebung lässt die Folgerung zu, dass Relaxationszeit und -länge kleiner werden, wenn der Wassergehalt abnimmt, was im Zusammenhang mit den kleineren Poren steht, die bei niedrigem Wassergehalt noch gesättigt sind.

Zusätzlich wurde der Einfluss der effektiven ungesättigten hydraulischen Eigenschaften auf die SIP Parameter untersucht. Die Ergebnisse zeigen eine klare Potenzgesetz-Korrelation zwischen dem Matrixpotenzial und der Relaxationszeit des Phasenmaximums der Sand-Ton-Gemische. Es wurden jedoch zwei unterschiedliche Steigungen für diese Beziehung beobachtet, eine für Matrixpotentiale größer als -120 cm und eine weitere für kleinere Matrixpotentiale. Die beobachtete Steigung war quadratisch für Matrixpotentiale  $>-120$  cm

und linear für Matrixpotentiale  $< -120$  cm. Die quadratische Korrelation wurde Diffusionsprozessen zugeordnet, während die lineare Korrelation einen bislang unbekanntem Relaxationsprozess andeutet. Die Beziehung zwischen der elektrischen Relaxationszeit und der ungesättigten hydraulischen Leitfähigkeit wurde mit Hilfe dieser Beziehung und einer vereinfachten Version des Mualem – van Genuchten Modells erzielt. Die Steigung dieser Potenzgesetz-Abhängigkeit zwischen ungesättigter hydraulischer Leitfähigkeit und Relaxationszeit hängt von der Breite der Porengrößenverteilung ab, die durch den semiempirischen  $n$ -Parameter des Mualem-van Genuchten Modells ausgedrückt wird. Es wurde die Schlussfolgerung gezogen, dass die ungesättigte hydraulische Leitfähigkeit mit Hilfe von SIP bestimmt werden kann, indem die Relaxationszeit und zusätzliche Informationen wie der  $n$ -Parameter des Mualem-van Genuchten Modells genutzt werden.

# Table of Contents

1	Introduction .....	1
1.1	Motivation .....	1
1.2	Modeling of flow in unsaturated zone.....	1
1.3	Laboratory and field methods to determine water retention and hydraulic conductivity function.....	2
1.4	Geophysical methods to determine hydraulic properties .....	3
1.4.1	Analogy electrical and hydraulic flow .....	3
1.4.2	DC electrical methods .....	4
1.4.3	Induced Polarization.....	4
1.4.4	Spectral Induced Polarization.....	5
1.4.4.1	Models of SIP for saturated soil.....	5
1.4.4.2	Spectral Induced Polarization measurements on saturated soil .....	7
1.4.4.3	Prior work on SIP for unsaturated soil .....	8
1.5	Aims and structure of thesis .....	9
2	Joint measurement setup for determining spectral induced polarization and soil hydraulic properties.....	11
2.1	Introduction .....	11
2.2	Fundamentals and interpretation of spectral induced polarization (SIP) measurements .....	13
2.3	Fundamentals and interpretation of multi-step outflow measurements .....	14
2.4	Description of the measurement setup .....	15
2.4.1	Electrical measurement equipment .....	15
2.4.2	Joint measurement cell for simultaneous SIP and MSO measurements .....	16
2.5	Test measurements on sand.....	20
2.5.1	Methods.....	20
2.5.2	Electrical results for the sand .....	21
2.5.3	Electrical results for shrinking material .....	25
2.6	Summary and conclusions.....	26
3	Spectral induced polarization measurements on variably saturated sand-clay mixtures .....	29
3.1	Introduction .....	29
3.2	Materials and Methods .....	30
3.2.1	Measurement setup.....	30
3.2.2	Sample preparation.....	31
3.2.3	Data interpretation.....	32
3.3	Results and Discussion.....	32
3.4	Conclusions .....	43
4	Electrical-hydraulic relationships of unsaturated sand-clay mixtures using spectral induced polarization .....	45
4.1	Introduction .....	45
4.2	Materials and Methods .....	47
4.2.1	Measurement setup.....	47
4.2.2	Sample characterization .....	48
4.2.3	Experimental approach.....	48
4.2.4	Data interpretation of electrical results .....	49
4.2.5	Data interpretation for hydraulic measurements .....	50
4.3	Results and Discussion.....	52
4.4	Conclusions .....	61

5	Conclusions and Outlook .....	63
5.1	Final Conclusions .....	63
5.2	Outlook.....	65
5.2.1	Further laboratory studies using SIP .....	65
5.2.2	Laboratory EIT experiments .....	65
5.2.3	Step to the field .....	65
5.2.4	Simulation .....	66

## List of Tables

Table 2.1: Dimensions of the measurement cells.....	17
Table 2.2: Physical properties of the ceramic plates from the manufacturer. $d$ – thickness, $\varnothing$ - diameter, $\alpha^{-1}$ - air entry value, $\Phi$ - approximate porosity, $r_p$ – maximum pore size, $K_s$ – saturated hydraulic conductivity. ....	19
Table 3.1. Petrophysical properties of the pure sand and the sand-clay mixtures. ....	31
Table 3.2: Fitted petrophysical model parameters (Eq. 4) for the pure sand and the sand-clay mixtures. ....	34
Table 4.1: Soil physical properties of the pure sand and the sand-clay mixtures. ....	48
Table 4.2: Pressure steps for all four samples. ....	49
Table 4.3: Initial parameter estimates of the sample material for the optimization during the modeling with HYDRUS-1D. $\theta_s$ is the saturated water content, $\theta_r$ is the residual water content, $\alpha$ is the inverse of the air-entry-pressure, $n$ is a shape parameter related to the pore size distribution, and $K_s$ is the saturated hydraulic conductivity. ....	51
Table 4.4: Mualem-van Genuchten parameter obtained by inverse modeling with HYDRUS 1D. $\theta_s$ – saturated water content, $\theta_r$ – residual water content, $\alpha$ - inverse of air entry value, $n$ – $n$ parameter, $K_s$ – saturated hydraulic conductivity, $R^2$ – coefficient of determination.....	53
Table 4.5: Petrophysical parameters fitted using the model of Jougnot et al. (2010). ....	55
Table 4.6: Coefficients $b_3$ for $h \leq 120$ cm ( $b_{3,a}$ ) and $h \geq 120$ cm ( $b_{3,b}$ ). ....	60



## List of Figures

Figure 1.1: Polarization mechanisms for a porous medium (after Ghorbani et al. (2008)). (a) Polarization of the electrical double layer (EDL) related to a single spherical silica grain caused by local diffusive flows of anions and cations and resulting in an excess and deficiency of ion concentration and thus to a polarized grain. (b) Membrane polarization caused by clay particles in the pore throats acting as ion-selective zones. (c) Polarization related to pore-throats acting as ion-selective zones. (d) No interfacial polarization: The layered medium is parallel to the electric field. (e) Maxwell (interfacial) polarization: The layered medium is perpendicular to the electric field. (f) Wagner (interfacial) polarization: Dielectric host with conductive inclusions. ....	6
Figure 2.1: a) Picture of measurement cell; drawing of measurement cell for b) non-shrinking soil and c) shrinking soil: 1 – Current porous bronze electrodes, 2 – Potential electrodes: non-polarizable, 3 – Potential electrodes: steel, 4 – Chamber filled with water, 5 – Chamber for the pressurized air supply (only for shrinking soil), 6 – Chamber filled with the sample, 7 – Ceramic plates, 8 – Small tube of PMMA, 9 – Connector to pressurized air, 10 – Connector to water burette; d) picture of measurement cell for shrinking cell; e) drawing of non-polarizable potential electrodes: 1 – Tube of PMMA, 2 – Ceramic cone point, 3 – Calcium chloride solution, 4 – Silver wire, 5 – Plug. ....	16
Figure 2.2: a) Test measurements for calibration of the non-polarizable ceramic and stainless steel potential electrodes. Phase spectra with (+cp) and without (-cp) ceramic plates in the measurement cell were measured using the ceramic electrodes. b) Test measurements for comparison of the phase spectra measured with both potential electrode types on relatively dry sand-clay mixture. ....	18
Figure 2.3: Hydraulic measurements with the MSO equipment. Applied pressure (red crosses – left Y axis) and outflow (blue circles – right Y axis) as a function of time in days. ....	20
Figure 2.4: Soil-water characteristic curve. Water content as a function of the capillary pressure achieved from the hydraulic measurements and from HYDRUS1D. ....	21
Figure 2.5: Amplitude of the complex electrical conductivity versus frequency for all equilibrium water saturations measured with ceramic electrodes. ....	22
Figure 2.6: Real part of the complex conductivity versus water saturation at a frequency of 1 Hz: a) model of Waxman & Smits (1968) and b) model of Revil et al. (2007). ....	22
Figure 2.7: a) Phase angle and b) imaginary part of the complex electrical conductivity versus frequency for all equilibrium water saturations measured with ceramic electrodes. ....	23
Figure 2.8: Cole-Cole chargeability associated with the phase peak in dependence on water saturation. ....	24
Figure 2.9: Cole-Cole relaxation time associated with the phase peak in dependence on a) water saturation and b) unsaturated hydraulic conductivity determined by Hydrus1D. ....	24
Figure 2.10: Phase angle of the complex electrical conductivity versus frequency for Selhausen soil conducted in the measurement cell for shrinking material. The arrows show how the phase spectra have changed when the upper part of the measurement cell was lowered to reestablish the electrical contact between the upper current electrode and the sample. ....	26
Figure 3.1: Sketch of experimental setup: A pump is used to desaturate the sample using several pressure steps. Electrical measurements are conducted using a high-accuracy impedance spectrometer. The high air-entry porous ceramic cones of the non-polarizing potential electrodes are located in the sample to keep a good electrical contact. ....	30
Figure 3.2: Measured and modeled real part of the complex electrical conductivity ( $\sigma'$ ) at 1 Hz as a function of water saturation: (a) pure sand, (b) 5% sand-clay mixture, (c) 10% sand-clay mixture, and (d) 20% sand-clay mixture. ....	33

Figure 3.3: Frequency-dependent imaginary part of the complex electrical conductivity ( $\sigma''$ ) of the investigated pure sand as a function of water saturation. ....	35
Figure 3.4: Frequency-dependent imaginary part of the complex electrical conductivity ( $\sigma''$ ) of the investigated sand-clay mixture with 5% clay content as a function of water saturation. ....	36
Figure 3.5: Frequency-dependent imaginary part of the complex electrical conductivity ( $\sigma''$ ) of the investigated sand-clay mixture with 10% clay content as a function of water saturation. ....	37
Figure 3.6: Frequency-dependent imaginary part of the complex electrical conductivity ( $\sigma''$ ) of the investigated sand-clay mixture with 20% clay content as a function of water saturation. ....	37
Figure 3.7: Imaginary part of the complex electrical conductivity ( $\sigma''$ ) at a frequency of (a) 0.01 Hz and (b) 1 kHz for all samples as a function of water saturation. ....	38
Figure 3.8: Normalized total chargeability ( $m_{n,tot}$ ) of all samples as a function of water saturation. ....	39
Figure 3.9: Conceptual model for electrical response associated with unsaturated sand-clay mixtures. a) Full saturation: Intergrain pore spaces act as large pores, while the grain contact regions act as narrow pores. The clay minerals are mainly loosely arranged within the entire saturated pore space. b) Medium saturation: The clay minerals are rearranged into a smaller available saturated pore volume. Some of the clay particles are associated with the sand grains. c) Low saturation: Grain contact regions become the large pores, while the water films around the sand grains act as narrow pores. d) Dry soil: The amount of water in the grain contact regions is reduced, resulting in a decreased difference between effective pore radii associated with grain contacts and water films. ....	40
Figure 3.10: Estimated peak relaxation time ( $\tau_{peak}$ ) from the $\tau$ distribution obtained with Debye decomposition for different water saturations of the 5% sand-clay mixture. ....	41
Figure 3.11: Peak relaxation time ( $\tau_{peak}$ ) of all samples as a function of water saturation. ....	42
Figure 4.1: Simplified sketch of the measurement column for joint hydraulic and electric measurements: Ce 1 and ce 2 are current electrodes being porous bronze plate electrodes. Cp1 and cp2 are ceramic plates with an air-entry pressure of 1 bar. Pe1 and pe2 are non-polarizable electrodes consisting of a Plexiglas tube filled with a calcium chloride solution and having a ceramic cone with an air-entry pressure of 1 bar. ....	47
Figure 4.2: Outflow experiments for a) pure sand b) 5% sand-clay mixture c) 10% sand-clay mixture, and d) 20% sand-clay mixture. ....	52
Figure 4.3: Retention curves for a) pure sand b) 5% sand-clay mixture c) 10% sand-clay mixture, and d) 20% sand-clay mixture. ....	53
Figure 4.4: Electrical phase spectra for a) pure sand b) 5% sand-clay mixture c) 10% sand-clay mixture, and d) 20% sand-clay mixture. ....	54
Figure 4.5: DC resistivity $\rho_0$ which was achieved by the Debye Decomposition versus the unsaturated hydraulic conductivity. ....	56
Figure 4.6: Normalized total chargeability achieved by the Debye Decomposition versus the unsaturated hydraulic conductivity. ....	57
Figure 4.7: (a) Matric potential versus peak relaxation time. (b) Relaxation time versus pore radius. ....	58
Figure 4.8: Peak relaxation time versus the unsaturated hydraulic conductivity. ....	60

# 1 Introduction

## 1.1 Motivation

Groundwater is one of the most important resources for humanity because it is used, for instance, as drinking water and for agriculture use and thus to feed humanity. However, groundwater is endangered through overuse and contamination. Soils fulfill important functions to protect the groundwater and to maintain a good water quality. They act as filter, buffer, and storage for water (Scheffer & Schachtschabel, 2010). For many applications, the understanding of flow and transport processes in soils is of importance. However, these processes are controlled by structural and textural heterogeneities that are difficult to determine in the field. Geophysical measurement methods like spectral induced polarization (SIP) can help to determine saturated (e.g., Pape et al., 1987; de Lima & Niwas, 2000; Binley et al., 2005; Hördt et al., 2007) and unsaturated (e.g., Titov et al., 2004; Binley et al., 2005; Jougnot et al., 2010) hydraulic properties to gain information on flow (Ghorbani et al., 2008; Jougnot et al., 2009) and transport processes (e.g., Börner et al., 1996; Revil & Linde, 2006; Revil, et al., 2007) in porous media. In addition, electrical impedance tomography (EIT), which is the 3D imaging version of SIP, is able to provide information about the structural and textural heterogeneity. Thus, in the future it may be possible to use EIT to determine unsaturated hydraulic conductivity distribution in the field.

## 1.2 Modeling of flow in unsaturated zone

Water flow and chemical transport are often numerically simulated with computer models to better understand contamination of the subsurface environment or for enhancing agricultural applications. A multitude of those models is based on the Richard's equation that describes the water flow in the vadose zone (Richards, 1931):

$$\frac{\partial \theta}{\partial t} = \frac{\partial}{\partial z} \left[ K(\theta) \frac{\partial H}{\partial z} \right] = \frac{\partial}{\partial z} \left[ K(\theta) \left( \frac{\partial h}{\partial z} - 1 \right) \right], \quad (1.1)$$

where  $K$  is the hydraulic conductivity,  $H$  is the hydraulic head,  $h$  is the matric potential,  $z$  is the elevation above a vertical datum,  $\theta$  is the water content, and  $t$  is the time. In order to use Richard's equation, closed-form expressions are used to relate  $K$ ,  $h$ , and  $\theta$ . In particular, the water retention function relates the water content with the matric potential and the hydraulic conductivity curve relates the hydraulic conductivity and the matric potential. A lot of research has been dedicated to the formulation and parameterization of these closed-form expressions. Leij et al., (1997) provided an overview of closed-form expressions that are used in computer modeling programs like for instance Hydrus-1D. These closed-form expressions can be differentiated into different types, such as single-porosity, dual-porosity, and dual-permeability expressions. The most commonly used type is the Mualem-van Genuchten model (Mualem, 1976; van Genuchten, 1980):

$$S_r = \frac{\theta(h) - \theta_r}{\theta_s - \theta_r} = \left( 1 + |\alpha h|^n \right)^{-m} \quad (1.2)$$

$$K(h) = K_s \left( \frac{\theta(h) - \theta_r}{\theta_s - \theta_r} \right)^{1/2} \left( 1 - \left( 1 - \left( \frac{\theta(h) - \theta_r}{\theta_s - \theta_r} \right)^{1/m} \right)^m \right)^2, \quad (1.3)$$

where  $S_r$  is the relative saturation,  $\theta_r$  is residual water content,  $\theta_s$  is the water content at full saturation,  $\alpha$  is the inverse of the air-entry value,  $n$  is a shape parameter related to the pore size distribution,  $m = 1 - 1/n$ , and  $K_s$  is the saturated hydraulic conductivity.

### **1.3 Laboratory and field methods to determine water retention and hydraulic conductivity function**

There are different methods to obtain estimates of effective hydraulic properties. These methods can be divided into empirical and experimental approaches. Empirical approaches are based on estimating the hydraulic properties from more easily available information. For example, the Kozeny-Carman equation (Carman, 1997) or the Hazen equation (Hazen, 1893) can be used to estimate the saturated hydraulic conductivity from the grain size distribution obtained by sieving and from pedotransfer functions (Vereecken et al., 2010).

The experimental approaches can be separated in laboratory and field methods (see for instance (Dane & Topp, 2002)). For laboratory methods, disturbed or undisturbed soil samples have to be taken in the field. Experimental approaches like permeameters are used to measure the hydraulic head and thus determine the unsaturated hydraulic conductivity. For such permeameter approaches water runs through a core sample under either constant (constant-head) or variable hydraulic gradient (falling-head). The first method is usually used for materials of moderate to high  $K$  while the second one is used for materials with low  $K$ . Multi step outflow experiments (e.g., van Dam et al., 1994) are commonly to determine effective unsaturated hydraulic properties by draining soil samples via several consecutive pressure steps. The hydraulic head and water outflow measured during drainage are used to inversely estimate the Mualem-van Genuchten parameters using hydrological modeling programs like HYDRUS-1D.

One class of field methods are the hydrogeological methods to determine the saturated hydraulic conductivity of aquifers. These are typically conducted in or in-between boreholes like for instance pump tests (Sanchez-Vila et al., 1999) and slug tests (Butler et al., 1996; Butler, 1998). Pump tests are conducted by stimulating an aquifer through constant pumping in observation wells. The observed drawdown is usually interpreted using an analytical model of aquifer flow, for example the Theis solution, under the assumption that the parameters from this idealized model apply to the real-world data. For more complex cases, numerical models may be used to analyze the observed data. Slug tests being a variation of typical pumping tests are also conducted in wells through an instantaneous change (increase or decrease) of the water table. This test is often conducted to get a quick estimate of the aquifer properties in a few minutes.

A second class of field methods are used to characterize hydraulic properties of the vadose zone, such as infiltrometry with single ring, double ring, and disc infiltrometers (resp. disc permeameters). With these methods, the rate of water infiltration into the soil is measured and analytical or numerical solutions of water flow are used to obtain estimates of the unsaturated hydraulic properties (Simunek et al., 1999). Inverse modeling of field data is also increasingly used to determine unsaturated hydraulic properties (e.g., Bauer et al., 2012; Mboh et al., 2011).

Information about the shallow subsurface is usually gained by collecting samples or conducting hydrological or geophysical borehole measurements. However, these approaches

are limited because they contain only information about the subsurface at that specific point, are time-consuming and also expensive. For some investigation objectives, such local measurements might be sufficient but when the study site is large compared to the scale of the heterogeneity or when the hydrology is complex, key-information about the hydrological situation may not be achieved (Binley et al., 2010).

## 1.4 Geophysical methods to determine hydraulic properties

Limitations of the hydrologic approaches have resulted in a multitude of studies that explored the possibility of combining hydrologic approaches with geophysical measurements to provide improved and minimally invasive characterization and monitoring information. Such joint approaches build the relatively new research area of “hydrogeophysics”. Rubin & Hubbard (2005) defined “hydrogeophysics” as “the use of geophysical measurements for mapping subsurface features, estimating properties, and monitoring processes that are important to hydrological studies, such as those associated with water resources, contaminant transport, and ecological and climate investigations”. The main applications of hydrogeophysical approaches are to provide information and input parameters for hydrological flow and transport models, hydrogeological mapping, and monitoring of hydrological processes. In the last decades, numerous geophysical studies were dedicated to hydrological investigations and almost all geophysical methods can be used for hydrogeophysical studies, such as seismic refraction and reflection, electrical resistivity, electromagnetic methods, and ground penetrating radar (GPR) (Slater, 2006; Vereecken et al., 2006; Revil et al., 2012). In this thesis, we focus on the use of electrical methods to estimate hydraulic properties.

### 1.4.1 Analogy electrical and hydraulic flow

The estimation of the hydraulic conductivity from electrical measurements is based on the fact that both water and the electrical current flow through the interconnected pore space of a porous medium. Electrical methods include: Electrical Resistivity (ER), Electrical Resistivity Tomography (ERT), Induced Polarization (IP), Spectral Induced Polarization (SIP), Electrical Impedance Tomography (EIT), and Self Potential (SP) measurements. These methods are used to measure potential differences in volts between two (or more) potential electrodes. This voltage can be transformed into electrical resistance,  $R$ , using Ohm’s law:

$$R = \frac{U}{I}, \quad (1.4)$$

where  $U$  is the potential difference, and  $I$  is the electric current. Using a geometric factor  $G$  for the applied electrode configuration, the resistance can be transformed into electrical resistivity,  $\rho$ , or electrical conductivity,  $\sigma$ :

$$\rho = \frac{1}{\sigma} = G \frac{U}{I}. \quad (1.5)$$

For complex electrical resistivity methods like IP, SIP, and EIT, the electrical resistivity is measured as a complex quantity  $\rho^*(\omega)$  consisting of real ( $\rho'$ ) and imaginary ( $\rho''$ ) part. The complex electrical resistivity can also be written as resistivity magnitude ( $|\rho|$ ) and phase angle ( $\varphi$ ) between the excited sinusoidal current and measured voltage signal:

$$\rho^*(\omega) = \frac{1}{\sigma^*(\omega)} = \rho'(\omega) + i\rho''(\omega) = |\rho(\omega)| \cdot e^{i\varphi(\omega)}, \quad (1.6)$$

where  $\omega = 2\pi f$ , and  $i = \sqrt{-1}$ . It is a matter of choice whether measurements are expressed in terms of complex electrical conductivity or complex electrical resistivity. The imaginary part of the electrical resistivity is related to the specific surface area of a porous medium and is caused by polarization processes coming from ion displacement currents in the pore space. Thus, measurements of the complex resistivity provide information on two important properties of the pore volume, i.e. the real part is related to the porosity and the imaginary part is related to the specific surface area.

### **1.4.2 DC electrical methods**

Many studies investigated the estimation of the hydraulic conductivity using petrophysical relations between electrical measurements and effective properties like the interconnected pore space and the interconnected pore surface area (Börner & Schön, 1991; Börner et al., 1996; Lesmes & Frye, 2001; Weller et al., 2010). The review paper of Slater (2006) provides a good overview of various approaches to estimate K from electrical measurements. Several electrical studies during the 1970's and 1980's revealed a log-log relationship between the electrical resistivity and the hydraulic conductivity for DC electrical measurements. However, both positive and negative correlations have been found depending on site mineralogy, grain size distribution, pore size distribution, and pore fluid chemistry (Huntley, 1986). Purvance & Andricevic (2000) reviewed these findings and showed that the log-log relationship between electrical resistivity and hydraulic conductivity is negative when interconnected pore volumes dominate the electrical current flow and positive when the electrical current flow is governed by interconnected pore surface areas. Thus, K estimation using DC electrical resistivity measurements is often limited because these measurements cannot separate whether the electrical resistivity is dominated by electrical conduction of the pore fluid or by interface conductivity of clay minerals.

In case of studies that attempt to relate electrical properties to the unsaturated hydraulic conductivity, the dependence of the electrical resistivity on the water saturation has to be taken into account. This was for example done by Doussan & Ruy (2009). They proposed three different approaches to estimate the unsaturated hydraulic conductivity using DC electrical measurements and parameters like the saturated hydraulic conductivity and the surface conductivity. They accounted for the water content by using the formation factor for different water contents, i.e. as a function of the matric potential, instead of the formation factor for saturated conditions. However, the approach of Doussan & Ruy (2009) is not able to estimate the unsaturated hydraulic conductivity from electrical measurements alone but needs additional information like saturated hydraulic conductivity, electrical resistivity of the pore fluid, and clay content that have to be determined in further experiments and are not always available.

### **1.4.3 Induced Polarization**

Although the electrical resistivity is both sensitive to the pore volume and the specific surface of a porous medium, those two properties cannot be clearly separated by DC electrical methods. In contrast to DC electrical methods, Induced Polarization (IP) measures not only the real part but also the imaginary part of the electrical conductivity or respectively the phase shift between the induced current and the measured voltage signal. During the last decades, a comprehensive volume of electrical studies has been published demonstrating a power-law dependence between the imaginary part of the electrical resistivity and the pore-related

specific surface area of a porous medium (Börner & Schön, 1991; Börner et al., 1996; Slater & Lesmes, 2002; Slater et al., 2006; Weller et al., 2010). Therefore, several studies have attempted to predict the saturated hydraulic conductivity from complex electrical properties. Several approaches are based on Kozeny-Carman type equations to predict the permeability  $k$  from electrical and petrophysical properties:

$$k = \frac{\Phi a_{eff}}{T 8\pi}, \quad (1.7)$$

with  $\Phi$  being the porosity,  $T$  is the tortuosity, and  $a_{eff}$  is the effective hydrodynamic cross section. The permeability  $k$  can be transformed into the hydraulic conductivity  $K$  using the following equation:

$$K = \frac{k \cdot d_w \cdot g}{\eta}, \quad (1.8)$$

where  $d_w$  is the density of water,  $g$  is the gravitational acceleration, and  $\eta$  is the dynamic viscosity. Thus,  $K$  is dependent on both the physical properties of the porous medium and the fluid. A modified version of the Kozeny-Carman equation is the PARIS equation (Pape et al., 1982; Pape et al., 1987), which is only valid for sandstones:

$$k = \frac{475}{F \cdot S_{por}^{3.1}}, \quad (1.9)$$

with  $F$  being the formation factor and  $S_{por}$  is the pore-volume related specific surface area. This semi-empirical equation is based on the approach to replace the two geometric parameters  $T$  and  $a_{eff}$  with parameters that can easily be determined. The tortuosity was replaced by the formation factor with the assumption that the geometrical and electrical tortuosity are the same. The second geometric parameter  $a_{eff}$  can be written as  $\pi r_{eff}^2$ , whereas  $r_{eff}$  can be expressed using the capillary surface area  $S_{por}^*$ :

$$S_{por}^* = \frac{2}{r_{eff}} \quad (1.10)$$

A similar approach using a power-law relationship between the hydraulic conductivity  $K$  and the imaginary component of the electrical conductivity was presented by Slater & Lesmes (2002):

$$K = a \cdot (\sigma'' )^{-j}, \quad (1.11)$$

where  $a$  and  $j$  are empirical constants. It was observed that the power law exponent is a function of soil type with ranges from 0.9-1.3 for unconsolidated soils (Slater & Lesmes, 2002) and 2.8-4.6 for sandstones (Börner et al., 1996). However, recent studies (Binley et al., 2005; Scott & Barker, 2005) showed that the relationship between the imaginary part of the electrical conductivity and  $S_{por}$  may not always be strong enough to allow  $K$  estimation using such Kozeny-Carman type approaches.

## 1.4.4 Spectral Induced Polarization

### 1.4.4.1 Models of SIP for saturated soil

An overview of the different polarization mechanisms in a porous medium without metallic components like ores (see Figure 1.1) was given by Ghorbani et al. (2008). They generalized that any restriction of relative displacement of charges results in an accumulation of negative charges on one side of the medium and positive charges on the opposite side and thus results in the polarization of this medium. The electrochemical origin of most of the polarization

mechanisms is related to the existence of an electrical double layer (EDL) forming at the grain-fluid interface. At this interface, an EDL consisting of the Stern layer and the diffuse layer is formed due to diffusive and electrostatic forces. In porous media like soils, the solid surface usually has a negative charge that is counterbalanced by the positive charge of the Stern and diffuse layer. The thickness of this electrical double layer usually remains thin with respect to the size of the pore throats and the grain size (Revil & Florsch, 2010). In more detail, the following polarization mechanisms have been proposed. Figure 1.1a shows the polarization of the EDL of a single spherical silica grain that was proposed for dilute suspensions (Lyklema, 1995). Membrane polarization (see Figure 1.1b) is caused by clay particles in pore-throats acting as barriers for anions due to their high negative surface charge. The third polarization mechanism (Figure 1.1c) is related to pore-throats acting as ion-selective zones. The remaining two polarization mechanisms are geometrical and interfacial polarization (Figure 1.1d-f). The origin of these mechanisms is a difference in conductivity or polarizability among components in a mixture that produces charge accumulations at the interface. Maxwell (1893) investigated layered materials and found that the medium only polarized when the layers were perpendicular to the electric field (Figure 1.1d and e). The last type of polarization mechanism (Figure 1.1f) was investigated by Wagner (1924) who solved the complex permittivity of a dilute suspension of conductive spheres. This interfacial polarization is therefore also known as Maxwell-Wagner polarization. This Maxwell-Wagner polarization only occurs at higher frequencies ( $> 100$  Hz) and, therefore, is of secondary importance for SIP measurements.

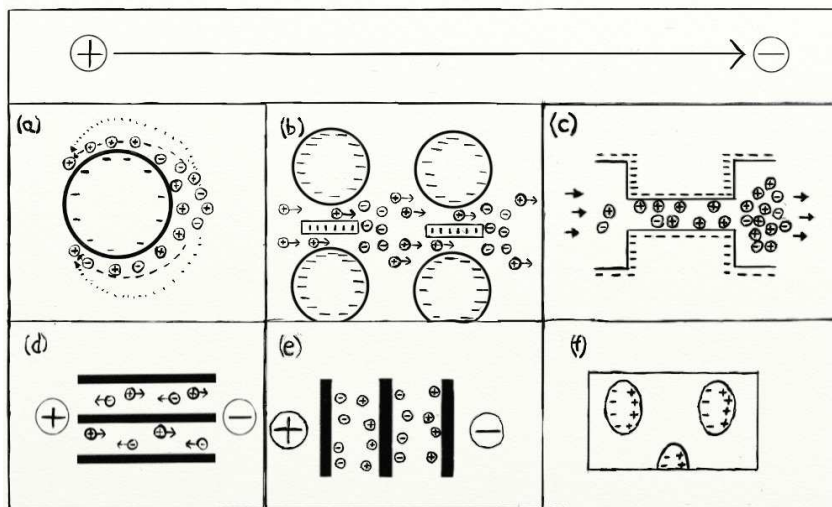


**Figure 1.1: Polarization mechanisms for a porous medium (after Ghorbani et al. (2008)). (a) Polarization of the electrical double layer (EDL) related to a single spherical silica grain caused by local diffusive flows of anions and cations and resulting in an excess and deficiency of ion concentration and thus to a polarized grain. (b) Membrane polarization caused by clay particles in the pore throats acting as ion-selective zones. (c) Polarization related to pore-throats acting as ion-selective zones. (d) No interfacial polarization: The layered medium is parallel to the electric field. (e) Maxwell (interfacial) polarization: The layered medium is perpendicular to the electric field. (f) Wagner (interfacial) polarization: Dielectric host with conductive inclusions.**

There are two classes of models that are typically invoked to explain SIP measurements on porous media. One type of model attempts to relate SIP to the polarization of grains (Figure 1.1a, hereafter referred to as the grain model). The first mechanistic model describing the polarization of a single grain was proposed by Schwarz (1962) by replacing the EDL with

a single layer of counterions that was able to move only tangentially to the grain surface (i.e. no exchange between bulk solution and EDL). In addition, Schwarz (1962) related the relaxation time to the square of the particle radius and the diffusion coefficient of the counterions. However, Dukhin & Shilov (1974) demonstrated that the treatment of Schwarz of the polarization of the EDL was not accurate for disperse solutions. They developed a linearized polarization model for a particle surrounded by a Gouy-Chapman diffuse layer and hypothesized that the Stern layer does not polarize and thus does not contribute to the surface conductivity. However, it was found that the model of Dukhin & Shilov (1974) could not explain the available experimental data. Thus, Lyklema (2002) proposed that the Stern layer could be the important part of the EDL for polarization of a single grain. More recently, Leroy et al. (2008) proposed a model combining polarization of the Stern layer and Maxwell-Wagner polarization. This model is connected to a triple-layer model and accounts for the partitioning of counterions between the Stern and diffuse layer. A key assumption in the model of Leroy et al. (2008) is that for saturated porous media with a small grain-to-grain contiguity the polarization of the diffuse layer is prevented by the overlapping of the EDLs at the grain contacts. Experimental studies such as those by Klein & Sill (1982), Chelidze & Gueguen (1999), Lesmes & Morgan (2001), and Revil & Florsch (2010) have also related the relaxation time to the grain size.

A second class of models attempts to relate SIP to the polarization of pore-throats acting as ion-selective zones (Figure 1.1c, hereafter referred to as the pore size model). This model is supported by Marshall and Madden (1953) and Titov et al. (2002, 2004), who proposed the consecutive short-narrow pore model. They showed a dependence of the relaxation time on the square of a pore surface length scale that can be determined by the distribution of wide or narrow pores. The experimental studies of Binley et al. (2005) and Scott & Barker (2003) support the pore size model. For example, Binley et al. (2005) found a power-law relationship between the relaxation time and the dominant pore throat size with an exponent of 1.04. Scott & Barker (2003) also observed a positive power-law relationship between these two parameters.

#### ***1.4.4.2 Spectral Induced Polarization measurements on saturated soil***

Spectral Induced Polarization measures the complex electrical resistivity in a frequency range between 1 mHz and several kHz. This multi-frequency analysis gives additional electrical parameters that can be obtained by using one of the many phenomenological relaxation models, like the Cole-Cole model (Cole & Cole, 1941; Pelton et al., 1987):

$$Z(\omega) = R_0 \left[ 1 - \sum_k m_k \left( 1 - \frac{1}{1 + (i\omega\tau_k)^{c_k}} \right) \right], \quad (1.12)$$

where  $Z$  is the impedance,  $R_0$  is the DC electrical resistivity at very small frequencies,  $m_k$  is the chargeability,  $i = \sqrt{-1}$  being the imaginary unit,  $\tau_k$  is the relaxation time,  $\omega = 2\pi f$ , and  $c_k$  is the Cole-Cole exponent. More recently, Debye decomposition (Nordsiek & Weller, 2008; Zisser et al., 2010) is often used. The chargeability is a measure of the polarization that is related to the interfacial charge storage of ion displacements in the pore space but is also influenced by the electrical resistivity. Thus, the normalized total chargeability is often used which is a measure of the polarization of the whole sample. The relaxation time is related to the length-scale over which ions in the electrical double layer move during electric current application. The Cole-Cole exponent determines the width of the phase maximum and usually ranges between 0.1 and 0.6 for consolidated and unconsolidated sedimentary rocks.

Many studies investigated the potential of SIP for K estimation in saturated conditions. Based on the theoretical proportionality of both relaxation time and hydraulic conductivity on the square of an effective length scale, Kemna (2000) proposed a linear relationship between the relaxation time  $\tau$  and the permeability  $k$ . Pape & Vogelsang (1996) also proposed that the time constant of their pigeon-hole model was a measure of the permeability. Strong power law relationships between the relaxation time and the hydraulic conductivity were found for sandstones ( $\tau \sim K^{0.26}$ , Binley et al., 2005) and unconsolidated sands ( $\tau \sim K^{1.78}$ , Kemna et al., 2005). The different exponents for unconsolidated and consolidated sediments are related to the cementation factor  $m$  of Archie's law that is dependent on the cementation and the rock, respectively soil type. All these empirical studies indicate that the relaxation time is a measure of the effective hydraulic radius used in the original Kozeny-Carman equation.

#### ***1.4.4.3 Prior work on SIP for unsaturated soil***

Most SIP studies were conducted on fully saturated samples so that only relationships between the relaxation time and the saturated hydraulic conductivity have been investigated. Binley et al. (2005) also conducted SIP measurements on unsaturated sandstones and showed that the water saturation has to be taken into account for SIP studies. They observed a decrease of the relaxation time with decreasing water saturation. In addition, they suggested a parallelism between SIP behavior and unsaturated hydraulic conductivity.

Titov et al. (2004) investigated sieved quartz samples in dependence on the water content. For some cases the unsaturated pores contained air in other cases it was filled with kerosene. They found two different power-law relationships between resistivity and water content and also between chargeability and water content. They proposed the short-narrow-pore model as a conceptual model to explain the observed results. In the saturated case, the water filled pore space was considered to be the largest current pathways and the areas of grain contact were assumed to act as narrow ion-selective pores. In the unsaturated case, most of the water is bound at the areas of grain contacts and thus form the largest current pathways, whereas the water films coating the particles are the ion-selective zones.

Jougnot et al. (2010) presented a mechanistic model for partially saturated clay-rocks. This model is based on the model proposed by Leroy et al. (2008) and combines polarization of grains in the Stern layer of the EDL and additional Maxwell-Wagner polarization at high frequencies. The model predicts that the relaxation time is independent of the water content and is only dependent on the dominant grain size. However, measurements of Jougnot et al. (2010) showed a increasing relaxation time with decreasing water content which was attributed to an increase of 'dominant length scale' with desaturation due to clay mineral deformation that increased the relaxation path length of the ions causing polarization. Finally, Cassiani et al. (2009) investigated the SIP behavior in dependence of saturation with both air and a non-aqueous phase liquid (octanol and benzene). They found that the resistivity increase with decreasing water saturation is less for non-aqueous phase liquids than with the same amount of air. In addition, they found that the relaxation time increases with decreasing saturation, albeit differently for air and non-aqueous phase liquids.

## **1.5 Aims and structure of thesis**

SIP has proven to be a valuable measurement method for hydrologic applications due to the links between properties of the complex electrical resistivity and hydraulic conductivity. However, much work remains to be done. In particular, the relationship between SIP and unsaturated hydraulic conductivity and the origin of the observed relaxation in porous media is still debated. Therefore, the general aim of this thesis is to determine effective hydraulic properties of unsaturated porous media using electrical spectral induced polarization measurements. This thesis has three specific objectives. The first objective is to build a joint measurement setup for simultaneous hydraulic and electrical measurements on unsaturated and unconsolidated porous media. The second objective is to study the dependence of the spectral induced polarization response on water saturation. Finally, the third objective was to investigate relationships between SIP parameters and unsaturated effective hydraulic properties.

Chapter two deals with the first objective. The developed joint measurement setup consists of a multi step outflow equipment to desaturate unconsolidated porous media using several pressure steps. For the electrical measurements a high-accuracy electrical impedance spectrometer was applied. A special measurement cell was constructed to allow spectral induced polarization measurements while the sample is drained without losing electrical contact between the electrodes and the sample. A test measurement with pure quartz sand is shown.

Chapter three is concerned with investigations of the influence of water saturation on spectral induced polarization properties. Long-term desaturation experiments on four different unconsolidated porous media - one sand and three artificially mixed sand-clay mixtures - were conducted using the joint measurement setup described in the second chapter. The behavior of spectral induced polarization is investigated in dependence on the water saturation, and a conceptual model is presented that explains our measurements.

Chapter four presents and discusses relationships between SIP parameters and unsaturated hydraulic properties. The results from the same four experiments on sand and sand-clay mixtures described in the third chapter are used. Unsaturated hydraulic properties for each sample are determined using the Mualem - van Genuchten parameters determined with inverse modeling of water outflow using HYDRUS-1D. Debye parameters like DC electrical resistivity, chargeability, and peak relaxation time of each pressure step are determined for all samples. Relationships between unsaturated hydraulic conductivity and the Debye parameters are investigated.

Finally, chapter five summarizes the main outcomes of this research project. In addition, possible future applications of spectral induced polarization to characterize soil hydraulic properties are discussed.



## **2 Joint measurement setup for determining spectral induced polarization and soil hydraulic properties<sup>\*</sup>**

### **2.1 Introduction**

Soil is an important resource that is useful in many ways for mankind. For example, it supports food and other biomass production and it stores many essential substances, such as water, carbon, and nitrogen. In addition, soil is an important protective buffer for vulnerable groundwater resources against contaminants. To manage and protect vital soil and groundwater resources, understanding of flow and transport processes in soils is essential. To describe water flow in the unsaturated zone, both hydraulic conductivity and water retention functions need to be provided. A range of methods is available to determine these soil hydraulic properties. The two most commonly used groups of methods are based on monitoring infiltration in the field (e.g., double-ring infiltrometer, tension-disk infiltrometer) or monitoring drainage or evaporation in the laboratory (e.g., multi-step outflow experiment). A detailed overview of methods to determine soil hydraulic properties is provided by Dane & Topp (2002).

The prediction capabilities of unsaturated flow and transport models are limited by insufficient knowledge of the structural and textural heterogeneity of the soil. Both infiltration measurements in the field and drainage and evaporation experiments in the laboratory are time-consuming and impractical to estimate the spatial variability of hydraulic properties. To obtain more information, geophysical methods may be employed in field-scale studies. Slater & Lesmes (2002) summarized the advantages of geophysical approaches to estimate hydraulic properties. First, geophysical measurements are non-invasive when applied from the earth surface and minimally invasive when conducted from a small number of boreholes. Second, measurements can be quickly performed and are less time-consuming than classical methods to determine hydraulic properties. Third, a relatively high temporal and spatial sampling density can be achieved. Nowadays, geophysical equipment and inversion algorithms can even provide 3D images of the subsurface.

The analogy between electric current flow and groundwater flow has led to various attempts to predict hydraulic properties from geoelectrical measurements (e.g., Vereecken et al., 2005; Slater, 2007). Since water in interconnected pores is the main path for water flow and electrolytic conduction, it is clear that both electrical and hydraulic properties are governed by pore space properties. Therefore, several studies have attempted to estimate hydraulic conductivity from DC electrical conductivity (e.g., Kosinski & Kelly, 1981). However, as discussed in detail by Purvance & Andricevic (2000), both positive and negative correlations between electrical and hydraulic conductivity can exist. A positive correlation is found when porosity controls electrical conductivity (e.g., clay-free sediments), while a negative correlation results from an electrical conductivity being controlled by specific surface area and cation exchange phenomena. Thus, it is not possible to uniquely predict the hydraulic conductivity from DC electrical measurements without additional knowledge of the specific surface area or cation exchange capacity.

Significant improvements in the estimation of hydraulic properties have been made using induced polarization (IP) measurements (e.g., Börner et al., 1996; Slater & Lesmes, 2002);

---

<sup>\*</sup> Adapted from K. Breede, A. Kemna, O. Esser, E. Zimmermann, H. Vereecken, and J.A. Huisman. Joint measurement setup for determining Spectral Induced Polarization and soil hydraulic properties. *Vadose Zone J.* 10: 716-726, doi: 10.2136/vzj2010.0110

Hördt et al., 2007; Revil & Florsch, 2010). With IP, the complex electrical conductivity of a sample is determined for a single frequency (or a small subset of frequencies). The complex electrical conductivity is a measure of both the electrolytic conductivity and the ohmic interface conductivity (real part) and the polarization effects (imaginary part). Polarization is caused by charged interfaces and constrictions in the pore space, which lead to zones of unequal ionic transport properties in the pore space (e.g., Börner et al., 1996; Titov et al., 2002). Polarization at interfaces is associated with metals and clays (e.g., Madden & Cantwell, 1967; Olhoeft, 1985) and with the electrical double layer that exists for all minerals Leroy et al. (2007). In clay-free and metal-free sediments, polarization effects are mainly associated with tangential ion displacement in the electrical double layer forming at the grain-fluid interface (e.g., Schwarz, 1962; Börner et al., 1996; Chelidze & Gueguen, 1999). There have been several studies that established empirical correlations between the imaginary part of the electrical conductivity at a particular frequency and hydraulic conductivity (e.g., Börner et al., 1996; Slater & Lesmes, 2002). However, it is difficult to generalize these empirical relationships because of the inherently frequency-dependent nature of the complex electrical conductivity, which is not considered in IP.

Spectral induced polarization (SIP) is used to characterize the complex electrical conductivity for a broad frequency bandwidth (i.e., mHz to kHz range). The frequency dependence of the complex electrical conductivity is of great interest because it provides information on characteristic relaxation times which are indicative of characteristic length scales of the sample (e.g., Scott & Barker, 2003; Binley et al., 2005). Recently, Jougnot et al. (2010) proposed a mechanistic model for interpreting SIP measurements of partially saturated clay-rocks. Their model combines the polarization of the inner part of the electrical double layer (Stern layer) and Maxwell-Wagner polarization and predicts that the characteristic relaxation time is independent of water saturation, but instead only depends on the given grain size (i.e., grain diameter). Furthermore, they showed an adequate fit between measured and modeled complex electrical conductivity above 1 Hz, although the measured characteristic relaxation time increased with decreasing saturation due to deformation within the clay rock. Binley et al. (2005) reported correlations between the characteristic relaxation time and both the hydraulic conductivity and the air entry pressure (i.e., the  $\alpha$  parameter in the Mualem-van Genuchten model) of sandstone samples. In addition, for their samples the characteristic relaxation time decreased with decreasing saturation, as would be expected for a characteristic length scale because the water is held in smaller pores for lower saturation. Although not further explored by Binley et al. (2005), this implies a link between unsaturated hydraulic conductivity and relaxation time.

There have been only a few studies that focus on the relationship between spectral induced polarization and unsaturated hydraulic properties for unconsolidated samples (e.g., Münch et al., 2005; Ghorbani et al., 2008). Because of the low polarizability of most unconsolidated samples, such investigations require highly accurate measurements of the complex electrical conductivity. Therefore, the aim of this paper is to present an experimental setup that allows simultaneous hydraulic and SIP measurements with the high accuracy required for characterization of soils and sediments with low polarizability. As a proof of concept, we analyze the complex electrical conductivity as a function of saturation for an unconsolidated sandy soil sample. The paper is organized as follows. First, the fundamentals of SIP measurements are shortly outlined in section 2. The multi-step outflow approach used to determine the soil hydraulic properties is shortly presented in section 3. In section 4, the joint setup for simultaneous electrical and hydraulic measurements is presented. Section 5 presents results of complex electrical conductivity measurements on unconsolidated sand as a function

of saturation using the newly developed experimental setup. Furthermore, results of the hydraulic measurements are shown in this section.

## 2.2 Fundamentals and interpretation of spectral induced polarization (SIP) measurements

To measure the effective complex electrical conductivity of a soil sample, an electrical excitation voltage with known amplitude and frequency is applied at two current electrodes positioned at both ends of the sample. This results in an alternating electric current in the sample, and the associated voltage is measured at two potential electrodes, which are located between the current electrodes. The recorded voltage and current are converted to the frequency dependent complex electrical conductivity ( $\sigma^*(\omega)$ ) using the geometric factor for the electrode arrangement.  $\sigma^*(\omega)$  can also be expressed as conductivity magnitude ( $|\sigma|$ ) and phase angle ( $\varphi$ ) between the excited sinusoidal current and measured voltage signal or as a sum of the real ( $\sigma'$ ) and imaginary part ( $\sigma''$ ) of the electrical conductivity:

$$\sigma^*(\omega) = |\sigma| \cdot e^{i\varphi} = \sigma'(\omega) + i\sigma''(\omega), \quad (2.1)$$

with  $i = \sqrt{-1}$  and  $\omega = 2\pi f$ .

It is a matter of choice whether measurements are expressed in terms of  $\sigma^*$ , complex electrical resistivity,  $\rho^*$ , or complex dielectric permittivity,  $\varepsilon^*$ :

$$\sigma^*(\omega) = \frac{1}{\rho^*(\omega)} = i\omega\varepsilon^*. \quad (2.2)$$

These electrical parameters can all be calculated from the measured impedance and the sample geometry. We choose to present the spectral electrical response in terms of amplitude and phase angle,  $\varphi$ , of  $\sigma^*$ . These can be calculated from the real and imaginary components of  $\sigma^*$  as follows:

$$|\sigma(\omega)| = \sqrt{(\sigma'(\omega))^2 + \sigma''(\omega)^2}, \quad (2.3)$$

$$\varphi(\omega) = \arctan\left[\frac{\sigma''(\omega)}{\sigma'(\omega)}\right] \approx \frac{\sigma''(\omega)}{\sigma'(\omega)}. \quad (2.4)$$

The approximation in Eq. (2.4) is valid for phase angles below  $\sim 100$  mrad (Ulrich & Slater, 2004).

Ohmic conduction in unconsolidated sediments is ionic, occurring through the pore-filling electrolyte and by ion migration in the electrical double layer forming at the grain-fluid interface (surface conductivity). The surface conductivity ( $\sigma_s^*$ ) depends on matrix mineralogy, grain size, and electrical conductivity of the pore fluid. A classic model to describe the bulk conductivity of a porous medium ( $\sigma^*$ ) in the presence of surface conductivity was presented by Waxman & Smits (1968):

$$\sigma^* = \frac{S_w^n}{F} \left( \sigma_w + \frac{\sigma_s^*}{S_w} \right), \quad (2.5)$$

where  $F$  is the formation factor,  $S_w$  is the water saturation,  $n$  is the saturation exponent, and  $\sigma_w$  is the pore water conductivity. In this equation, the ‘surface conductivity’ should be interpreted as a contribution of the ions in the diffuse double layer. In addition, the division of the surface conductivity by the saturation implies that the diffuse double layer extends over the entire pore space. Recently, Revil et al. (2007) derived the following model using a volume averaging approach:

$$\sigma^* = \frac{1}{F} (\sigma_w S_w^n + (F-1)\sigma_s^*). \quad (2.6)$$

In this model, the surface conductivity is related to the Stern layer and, thus, to the tortuosity of the solid phase instead of the water phase. For this reason, the formation factor appears as a multiplier before the surface conductivity. It should be noted that in Revil et al. (2007) and Jougnot et al. (2010) the contribution of the diffuse double layer was considered in  $\sigma_w$  through the Donnan equilibrium approach. Here, we assume that  $\sigma_w$  equals the conductivity of the bulk solution used to saturate the sample, which implies that we neglect the contribution of the diffuse double layer to the bulk electrical conductivity in Eq. (2.6). Therefore, these two models can be considered as limiting cases where the surface conductivity is either attributed to the diffuse double layer or to the Stern layer.

To characterize the measured electrical spectra, we used the program SPECFIT described in Kemna (2000) and Chen et al. (2008). In this program, the magnitude and phase spectra of complex resistivity ( $\rho^*(\omega) = 1/\sigma^*(\omega)$ ) are regarded as a superposition of three Cole-Cole spectra:

$$\rho^*(\omega) = \rho_0 \left( 1 - \sum_{k=1}^3 m_k \left( 1 - \frac{1}{1 + (i\omega\tau_k)^{c_k}} \right) \right), \quad (2.7)$$

where each Cole-Cole dispersion term is characterized by a chargeability  $m_k$ , a relaxation time  $\tau_k$ , the Cole-Cole exponent  $c_k$ , and  $\rho_0$  is the DC resistivity. The relaxation time is related to a relaxation frequency by  $\tau = (2\pi f)^{-1}$ . The Cole-Cole term with the smallest relaxation time accounts for the effect of capacitive coupling at high frequencies. This approach is similar to that of Pelton et al. (1978) to describe inductive coupling in complex resistivity spectra. The other two Cole-Cole terms summarize the electrical response of the soil. The parameters of the three Cole-Cole terms are determined by minimizing the difference between measured and modeled log magnitude and phase data using a conventional real-valued least-squares approach with Marquardt regularization Press et al. (1992).

### 2.3 Fundamentals and interpretation of multi-step outflow measurements

For hydraulic measurements, the multi-step outflow (MSO) method was selected. This method is widely considered to be one of the standard laboratory methods for the determination of hydraulic conductivity and water retention functions (e.g., Dane & Topp, 2002). The idea behind the MSO method is to drain a soil sample by applying a set of predefined pneumatic pressures. The hydraulic parameters can be determined by inverse modeling of the recorded outflow as a function of the applied pressure (van Dam et al., 1994). The program HYDRUS-1D of Simunek et al. (2005) was used for modeling the multi-step outflow experiment. The applied pressure at the top of the soil column was transformed into suction at the bottom of the soil column and the measured outflow was normalized to the area of the soil column. The water content and the hydraulic conductivity as a function of the pressure head,  $h$ , were described by the Mualem–van Genuchten model (Mualem, 1976; van Genuchten, 1980):

$$\frac{\theta(h) - \theta_r}{\theta_s - \theta_r} = (1 + |\alpha h|^n)^{-m}, \quad (2.8)$$

where  $\theta_r$  is the residual and  $\theta_s$  is the saturated soil water content,  $\alpha$  is the inverse of the air-entry value,  $n$  is a shape parameters related to the pore size distribution and  $m = 1 - 1/n$ . The hydraulic conductivity is given by

$$K(h) = K_s \left( \frac{\theta(h) - \theta_r}{\theta_s - \theta_r} \right)^{1/2} \left( 1 - \left( 1 - \left( \frac{\theta(h) - \theta_r}{\theta_s - \theta_r} \right)^{1/m} \right)^m \right)^2, \quad (2.9)$$

where  $K_s$  is the saturated hydraulic conductivity.

## 2.4 Description of the measurement setup

The novel measurement setup consists of a combined SIP measurement system and a multi-step outflow cell to drain the sample. Most SIP studies on variably saturated porous media were conducted with evaporative drying so far. The advantage of pressure drainage over evaporative drying is that the electrical conductivity of the pore fluid remains stable and must, therefore, not be considered for data interpretation or modeling. In the following, we first present the electrical measurement equipment and then the combined measurement cell.

### 2.4.1 Electrical measurement equipment

The SIP measurements are made with a high-accuracy electrical impedance spectrometer described by Zimmermann et al. (2008). It is based on a 4-point electrode array: two electrodes for current injection and two electrodes for voltage measurement. A sinusoidal excitation voltage with a predefined frequency in the range from 1 mHz to 45 kHz is generated by a function generator (Agilent 33120A). The amplitude and frequency of the signal are remotely controlled. The measurement system is typically operated using an excitation voltage of  $\pm 5$  V, which was shown to provide a good signal-to-noise ratio (Zimmermann et al., 2008). An amplifier unit measures the voltages at the potential electrodes with minimum load and crosstalk. The voltages are then transmitted via short triaxial cables of 0.5 m to the DC-coupled amplifiers (JFET OP AD825) with high impedance and low capacity. To reduce parasitic leakage currents and capacitive loads, the cables are used with a driven shield (Morrison, 1998). The input capacity between the triaxial cables and ground is less than 5 pF, while the input resistance is higher than 1 G $\Omega$ . Due to the high input resistance, it is not required to use non-polarizable electrodes for the voltage measurements. To minimize crosstalk, the outer shields of the triaxial cables are connected to ground potential and the coupling capacities of the amplifiers are minimized so that they are smaller than 0.1 pF. Three different shunt resistors  $R_s$  (10  $\Omega$ , 100  $\Omega$  or 1 k $\Omega$ ) can be used for current measurement. All channels are constructed in an identical manner to minimize phase and gain differences between the channels.

The measured voltages are simultaneously digitized with 24-bit Sigma-Delta data acquisition cards (NI4472) providing a high phase accuracy and digital anti-aliasing filters. The maximum measurement frequency is about 45 kHz. The 24-bit (1.2  $\mu$ V) resolution enables the measurement of the AC voltages with a high signal-to-noise ratio. A LabVIEW program controls the function generator and the data acquisition cards. For each measurement frequency, the time series of the voltages are stored. A MATLAB program removes the drifts in the time series (as proposed by Dahlin et al., 2002) and computes the complex voltages from the measured time series at the known excitation frequencies.

## 2.4.2 Joint measurement cell for simultaneous SIP and MSO measurements

To simultaneously determine SIP and unsaturated hydraulic properties, design considerations for accurate SIP measurements have to be integrated into the MSO measurement cell. An important design consideration is the separation between current and potential electrodes because of the polarization of the current electrodes. Zimmermann et al. (2008) showed that the distance between the current and the potential electrodes should be at least twice the sample diameter to avoid errors associated with the polarization of the current electrodes. Therefore, our first measurement cell for non-shrinking materials, such as sand, consists of three units: a middle unit which is filled with the soil sample and an upper and a lower unit which are filled with tap water (see Figure 2.1a and b). The two water-filled units are used to increase the separation between current and potential electrodes, thus increasing the measurement accuracy. The dimensions of the measurement cell are provided in Table 2.1. To allow electrical measurements, the measurement cell is made of PMMA. The soil sample is fixed between two ceramic plates in the middle unit.

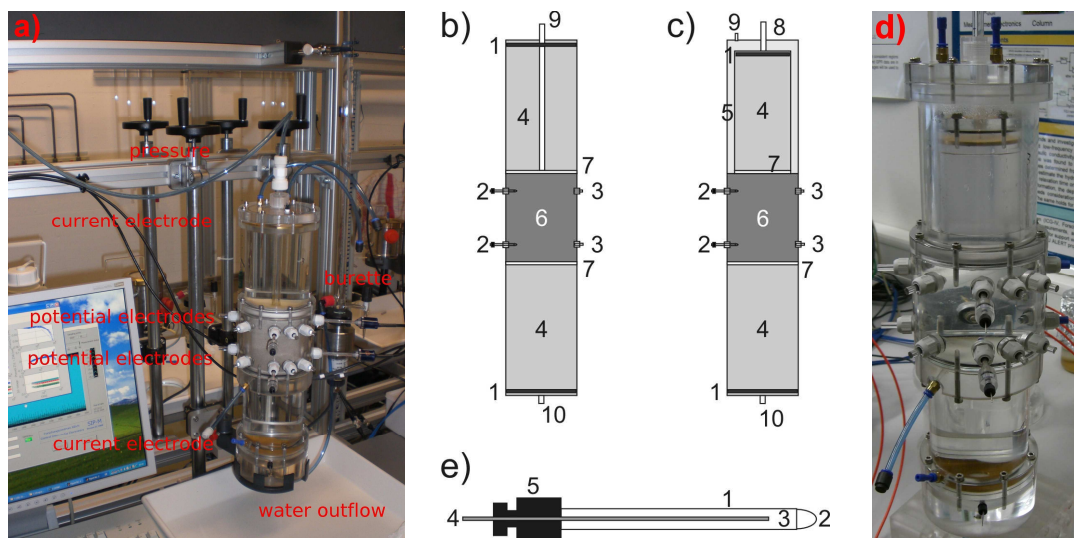


**Figure 2.1:** a) Picture of measurement cell; drawing of measurement cell for b) non-shrinking soil and c) shrinking soil: 1 – Current porous bronze electrodes, 2 – Potential electrodes: non-polarizable, 3 – Potential electrodes: steel, 4 – Chamber filled with water, 5 – Chamber for the pressurized air supply (only for shrinking soil), 6 – Chamber filled with the sample, 7 – Ceramic plates, 8 – Small tube of PMMA, 9 – Connector to pressurized air, 10 – Connector to water burette; d) picture of measurement cell for shrinking cell; e) drawing of non-polarizable potential electrodes: 1 – Tube of PMMA, 2 – Ceramic cone point, 3 – Calcium chloride solution, 4 – Silver wire, 5 – Plug.

Another important consideration for accurate SIP measurements is the selection of current and potential electrodes. Zimmermann et al. (2008) tested different current electrode materials like copper, stainless steel, and porous bronze. The results showed that at frequencies higher than 10 Hz, the impedance is almost independent of the electrode material and the current density. It depends only on the sample material and on the shape of the sample holder. For low frequencies, the porous bronze electrodes performed best. These porous bronze electrodes are made of Cu89Sn11 filter elements with an average pore diameter of 15  $\mu\text{m}$  and a porosity of 32% and they are located at the top as well as at the bottom of the measurement cell (Figure 2.1b). The current electrodes have a diameter of 89 mm and a thickness of about 4 mm. In

addition, they have a centered hole with a diameter of about 17 mm and four indentations at the edge. These indentations allow an easier removal of air bubbles from the underside of the current electrode. The hole is for a tube of PMMA (see Figure 2.1b, number 7) which is used to apply pressure to the soil sample.

**Table 2.1: Dimensions of the measurement cells.**

Dimensions	mm
Total length	400
Inner diameter	94.5
Outer diameter	105
Length of upper unit	150
Length of middle unit	100
Length of lower unit	150
Distance ceramic plate – potential electrode	20
Distance potential electrode – potential electrode	60

Typically, metallic materials are also used for potential electrodes (e.g. Zimmermann et al. (2008)). However, the presence of metallic potential electrodes in between the current electrode plates can distort the electric field in the sample due to electrode polarization, which affects the potential measurements. Electrode polarization depends on the electrode type, material, and the location in the sample holder. Electrode effects are typically observed at frequencies from 1 Hz up to 10 kHz. The minimization of this electrode polarization is commonly achieved by placing the metallic potential electrodes outside the sample and using an electrolyte for the electrical connection between the sample and the metal electrode (e.g., Zimmermann et al., 2008).

We used two types of potential electrodes in this study: one pair is made of stainless steel; the other pair consists of custom-made non-polarizable electrodes. These electrodes are inserted in the sample with a separation of 20 mm from each of the ceramic plates. The distance between both electrodes is 60 mm. The stainless steel electrodes are located outside of the sample for reasons discussed above. The non-polarizable electrodes are similar to the potential electrodes used by Ulrich & Slater (2004). They consist of a small tube of PMMA with a diameter of 5 mm and a length of 210 mm (see Figure 2.1e), and they are closed by a cone-shaped porous ceramic at one end and a plug at the other end. The ceramic cone has a diameter of 5 mm, a homogeneous porosity with an average pore size of 0.3  $\mu\text{m}$ , and an active surface of about 0.5  $\text{cm}^2$ . The ceramic is made out of aluminum oxide and its bubbling point is about 2000 hPa. Since the maximum applied pressure during an MSO experiment is 1000 hPa, the ceramic cups remain saturated throughout the experiment. The PMMA tube is filled with a 0.02 M  $\text{CaCl}_2$  solution. A silver wire with a diameter of 1 mm is located in the tube and is fixed by the plug at the end of the electrode. The construction of our electrodes allows positioning of the ceramic cone inside the measurement cell without greatly disturbing the electric field, because the metal inside the electrode is outside of the electric field in the measurement cell. Thus, a good contact to the sample is provided without introducing electrode polarization.

Test measurements in water were conducted for both electrode types (Figure 2.2a). The increase of the phase at higher frequencies is due to the capacitive load of the amplifiers and the contact impedance of the electrodes. Figure 2a shows that the measured phase is close to zero as expected for the stainless steel electrodes. Only for frequencies higher than 100 Hz, a slight increase is observed. The ceramic electrodes start to deviate from zero above 10 Hz due

to the higher contact impedance as compared to the stainless steel electrodes in water. However, it should be noted that the observed difference is still below 1 mrad.

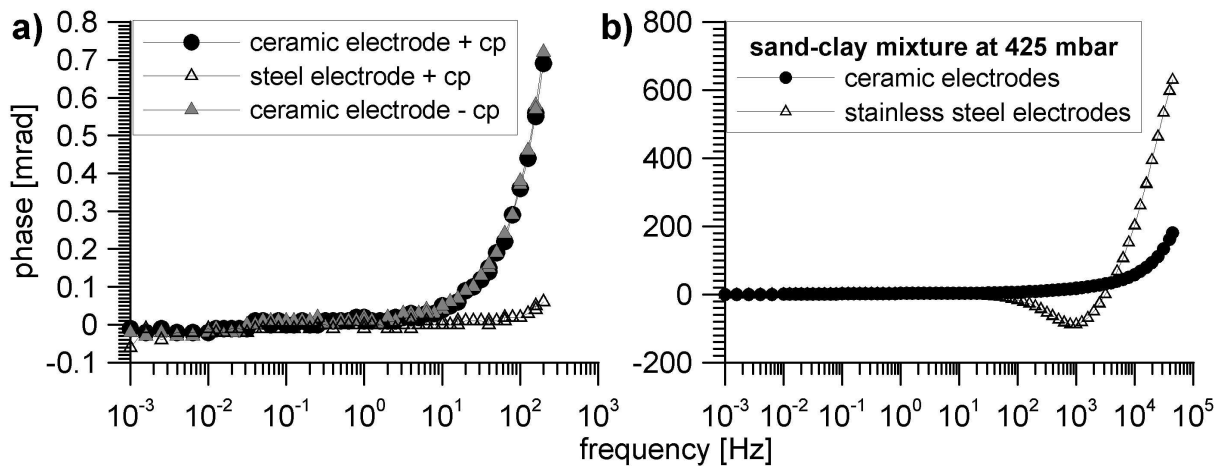


**Figure 2.2:** a) Test measurements for calibration of the non-polarizable ceramic and stainless steel potential electrodes. Phase spectra with (+cp) and without (–cp) ceramic plates in the measurement cell were measured using the ceramic electrodes. b) Test measurements for comparison of the phase spectra measured with both potential electrode types on relatively dry sand-clay mixture.

The contact impedance of the electrodes generally increases with decreasing water content. Figure 2.2b shows the phase angle for a measurement on a dry sand-clay mixture with a clay content of 5% for both the ceramic and the stainless steel electrodes. For frequencies lower than 10 Hz, the measured phase angle is similar for the two electrode types. At frequencies higher than 10 Hz, the phase error of the stainless steel electrodes increases dramatically due to the higher contact impedances of the electrodes. The measurements with the ceramic electrodes are clearly more appropriate, although the contact impedance of the electrodes also affects the measurements at higher frequencies. The reason for the strong increase in the measured phase angle with the stainless steel electrodes is the reduced electrical contact between the sample and the electrode when the water content decreases (i.e., no water film is present anymore between soil and electrode as in the case of a saturated sample).

The specifications of the ceramic plates that hold the sample in place are provided in Table 2.2. The ceramic plate at the top of the soil sample has a centered hole with a diameter of 10 mm. A tube of PMMA with a length of about 210 mm and a diameter of 10 mm was glued into the hole. The tube of this ceramic plate is fixed by a compression fitting to the lid of the measurement cell. The influence of the ceramic plates on the electrical measurements was evaluated. For this purpose, two measurements were conducted on water: one with and one without ceramic plates in place (Figure 2.2a). The results show that the ceramic plates have a negligible impact on the electrical measurements. The saturated hydraulic conductivity of the ceramic plates is relatively low (Table 2.2), which means that the ceramic plate at the bottom of the sample needs to be considered in the hydrologic model to obtain meaningful estimates of the hydraulic parameters from inverse modeling of the outflow data.

**Table 2.2: Physical properties of the ceramic plates from the manufacturer.  $d$  – thickness,  $\varnothing$  - diameter,  $\alpha^{-1}$  - air entry value,  $\Phi$  - approximate porosity,  $r_p$  – maximum pore size,  $K_s$  – saturated hydraulic conductivity.**

$d$ [mm]	$\varnothing$ [mm]	$\alpha^{-1}$ [hPa]	$\Phi$ [vol.-%]	$r_p$ [ $\mu\text{m}$ ]	$K_s$ [cm/sec]	Flow through ¼-inch plate [ml/hr/cm <sup>2</sup> /14.7 psi]
7	90	1000	45	2.5	8.6E-6	50

Figure 2.1c and d show the second measurement cell designed for measurements on shrinking soil. The upper unit of the cell was modified for this purpose. It now consists of the same outer cylinder and a new inner cylinder with a diameter of 70 mm and a length of 130 mm. The inner cylinder is filled with water and the space between the inner and the outer cylinder is filled with air. The current electrode is located at the top of the inner cylinder (see Figure 2.1c). The bottom of the inner cylinder is closed with a ceramic plate. This unit of the cell can be moved up and down by a small tube of PMMA, which has a length of 210 mm and a diameter of 10 mm. The connection for the current electrode, a silver wire with a diameter of 1 mm, is fed through this PMMA tube. The pressure is applied to the sample via the air-filled space between inner and outer cylinder. If the soil material shrinks during desaturation, an air gap typically occurs between the ceramic plate and the soil sample, which prohibits electrical measurement because of the lack of electrical contact. In this adapted design, the inner cylinder can be adjusted without removing the pressure from the soil. The disadvantage of the adapted design is that the distribution of the electric field is not as homogeneous as it is for the measurement cell shown in Figure 2.1b, because of the smaller diameter of the upper current electrode.

For both measurement cells, air pressure is applied to the measurement cell (see Figure 2.1b, c) As the air pressure is directly applied at the interface between the saturated upper ceramic plate and the top of the soil sample, part of the soil water is removed for each pressure step. This soil water flows through the lower ceramic plate and because of the incompressibility of water, this water will displace a comparable amount of water in the bottom water reservoir that will flow into the burette through the flexible tube. The water height in the burette is measured by a pressure sensor and converted into milliliter using a calibration factor. With increasing pressure steps, smaller and smaller pores of the sample are desaturated. As long as the lower ceramic plate is saturated, only water can flow or diffuse through it. Saturation of the ceramic plates is ensured by the high air entry pressure. The applied air pressure at the interface between the upper ceramic plate and the sample acts as a counter pressure such that water flow from the upper water reservoir through the ceramic plate and into the sample is prevented.

The rather complicated design of our joint measurement cell for combined measurements of SIP and hydraulic properties has some advantages over a simple design, where a column is packed with sediment with imbedded current and potential electrodes. First, it needs to be emphasized that a large separation between current and potential electrodes is required to determine SIP properties of sediments with sufficient accuracy. If a simple design of a one-piece column with a diameter of 8 cm is desired, then the entire length has to be about 40 cm to achieve high-accuracy SIP data. However, such a long sample holder completely filled with soil material has some disadvantages. First, the hydraulic measurements would take much more time. Second, a homogeneously packed sample is more difficult to achieve. Finally, the soil sample holder with a height of 10 cm and a diameter of 8 cm used in this study can be used to take in-situ soil samples representative of a soil horizon, which is not possible for a longer column design completely filled with soil material.

## 2.5 Test measurements on sand

A laboratory experiment was conducted to test the new measurement setup for joint hydraulic and electrical measurements. We used conditioned quartz sand with a medium grain size of 0.20 mm, a specific surface of 0.104 cm<sup>2</sup>/g, a bulk density of 1.62 g/cm<sup>3</sup>, and a porosity of 37.8%. The laboratory was air-conditioned and had a temperature of 20 ± 1°C.

### 2.5.1 Methods

Before the experiment was started, the measurement cell was filled with water and the electrical impedance was measured. This measurement was conducted to ensure that the measurement cell showed no unexpected polarization effects. In a next step, a small amount of water was removed from the middle unit of the cell and a pressure test up to 1000 hPa was performed to check whether the cell was airtight. In addition, the saturated hydraulic conductivity of the lower ceramic plate was determined. For this purpose, the measurement cell was connected to a burette filled with water via a flexible tube. The decrease of the water volume in the burette was recorded as a function of time and converted to saturated hydraulic conductivity of the ceramic plate. Next, the lower unit of the measurement cell was filled with water and covered with a ceramic plate that was saturated in a water bath for at least 24 hours. We used degassed tap water with a temperature of about 20°C throughout the experiment. The middle unit of the measurement cell was screwed onto the lower unit and some water was filled into the cell to cover the ceramic plate. A small amount of unconsolidated wet sand was mixed with water and added to the measurement cell. This process was repeated until the measurement cell was filled. The second ceramic plate with its tube was fixed by the compression fitting at the lid of the measurement cell before the entire upper unit was screwed onto the middle unit. Next, water was pumped into the upper unit of the measurement cell and it was put on a holder, horizontally leveled, and connected to the burette with a flexible tube. The sample was left to equilibrate with the water in the burette. After some days, when equilibrium and full saturation were reached, the measurement cell was connected to the pressure supply. We used the following pressure steps to desaturate the soil sample: 10, 40, 50, 52, 55, 60, 65, and 70 hPa. The applied pressure and the water outflow were automatically recorded as a function of time using dedicated Labview software (Figure 2.3). When the outflow of the sample was negligible and the electrical measurements were identical for two consecutive days, the next pressure step was applied.

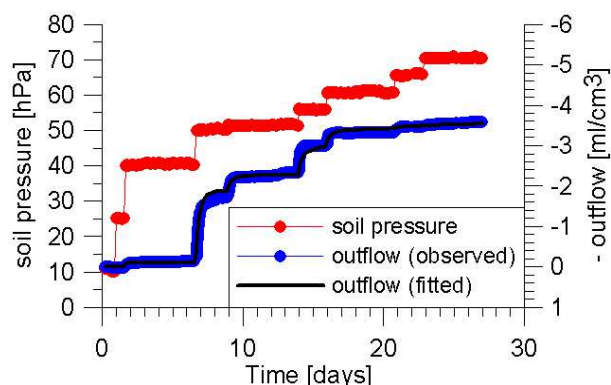


**Figure 2.3: Hydraulic measurements with the MSO equipment. Applied pressure (red crosses – left Y axis) and outflow (blue circles – right Y axis) as a function of time in days.**

The modeled outflow data obtained after minimizing the difference between measured and modeled outflow data using the Levenberg-Marquardt local optimization strategy

implemented in HYDRUS1D are also presented in Figure 2.3. During optimization of the Mualem–van Genuchten model parameters, the saturated water content,  $\theta_s$ , was fixed to the measured value of the porosity ( $0.379 \text{ m}^3 \text{ m}^{-3}$ ). The values of the remaining optimized parameters were:  $\theta_r = 0.024 \text{ m}^3 \text{ m}^{-3}$ ,  $\alpha = 0.0222 \text{ cm}^{-1}$ ,  $n = 19$ , and  $K_s = 402 \text{ cm d}^{-1}$ . The coefficient of determination,  $R^2$ , was 0.99 and the mass balance error was 0.32%. The quality of the fit is comparable to results obtained with dedicated MSO equipment.

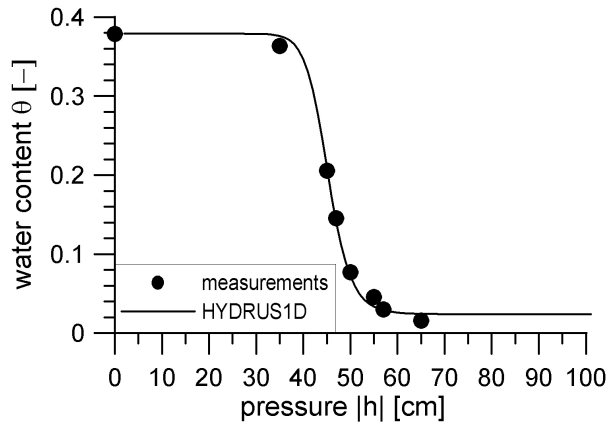
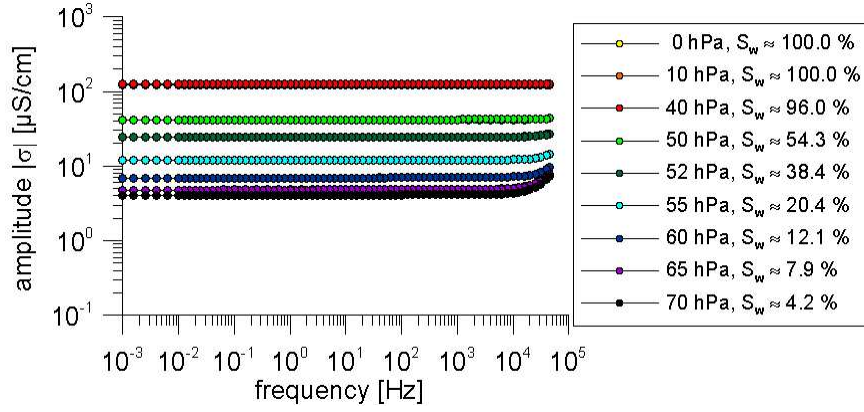


**Figure 2.4: Soil-water characteristic curve. Water content as a function of the capillary pressure achieved from the hydraulic measurements and from HYDRUS1D.**

Figure 2.4 shows the water retention function obtained from steady-state in the MSO measurement cell, and the water retention function obtained using the inversion is also provided. Both retention curves show a good agreement, emphasizing the quality of the fit. The high value of  $n$  is related to the steep decrease in the hydraulic conductivity when the unconsolidated sand starts to drain. High values of  $n$  were also reported by other researchers for unconsolidated sand samples (e.g., Lambot et al., 2009).

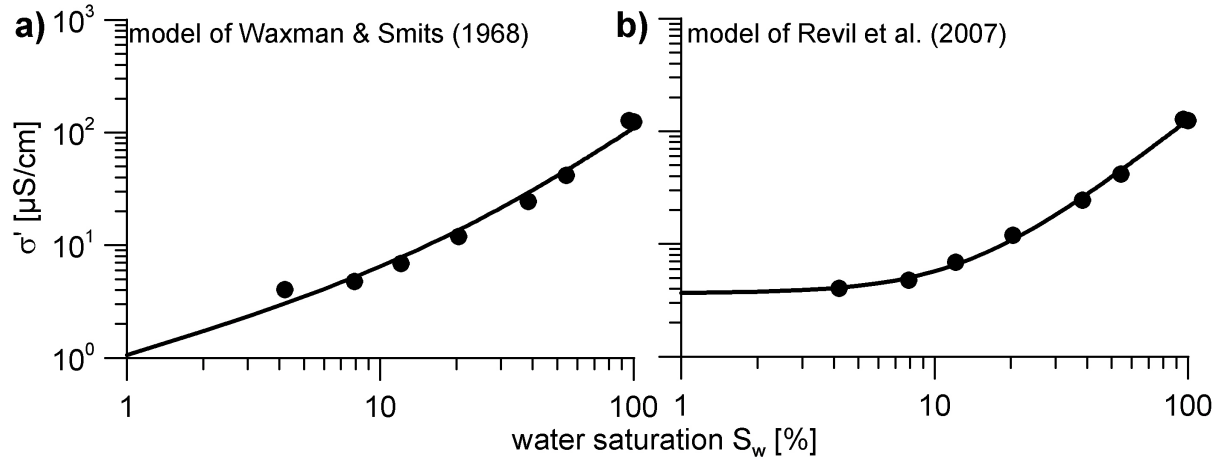
### 2.5.2 Electrical results for the sand

Figure 2.5 presents the measured amplitudes of the complex conductivity for the equilibrium water content associated with each pressure step. The amplitudes are nearly constant over the whole frequency range. For low water contents, the amplitude increases at high frequencies due to increased contact impedance of the electrodes as discussed in the context of Figure 2.2b. For the first three pressure steps (0, 10, and 40 hPa), the amplitudes are the same because the water outflow is small for these small applied pressures (water content remains close to saturation). With decreasing water content, the amplitude decreases.



**Figure 2.5: Amplitude of the complex electrical conductivity versus frequency for all equilibrium water saturations measured with ceramic electrodes.**

The petrophysical models presented in Eq. (2.5) and Eq. (2.6) were fitted to the real part of the bulk electrical conductivity at a frequency of 1 Hz. Our data are not well described by the model of Waxman & Smits (1968), as shown in Figure 2.6a.

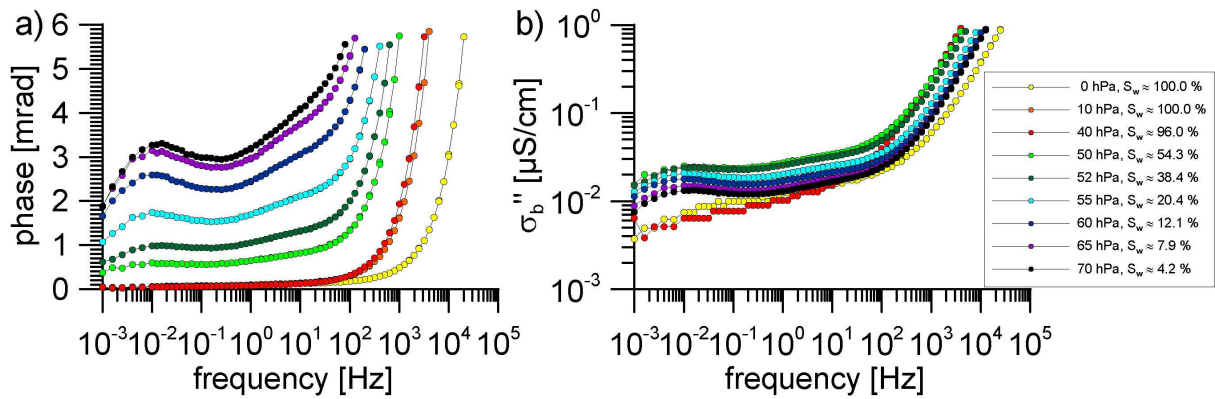


**Figure 2.6: Real part of the complex conductivity versus water saturation at a frequency of 1 Hz: a) model of Waxman & Smits (1968) and b) model of Revil et al. (2007).**

The fitted model parameters for the Waxman & Smits (1968) model are  $F = 4.97$ ,  $n = 1.64$ , and the  $\sigma_s'$  associated with the diffuse double layer is  $0.01 \text{ S m}^{-1}$ . Especially the latter value is too high for the relatively clean sand used in this study. We partly attribute the poor fit to the implicit assumption that the diffuse double layer extends over the entire pore space. This is perhaps a reasonable assumption for the shaly sands considered in Waxman & Smits (1968), but it is less realistic for the sand considered here. The data are much better described by the petrophysical model derived by Revil et al. (2007), as shown in Figure 2.6b. The fitted model parameters for the Revil et al. (2007) model are  $F = 3.69$ ,  $n = 1.77$ , and  $\sigma_s' = 5.0 \text{ } \mu\text{S cm}^{-1}$ . This is an indication that the surface conductivity in our quartz sand is dominated by the conductivity of the Stern layer, which seems reasonable when considering the modeling results of Leroy et al. (2008) for the pH and salinity of the pore water used in this study. The surface conductivity can also be calculated from the mean grain size and the surface conductance of the Stern layer (e.g., Leroy et al., 2008). Under the assumption that the sand consists of silica grains and that pore water consists of NaCl, the model of Leroy et al. (2008) predicts a frequency-dependent surface conductivity varying between  $0.87$  and  $0.61 \text{ } \mu\text{S cm}^{-1}$ .

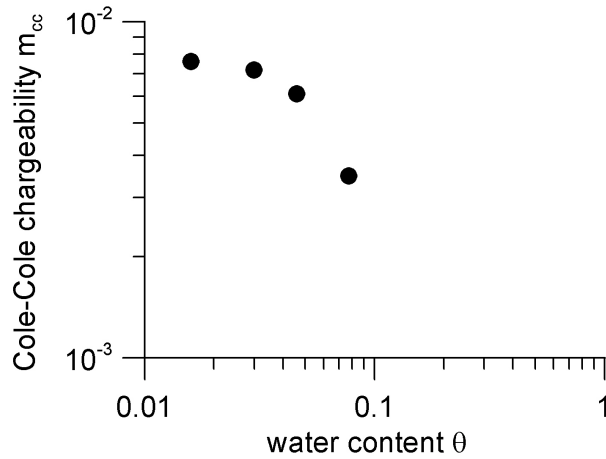
This is in reasonable agreement with our results given that the tap water used in this experiment is dominated by bivalent cations (mainly  $\text{Ca}^{2+}$ ).

Figure 2.7a presents the measured phase angles. As discussed above, the phase angle increases significantly due to the capacitive load of the amplifiers and the contact impedance of the electrodes at high frequencies Zimmermann et al. (2008). It is also evident that the phase angle is very small and shows a nearly constant phase behavior for the saturated sand. SPECFIT was used to determine Cole-Cole parameters for the measured complex resistivity. The two Cole-Cole spectra associated with the soil showed relaxation times near 25 s and 2.5 ms. These times are associated with the sand fraction and the minor silt fraction. In the following, we interpret only the lower relaxation times because these are associated with the phase maximum observed for low saturation (Figure 2.7). Measurements with small phase angles that approach a constant-phase behavior could not be reliably fitted with SPECFIT and are therefore not presented.



**Figure 2.7: a) Phase angle and b) imaginary part of the complex electrical conductivity versus frequency for all equilibrium water saturations measured with ceramic electrodes.**

With increasing pressure and decreasing water content both the phase angle (Figure 2.7a) and the chargeability increase (Figure 2.8). The same behavior was observed by Cosenza et al. (2007) and Jougnot et al. (2010) for partially saturated clay-rocks and by Cassiani et al. (2009) for sediments with low clay content. In contrast, Kruschwitz (2008) and Ghorbani et al. (2008) measured decreasing phase angles with decreasing saturation, although the modeling of Kruschwitz (2008) predicted increasing phase angles. Finally, Binley et al. (2005) reported phase angles that first increased and then decreased with decreasing saturation. Clearly, the database needs to be extended to understand and clarify these discrepancies. This will be an important objective of our future research.



**Figure 2.8: Cole-Cole chargeability associated with the phase peak in dependence on water saturation.**

With decreasing saturation, a peak in the phase angle appeared. The Cole-Cole relaxation time associated with this phase maximum varied only slightly with saturation (Figure 2.9a). Leroy, et al. (2008) related the relaxation time to the radius ( $a$ ) and the diffusion coefficient of the counter-ions ( $D_s$ ) in the Stern layer of the electrical triple-layer associated with the mineral surface:

$$\tau = \frac{a^2}{2D_s}. \quad (2.10)$$

Leroy et al. (2008) further argued that  $D_s$  does not deviate strongly from the diffusion coefficient in the water phase for hydrated ions and used  $D_s = 2.45 \times 10^{-9} \text{ m}^2 \text{ s}^{-1}$ . Using this value, the Cole-Cole relaxation times found in this study are associated with a radius of 0.31 to 0.35 mm, which is in the same order as the mean grain radius of 0.1 mm.

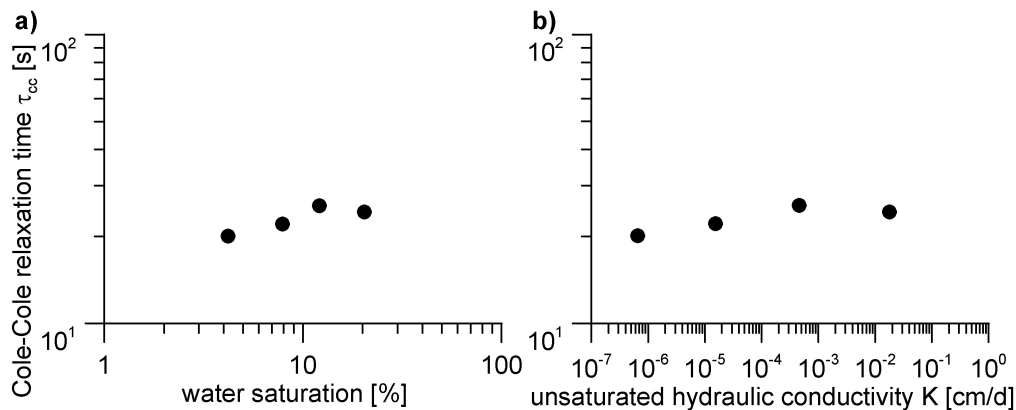


**Figure 2.9: Cole-Cole relaxation time associated with the phase peak in dependence on a) water saturation and b) unsaturated hydraulic conductivity determined by Hydrus1D.**

The results for the relaxation time presented in Figure 2.9a are consistent with the mechanistic models for partially saturated rocks developed by Jougnot et al. (2010) and Schmutz et al. (2010). Their models assume that the relaxation time is mainly related to the polarization of the Stern layer. Since the Stern layer is relatively unaffected by desaturation, these models

predict that relaxation time does not change with saturation and is mainly an expression of the dominant grain size. However, there are also discrepancies between our data and the models of Jougnot et al. (2010) and Schmutz et al. (2010). For example, the model of Schmutz et al. (2010) predicts an increasing  $\sigma''$  with decreasing water saturation. This is not the case for our measurements where  $\sigma''$  first increases and then decreases again with decreasing water saturation (Figure 2.7b). As already suggested by Jougnot et al. (2010), the correspondence between modeling results and data can perhaps be further improved by including a membrane polarization term in these models.

Since the Cole-Cole relaxation time is nearly constant as a function of saturation, this implies that the Cole-Cole relaxation time also shows little variation as a function of unsaturated hydraulic conductivity (Figure 2.9b). A practical implication of this is that relaxation times determined for well-sorted unconsolidated sands can be related to the saturated hydraulic conductivity, but do not provide information on unsaturated hydraulic conductivity. Again, the database of complex conductivity measurements on variably saturated soils needs to be extended to assess the validity of this finding for a wider range of soil materials.

### **2.5.3 Electrical results for shrinking material**

We have also conducted an experiment in the measurement cell for shrinking material. For this experiment, a sieved soil sample from an agricultural soil with 13% sand, 70% silt, and 17% clay was used. The sample was packed as described above for the sand. During the experiment it was necessary to adjust the upper part of the measurement cell to reestablish the electrical contact between the ceramic plate and the sample (Figure 2.1c and d). Loss of electrical contact was determined from the impedance between the upper current electrode and the upper potential electrode and the lower current electrode and the lower potential electrode, which is provided by the electrical impedance spectrometer system of Zimmermann et al. (2008). If the real part of the impedance between the upper electrodes increased much more than the impedance between the lower electrodes, this was a good indicator for the loss of electrical contact.

The phase spectra for this shrinking soil are shown in Figure 2.10. Again, the phase values are relatively low, even for unsaturated soil. No clear peak can be recognized, which is most likely related to the wide grain and pore size distribution. It is interesting to note that the phase initially decreased with decreasing saturation at higher frequencies and then it slightly increased again. Already at low pressure, the electrical contact was lost twice because the soil sample shrunk and cracks between the upper ceramic plate and the sample occurred. These cracks resulted in deviating phase angles at low frequencies (Figure 2.10). After adjusting the upper part of the measurement cell, the phase values were more plausible as indicated by the arrows in Figure 2.10. The difference between the phase spectra before and after adjusting the upper part of the measurement cell was as large as 2 mrad, which is high considering the small phase angles that were observed for this soil. At a pressure of 200 hPa, horizontal cracks at the height of the upper and lower potential electrodes appeared. Both the hydraulic and the electrical measurements could not be interpreted anymore from this point onwards.

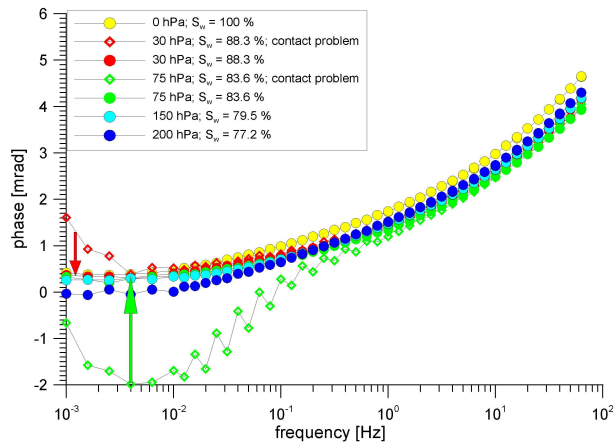


**Figure 2.10: Phase angle of the complex electrical conductivity versus frequency for Selhausen soil conducted in the measurement cell for shrinking material. The arrows show how the phase spectra have changed when the upper part of the measurement cell was lowered to reestablish the electrical contact between the upper current electrode and the sample.**

## 2.6 Summary and conclusions

A new experimental setup for combined electrical and hydraulic measurements on sediments and soils was developed. The electrical measurements are based on a high-accuracy spectrometer, and the hydraulic equipment consists of a multi-step-outflow apparatus which allows for individual pressure regulation. For the combination of these two measurement methods, two different measurement cells were constructed. The first measurement cell can be used for non-shrinking soil while the second one also allows measurements on shrinking soil. The first measurement cell allows more accurate electrical measurements due to a homogeneous distribution of the induced electric field in the sample. The disadvantage is that the electrical contact between the upper current electrode and the sample breaks when the soil shrinks. The second measurement cell also allows measurements on mildly shrinking materials. If the sample shrinks, the inner cylinder in the upper unit of the measurement cell can be moved down so that the electrical contact is reestablished. However, the accuracy of the electrical measurements made in this measurement cell is not as good as it is for the first one. This is due to the inhomogeneous distribution of the electric field in the sample. Test measurements have shown that the ceramic plates in the measurement cells have no influence on the electrical measurements. Two different electrode types were used as potential electrodes: stainless steel pins and ceramic electrodes. The stainless steel electrodes provided more accurate measurements in pure water and fully saturated sand, whereas the ceramic electrodes were much more accurate for unsaturated sand.

A first set of electrical and hydraulic measurements on an unconsolidated sand sample. The real part of the bulk electrical conductivity for this sand was best described by a petrophysical model that attributes the surface conductivity to the Stern layer. The measured phase values were generally low. Both the phase and the chargeability of the fitted Cole-Cole model increased with decreasing saturation. The Cole-Cole relaxation time associated with the observed maximum in the phase response at low saturation did not change with saturation, and was reasonably explained by the dominant grain size of the sand sample. This implies that relaxation times determined for well-sorted unconsolidated sands can be related to the saturated hydraulic conductivity, but do not provide information on unsaturated hydraulic conductivity. Finally, measurements on shrinking soil showed that the pressure range for

which electrical measurements could be made was extended by using an adjustable upper part of the measurement cell.



## 3 Spectral induced polarization measurements on variably saturated sand-clay mixtures<sup>†</sup>

### 3.1 Introduction

In recent years, there has been a growing interest in using the spectral induced polarization (SIP) method in environmental studies (see for example Vanhala, 1997; Kemna et al., 2000; Kemna et al., 2004; Slater & Binley, 2006; Hördt et al., 2007; Williams et al., 2009). The relationships between characteristics in the SIP response and lithological and pedological parameters, such as grain size distribution (Lesmes & Morgan, 2001), pore size distribution (Scott & Barker, 2003), specific surface area (Börner et al., 1996; Slater & Lesmes, 2002), presence of clay minerals (Klein & Sill, 1982; Slater & Lesmes, 2002), and permeability (Börner et al., 1996; Binley et al., 2005; Revil & Florsch, 2010) were investigated in several studies. However, most of these studies were conducted on fully saturated samples.

To better understand the mechanisms causing polarization and to extend the range of SIP applications to the vadose zone, it is important to investigate how the SIP response is affected by water saturation. Several studies have investigated the SIP response of unsaturated consolidated (e.g. Vinegar & Waxman, 1984; Worthington & Collar, 1984; Binley et al., 2005; Jougnot et al., 2010) and unconsolidated samples (e.g. Titov et al., 2004; Ulrich & Slater, 2004). Titov et al. (2004) conducted time-domain induced polarization (IP) measurements on sands with varying saturation. Their results showed a maximum in the chargeability at a water saturation of 18%. Interestingly, the relationship between log DC resistivity and log saturation also showed a change in slope at this water saturation. Ulrich & Slater (2004) also presented IP data of unsaturated unconsolidated porous media. In this study, saturation was varied by evaporative drying and pressure drainage and imbibition. They found a power-law dependence of the polarization magnitude on the saturation and observed that the behavior of the imaginary conductivity varied strongly as a function of the desaturation method (e.g. drainage or evaporation) and the sample lithology. Some samples showed an initial increase and a subsequent decrease of the imaginary conductivity with saturation, whereas other samples only showed an increase or decrease of the imaginary conductivity. Although these studies provided important insights into the IP response of unsaturated porous media, they did not analyze the frequency-dependent complex conductivity as a function of saturation for a wide range of frequencies.

Binley et al. (2005) analyzed broadband measurements of complex electrical conductivity (10 mHz to 1 kHz) as a function of saturation for sandstones. They were the first to report that the relaxation time associated with a maximum in the phase of the complex conductivity decreased with decreasing saturation. More recently, Jougnot et al. (2010) developed a mechanistic model for partially saturated clay-rocks that considers the polarization of the Stern layer of the electrical double layer and Maxwell-Wagner polarization. This model predicts that the relaxation time is independent of saturation and is only affected by the dominant diameter of the grains. The measurements on clay-rocks presented in Jougnot et al. (2010) showed an increase of relaxation time with decreasing saturation, which was attributed to an increase of ‘dominant length scale’ with desaturation due to clay mineral deformation that increased the relaxation path length of the ions causing polarization.

---

<sup>†</sup> Adapted from K. Breede, A. Kemna, O. Esser, E. Zimmermann, H. Vereecken, and J.A. Huisman. Spectral Induced Polarization measurements on variably saturated sand-clay mixtures. Revised to Near Surface Geophysics (22.12.2011)

This overview clearly indicates that there is a need to extend the database of SIP measurements on unsaturated samples. Therefore, the aim of this study is to investigate the complex electrical conductivity for pure sand and three sand-clay mixtures in the mHz to kHz frequency range as a function of frequency, saturation and clay content. In the remainder of this paper, we first present the experimental set-up used to drain the four samples and to make accurate measurements of the complex electrical conductivity. Next, sample preparation and data interpretation using a Debye decomposition procedure is discussed. Finally, the observed changes in the real and imaginary part of the electrical conductivity as a function of frequency, saturation and clay content are discussed and conclusions are drawn.

### 3.2 Materials and Methods

#### 3.2.1 Measurement setup

We developed an experimental setup for accurate SIP measurements on variably saturated porous media (Figure 3.1). The soil sample holder has a height of 10 cm and an inner diameter of 8 cm. Pressure was used to drain the samples in several steps. The advantage of drainage over evaporative drying is that the electrical conductivity of the pore fluid remains nearly constant during the experiment. The setup relies on a high-accuracy electrical impedance spectrometer described by Zimmermann et al. (2008). The electrical impedance over a frequency range from 1 mHz to 45 kHz was measured using a four-point electrode array by applying an alternating sinusoidal current to the sample using two bronze plate electrodes. The voltage and the phase shift between the applied current and measured voltage were determined using non-polarizing potential electrodes. For more details on the experimental set-up, see second chapter.

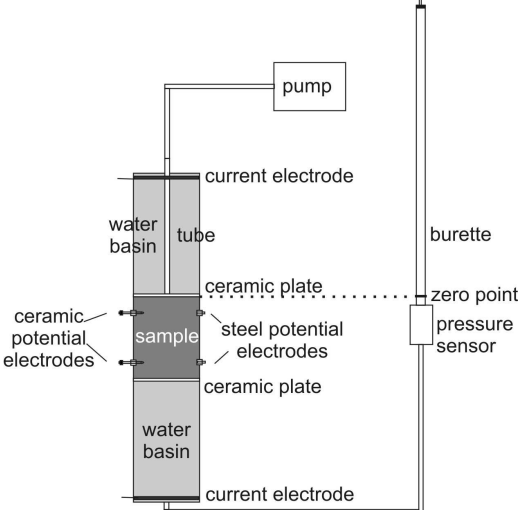


**Figure 3.1: Sketch of experimental setup: A pump is used to desaturate the sample using several pressure steps. Electrical measurements are conducted using a high-accuracy impedance spectrometer. The high air-entry porous ceramic cones of the non-polarizing potential electrodes are located in the sample to keep a good electrical contact.**

### 3.2.2 Sample preparation

We investigated the complex conductivity as a function of water saturation for pure sand and three sand-clay mixtures with 5, 10, and 20 weight-% clay content. The pure quartz sand used in all four samples had a medium grain size of 0.2 mm and a mass related specific surface area ( $S_m$ ) of  $0.104 \text{ m}^2 \text{ g}^{-1}$  determined using the BET method. For the sand-clay mixtures, a silt-clay mixture composed of 29% kaolinite, 18% illite and 47% quartz was added to the quartz sand. About 60% of the silt-clay mixture was smaller than  $2 \mu\text{m}$  and more than 96% was smaller than  $63 \mu\text{m}$ . The  $S_m$  of the silt-clay mixture was  $13.30 \text{ m}^2 \text{ g}^{-1}$ . A summary of the bulk density, porosity and estimated pore-volume related specific surface area ( $S_{por}$ ) of each of the four samples is provided in Table 3.1.

**Table 3.1. Petrophysical properties of the pure sand and the sand-clay mixtures.**

	Sand-clay mixtures			
	sand	5% clay	10% clay	20% clay
bulk density [ $\text{g}/\text{cm}^3$ ]	1.62	1.66	1.71	1.71
porosity [%]	39.02	36.05	34.22	34.10
estimated $S_{por}$ [ $\mu\text{m}^{-1}$ ]	0.43	3.44	6.55	13.70

To prepare the sample, the material was first moistened with tap water with a conductivity of  $450 \mu\text{S cm}^{-1}$  and then mixed so that the clay was well distributed in the sand. Some tap water was filled in the sample holder and a layer of about 5 mm of moistened sand-clay mixture was added. This procedure was repeated until the sample holder was filled. It was ensured that supernatant water was present at all times during the filling procedure. Small air bubbles were removed with a spoon during filling. The two non-polarizing ceramic potential electrodes were installed in the sample during the packing procedure to ensure good contact and limit soil disturbance by insertion.

At the beginning of each experiment, the filled sample holder was attached to the burette by a flexible tube. To fully saturate the sample, the water level in the burette was maintained above the top of the soil sample without applying pressure. After equilibrium was reached, the water level in the burette was leveled with the top of the sample and an SIP measurement was conducted. Next, the first pressure step was applied and the associated water outflow was monitored by determining the water level in the burette using a calibrated pressure transducer. When water outflow became negligibly small, it was assumed that hydrostatic equilibrium was reached and an SIP measurement was made on two consecutive days. If the complex electrical conductivity did not significantly change between consecutive days, the next pressure step was applied. The distribution of the pressure steps was chosen such that the sample was drained in small steps. This was considered to be important because preliminary experiments showed that changes in the complex electrical conductivity were substantial even for small changes in the water saturation. The experiment for the pure sand took about 1 month, while measurements on the sand-clay mixtures took about 3 months. At the end of each experiment, the sample was oven-dried to obtain the water content, bulk density and porosity. This information was combined with the measured water outflow to obtain the water content of the sample. All experiments were performed in an air-conditioned laboratory with a temperature of  $20 \pm 1^\circ\text{C}$ .

### 3.2.3 Data interpretation

The geometrical factor of the four-point electrode configuration was used to convert the measured impedance in complex electrical conductivity ( $\sigma^*(\omega)$ ), which can be written as

$$\sigma^*(\omega) = |\sigma| e^{i\varphi} = \sigma'(\omega) + i\sigma''(\omega), \quad (3.1)$$

where  $i^2 = -1$ ,  $\omega$  denotes the angular frequency ( $\omega = 2\pi f$  with frequency  $f$ ),  $\sigma'(\omega)$  is the real part of  $\sigma^*$ ,  $\sigma''(\omega)$  is the imaginary part of  $\sigma^*$ ,  $|\sigma|$  is the magnitude of  $\sigma^*$ , and  $\varphi$  is the phase of  $\sigma^*$ . The relationship between  $\varphi$ ,  $\sigma'(\omega)$  and  $\sigma''(\omega)$  is given by

$$\varphi(\omega) = \arctan\left[\frac{\sigma''(\omega)}{\sigma'(\omega)}\right] \approx \frac{\sigma''(\omega)}{\sigma'(\omega)}. \quad (3.2)$$

The last approximation is only valid for small phase values, i.e. below 100 mrad.

To characterize the measured electrical spectra, we used Debye decomposition as proposed by Morgan & Lesmes (1994) and adapted by Nordsiek & Weller (2008). In this procedure, the magnitude and phase spectra of complex resistivity ( $\rho^*(\omega) = 1/\sigma^*(\omega)$ ) are regarded as a superposition of a certain number ( $N$ ) of Debye spectra:

$$\rho^*(\omega) = \rho_0 \left( 1 - \sum_{k=1}^N m_k \left( 1 - \frac{1}{1 + i\omega\tau_k} \right) \right), \quad (3.3)$$

where each of the  $N$  Debye spectra is characterized by a chargeability  $m_k$  and a relaxation time  $\tau_k$ , and  $\rho_0$  is the DC resistivity. We used an extension of the Debye decomposition approach of Nordsiek & Weller (2008) proposed by Zisser et al. (2010), in which a weighting factor between the real and the imaginary part of the normalized complex resistivity was introduced. The discretization of the  $\tau$ -axis was chosen such that 100 relaxation times logarithmically spaced in the range from  $10^{-5}$  to  $10^5$  s were obtained. The effect of electromagnetic coupling at high frequencies was determined by fitting a Cole-Cole model to the high frequency data and these coupling effects were subsequently removed from the measured data by subtracting this fitted model, as previously proposed by Pelton et al. (1978).

## 3.3 Results and Discussion

The real part of the complex electrical conductivity,  $\sigma'$ , varied only marginally with frequency. Therefore,  $\sigma'$  is exemplarily shown at 1 Hz as a function of water saturation for the pure sand and the three sand-clay mixtures (Figure 3.2). For the 10% and 20% sand-clay mixtures, the saturation quickly dropped after the applied pressure was increased slightly above the air-entry pressure of the soil. Therefore, no complex conductivity measurements are available for saturations between 70% and 95% for these two sand-clay mixtures. Also, the maximum air pressure range that can be achieved with the experimental setup did not allow reaching saturations below 20% for the 10% and 20% sand-clay mixtures, which has led to a rather narrow saturation range where electrical measurements are available.

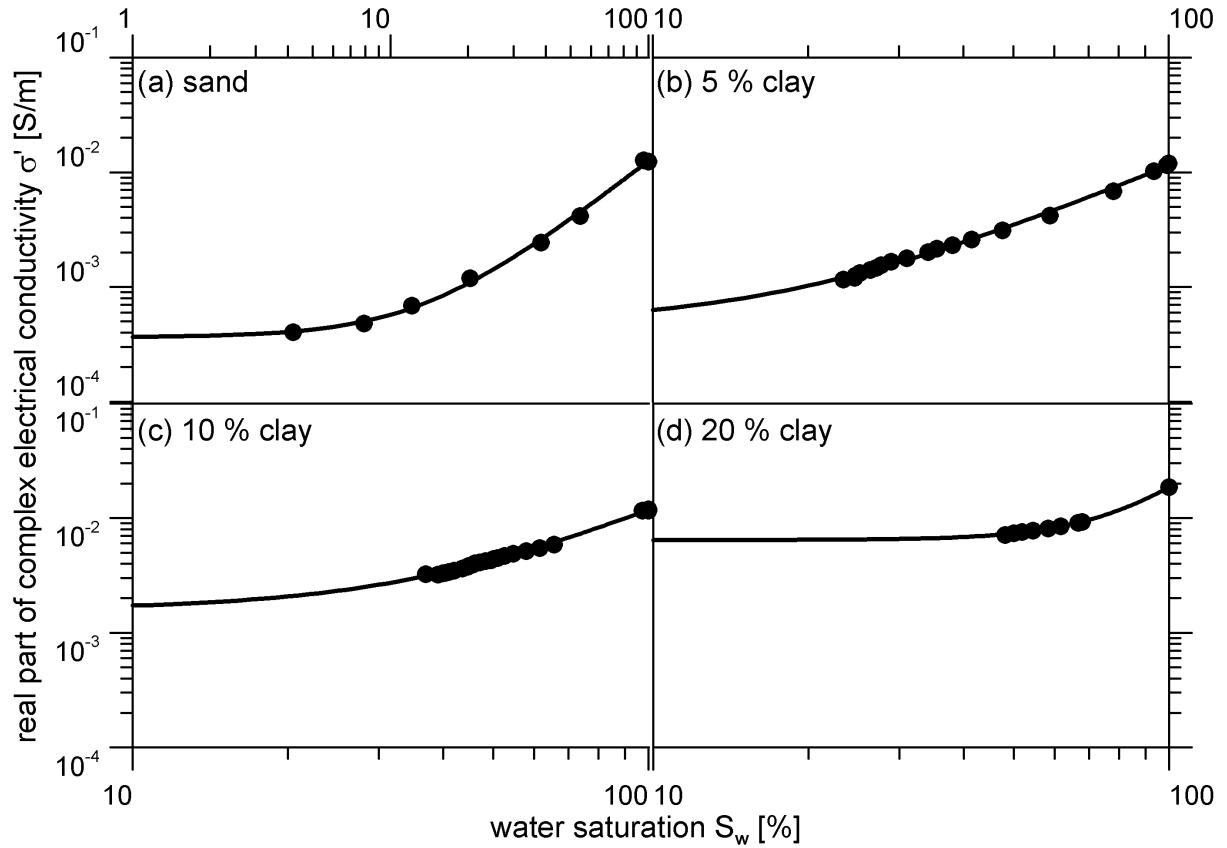


**Figure 3.2: Measured and modeled real part of the complex electrical conductivity ( $\sigma'$ ) at 1 Hz as a function of water saturation: (a) pure sand, (b) 5% sand-clay mixture, (c) 10% sand-clay mixture, and (d) 20% sand-clay mixture.**

The real part of the conductivity of a porous medium can be described by the model of Jougnot et al. (2010) based on Revil et al. (2007) for variably saturated conditions:

$$\sigma' = \frac{1}{F} \sigma_w S_w^n + \left( \frac{F-1}{F} \right) \sigma_s', \quad (3.4)$$

where  $F$  is the formation factor,  $\sigma_w$  is the conductivity of the pore fluid,  $S_w$  is the water saturation,  $n$  is the saturation exponent, and  $\sigma_s'$  is the real part of the surface conductivity. This model fits the real part of the conductivity well (Figure 3.2) with the parameters provided in Table 3.2. The  $\sigma_s'$  clearly increased with increasing clay content, which is reasonable given that most surface area is associated with the clay fraction (Ruffet et al., 1995; Brovelli et al., 2005). The fitted  $F$  increased from sand to 10% clay because the surface conductivity increased, while the real part of the bulk conductivity of the saturated samples remained approximately the same. For the 20% clay, there is an increase in both the real part of the bulk conductivity of the saturated sample and the surface conductivity, which led to a lower fitted formation factor. It is important to note that there is considerable uncertainty in the fitted formation factor because the release of ions from the clay can have increased  $\sigma_w$ . To which extent this occurred is not known and can, therefore, not be considered here. It was assumed that  $\sigma_w$  was equal for all four samples, which is reflected in the fitted  $F$ .

**Table 3.2: Fitted petrophysical model parameters (Eq. 4) for the pure sand and the sand-clay mixtures.**

	Sand-clay mixtures			
	sand	5 % clay	10 % clay	20 % clay
Formation factor, $F$ [-]	3.69	4.13	4.40	3.70
Saturation exponent, $n$ [-]	1.77	1.86	1.91	3.70
Surface conductivity, $\sigma_s'$ [ $\text{Sm}^{-1}$ ]	0.0005	0.0006	0.0021	0.0088

The fitted  $n$  showed a general tendency to increase with increasing clay content (Table 3.2). However, the sensitivity of  $n$  and  $\sigma_s'$  to small measurement errors in  $S_w$  and  $\sigma'$  is quite high for both the 10% and 20% clay samples because of the relatively narrow saturation range. High  $n$  values can be interpreted as an indication that the water phase is not well connected. Values well above 2 have been observed for oil-wet rocks where water does not coat the solid phase but is present as isolated pockets with minimum surface area (Keller, 1953; Sweeney & Jennings, 1960) and for rocks with disconnected microporosity where part of the conducting water phase is trapped in isolated regions (Sen, 1997). In contrast, low  $n$  are observed when the major current-carrying paths change little with saturation, such as in the case of a connected microporosity (Sen, 1997). The sand-clay mixtures investigated here can also be seen as a dual-porosity system and the increase of  $n$  with increasing clay content might, therefore, be interpreted as an indication that the connectedness of the water phase decreased with increasing clay content.

The frequency dependent imaginary part of the complex electrical conductivity,  $\sigma''(\omega)$ , of the pure sand as a function of water saturation  $S_w$  is presented in Figure 3.3. At high frequencies,  $\sigma''(\omega)$  clearly increases. Zimmermann et al. (2008) showed that the contact impedance of the potential electrodes in combination with the capacitive load of the amplifiers is the main source of phase errors for our measurement equipment and set-up. This will lead to an increase of  $\sigma''(\omega)$  at higher frequencies, which as a first approximation behaves like  $i\omega X$  (Zimmermann et al., 2008). This  $i\omega X$  behavior is illustrated by the dashed line in Figure 3.3, which was arbitrarily shifted to fit the lowest spectrum. Clearly, the spectra in Figure 3.3 can be nicely fitted by such a  $i\omega X$  relationship in the high frequency range. We interpret this as a clear indication that the increase in  $\sigma''(\omega)$  in this high frequency range is mostly due to measurement errors for this sand sample. A possible second source of an increase in  $\sigma''(\omega)$  in this frequency range is Maxwell-Wagner polarization, which can be described by mixing models based on the complex conductivity of the individual soil constituents (e.g. Chen & Or, 2006). However, we believe that this is of secondary importance here.

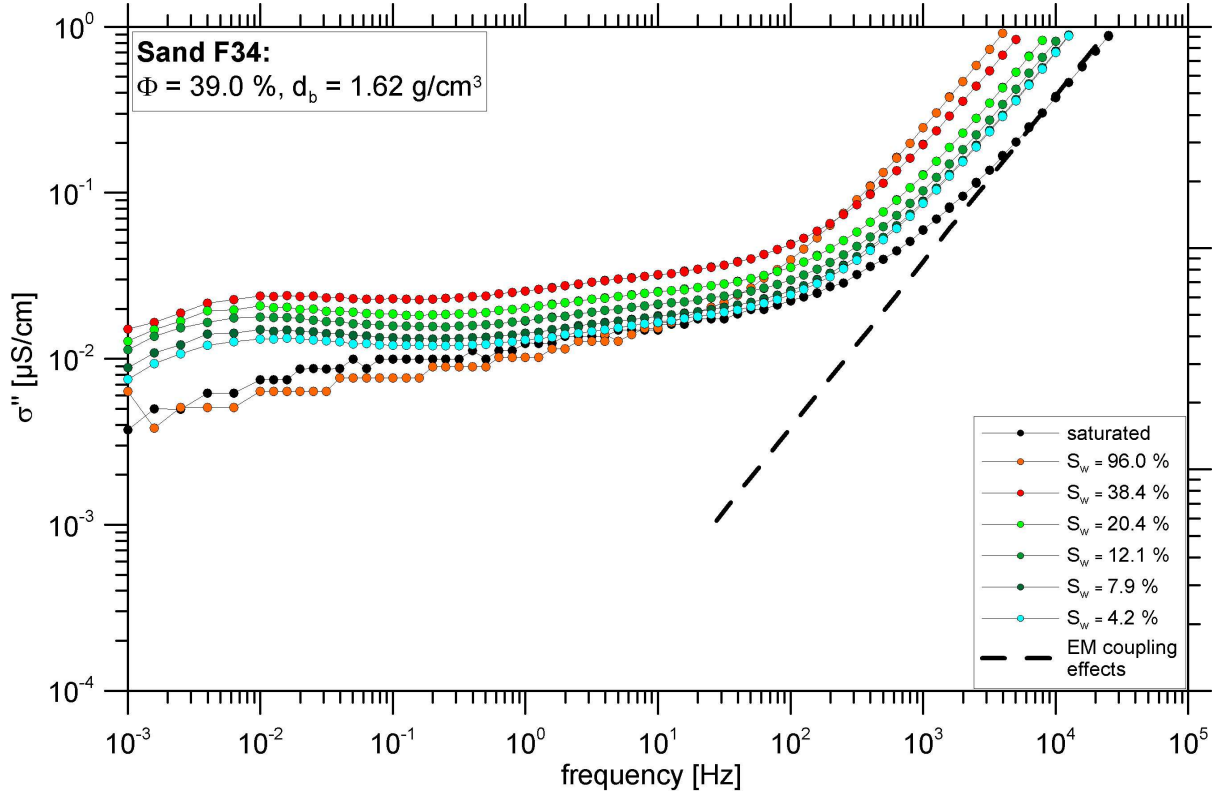


**Figure 3.3: Frequency-dependent imaginary part of the complex electrical conductivity ( $\sigma''$ ) of the investigated pure sand as a function of water saturation.**

For frequencies well below 1 kHz, the observed  $\sigma''(\omega)$  is not strongly affected by measurement errors associated with the electrode contact impedance. Here,  $\sigma''(\omega)$  first increased and then decreased with decreasing water saturation. In addition, a weak maximum of  $\sigma''(\omega)$  in the low-frequency range indicates a characteristic frequency ( $f$ ) at about 0.01 Hz for water contents below 54% water saturation. For higher saturation, such a maximum was not observed because of the extremely low phase angle ( $<0.1$  mrad) related to the low  $\sigma''(\omega)$  and relatively high  $\sigma'(\omega)$ . Such low phase angles are below the limit of what can be measured with our experimental setup. Titov et al. (2002) suggested the following relationship between grain diameter,  $d$  (in mm), and the characteristic frequency  $f$  (in Hz):

$$d = 0.09 \sqrt{\frac{1}{2\pi f}}. \quad (3.5)$$

Leroy et al. (2008) following the work of Schwarz (1962) suggested that  $d$  is related to the relaxation time,  $\tau$ , and the diffusion coefficient of the counter-ions ( $D_s$ ) in the Stern layer of the electrical triple-layer associated with the mineral surface:

$$\tau = \frac{d^2}{8D_s} \quad (3.6)$$

Leroy et al. (2008) further argued that  $D_s$  does not deviate strongly from the diffusion coefficient in the water phase for hydrated ions and used  $D_s = 2.45 \times 10^{-9} \text{ m}^2 \text{ s}^{-1}$ . By rewriting and substitution, this results in

$$d = \sqrt{8D_s\tau} = \sqrt{8D_s} \cdot \sqrt{\tau} = 0.140 \sqrt{\frac{1}{2\pi f}}. \quad (3.7)$$

Accordingly, a characteristic frequency of 0.01 Hz corresponds with an average grain size of 0.36 – 0.56 mm, which is above the median grain size diameter of 0.2 mm for the sand used in this study, but nevertheless in reasonable agreement given the uncertainty in  $D_s$ .

The imaginary conductivity spectra of the 5%, 10%, and 20% sand-clay mixtures showed a more complex behavior in dependence on saturation (Figure 3.4 - Figure 3.6). Again, the dashed lines indicate the expected  $i\omega X$  behavior related to the electrode contact impedance. The lines were shifted to fit the lowest spectrum for the highest frequency. In contrast to  $\sigma'(\omega)$  for the sand sample, the increase in  $\sigma''(\omega)$  above 1 kHz is not well described by  $i\omega X$  for the three sand-clay mixtures. Clearly,  $\sigma''(\omega)$  at these frequencies is not solely determined by measurement errors associated with the electrode contact impedance. This is further supported by the increasing deviation from  $i\omega X$  with increasing clay content.

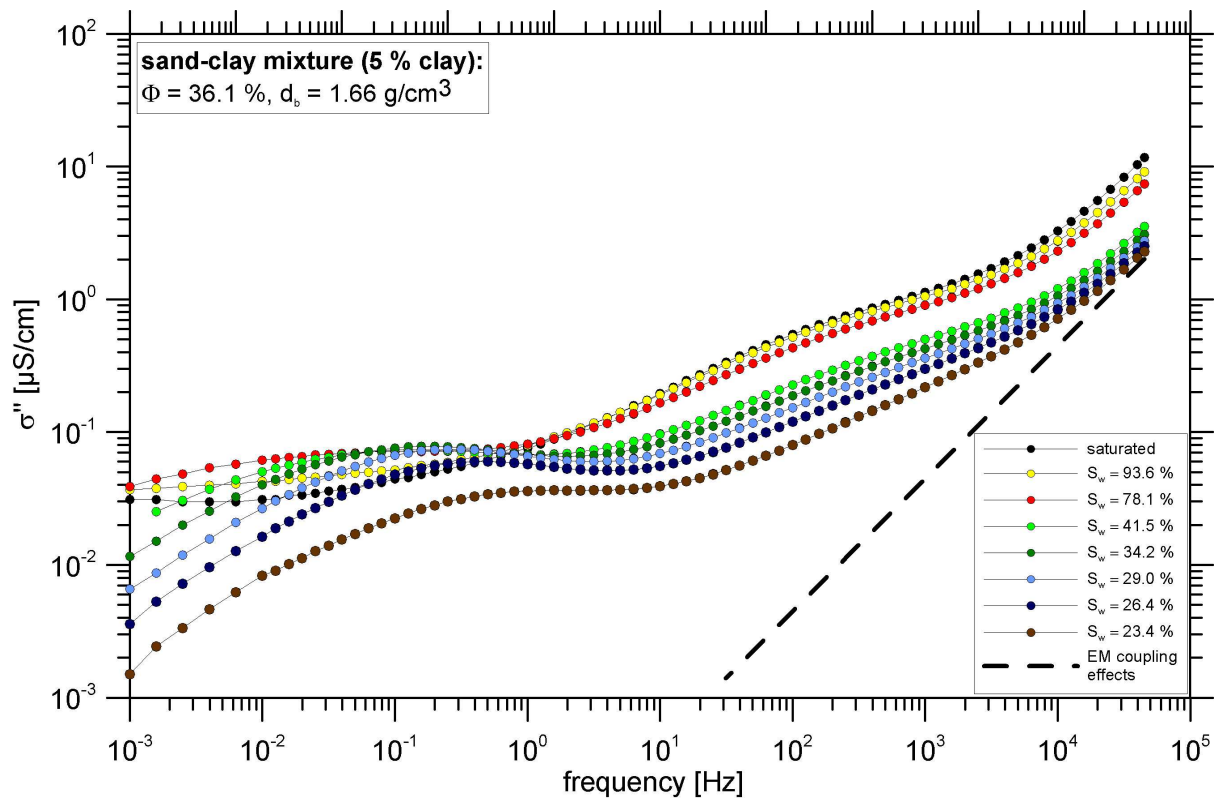


**Figure 3.4: Frequency-dependent imaginary part of the complex electrical conductivity ( $\sigma''$ ) of the investigated sand-clay mixture with 5% clay content as a function of water saturation.**

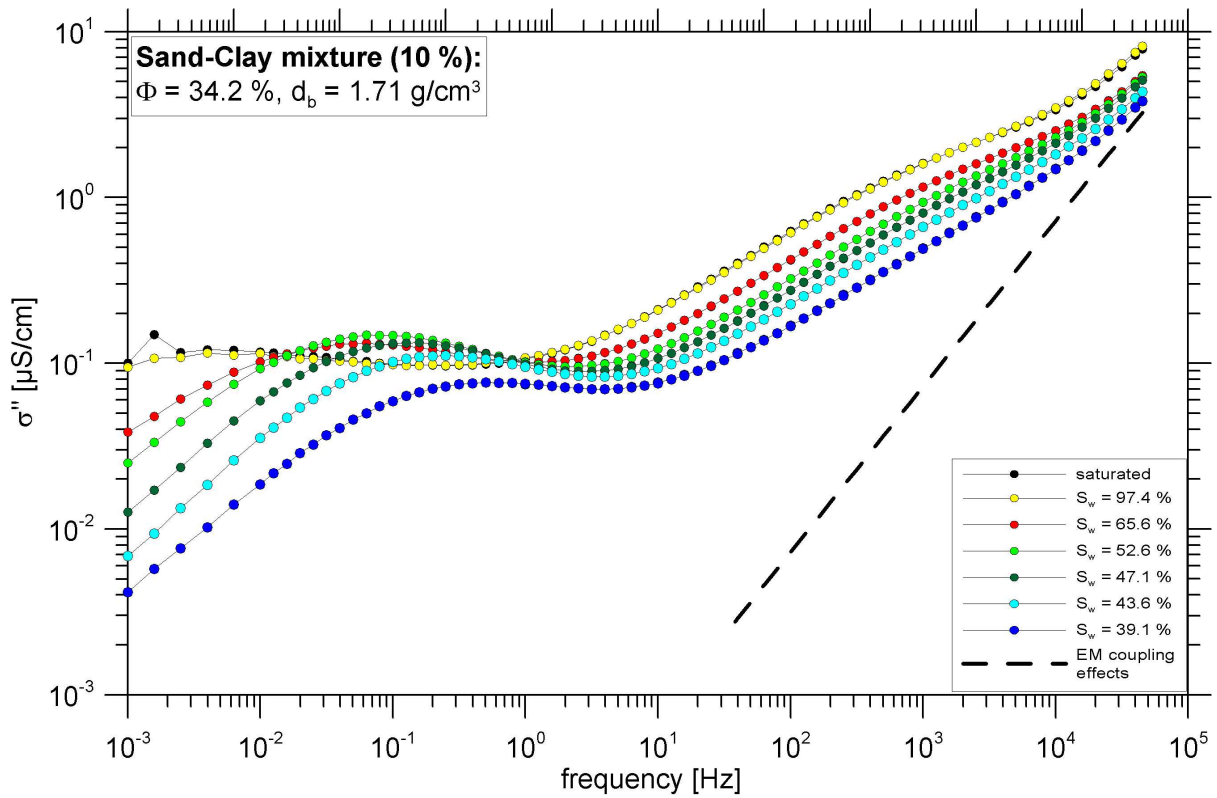


**Figure 3.5:** Frequency-dependent imaginary part of the complex electrical conductivity ( $\sigma''$ ) of the investigated sand-clay mixture with 10% clay content as a function of water saturation.

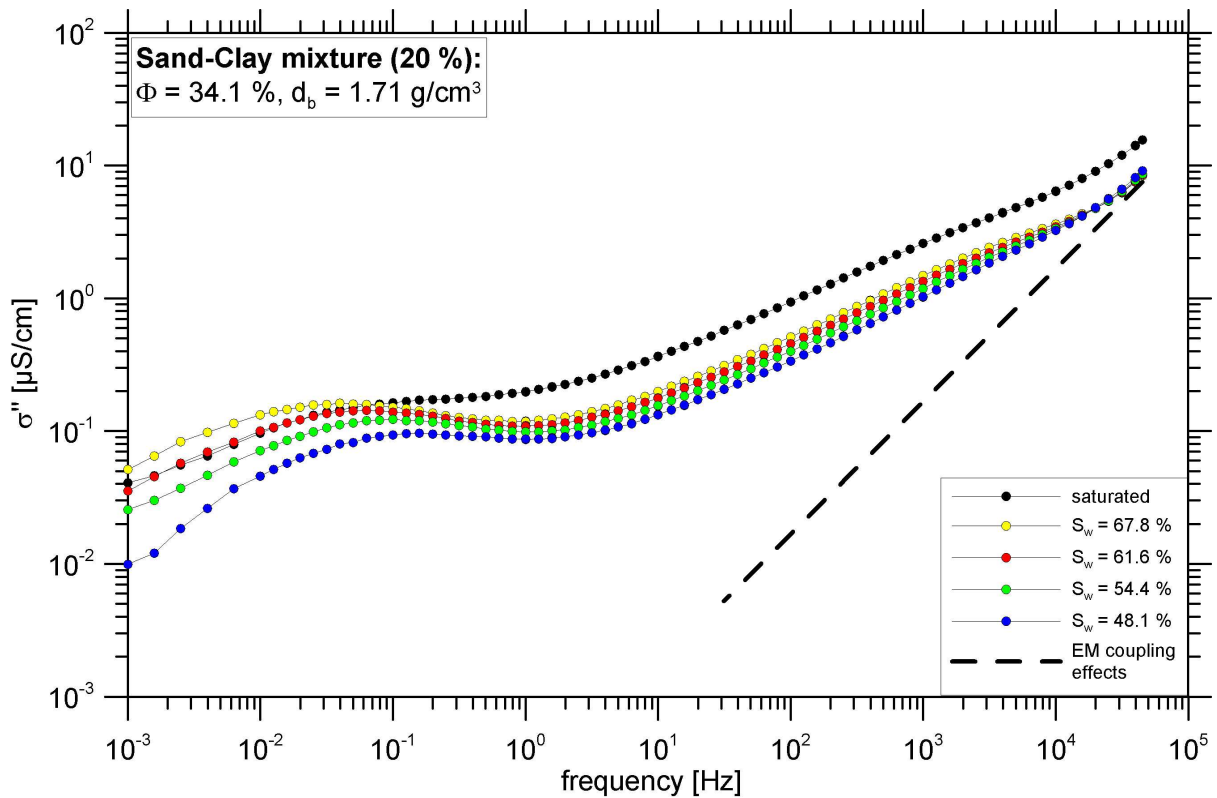


**Figure 3.6:** Frequency-dependent imaginary part of the complex electrical conductivity ( $\sigma''$ ) of the investigated sand-clay mixture with 20% clay content as a function of water saturation.

Lesmes & Morgan (2001) suggested that the relative proportion of grains with a certain size determine the magnitude of  $\sigma''(\omega)$  at a particular frequency. Therefore, we first inspect the behavior of  $\sigma''$  at 0.01 Hz (sand fraction) and 1 kHz (clay fraction according to Eq. 3.5) for the sand-clay mixtures (Figure 3.7). Similar to the pure sand,  $\sigma''$  again first increased and then decreased with decreasing water saturation at a frequency of 0.01 Hz for all investigated samples (Figure 3.7a). At a frequency of 1 kHz,  $\sigma''$  at full saturation increased with increasing clay content for the sand-clay mixtures (Figure 3.7b). With decreasing saturation,  $\sigma''$  at 1 kHz continuously decreased at a similar rate for all three sand-clay mixtures (Figure 3.7b). As outlined above,  $\sigma''$  at 1 kHz might be affected by the electrode contact impedance. The dashed lines in Figure 3.3 to Figure 3.6 indicate that this indeed is the case for the sand sample, but  $\sigma''$  of the sand-clay mixtures is not strongly affected because polarization from the sample is an order of magnitude larger than the expected  $\sigma''$  contribution of the contact impedance.

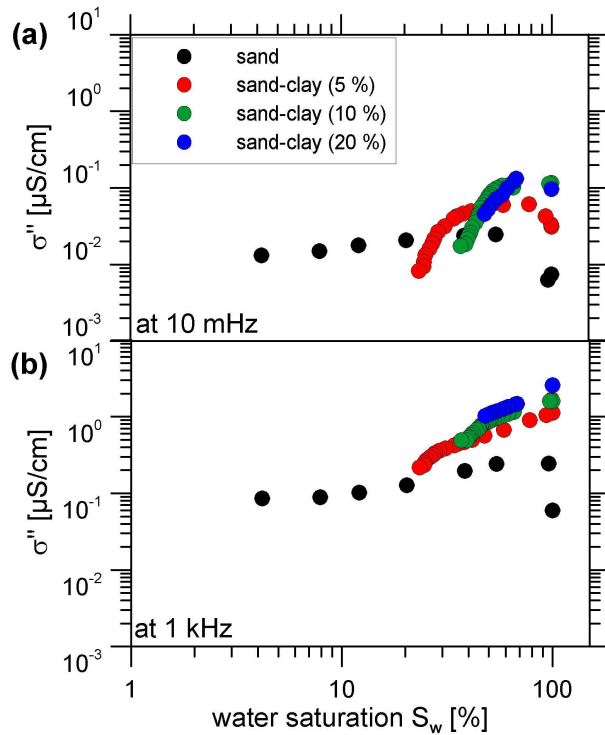


**Figure 3.7: Imaginary part of the complex electrical conductivity ( $\sigma''$ ) at a frequency of (a) 0.01 Hz and (b) 1 kHz for all samples as a function of water saturation.**

To further interpret the SIP measurements, the measured complex electrical conductivity spectra were analyzed using the Debye decomposition method of Zisser et al. (2010). In a first step, we present the normalized total chargeability ( $m_{n,tot}$ ) as a function of water saturation (Figure 3.8). The quantity  $m_{n,tot}$  is obtained by integrating the chargeability over the spectrum of relaxation times and normalizing this total chargeability by dividing it by  $\rho_0$ . Despite the similarity of  $m_{n,tot}$  with the metal factor used in mineral exploration, which is typically interpreted as a proxy for  $\sigma''$ , Weller et al. (2010) recently showed that  $m_{n,tot}$  contains additional information regarding the polarizability of the mineral-fluid interface per unit surface area as compared to  $\sigma''$ . For the saturated sand and sand-clay mixtures,  $m_{n,tot}$  increased with increasing clay content, which is expected because of the larger specific surface area of the clay minerals. During drainage of the sample,  $m_{n,tot}$  first increased for the sand and the 5% sand-clay mixture, and then decreased again.  $m_{n,tot}$  of the other two sand-clay

mixtures (10% and 20% clay) seemed to have remained relatively constant upon desaturation initially, but then decreased rapidly. However, this is somewhat uncertain due to a lack of electrical measurements. Generally, the behavior of  $m_{n,tot}$  is consistent with the interpretation of  $\sigma'$  provided earlier.

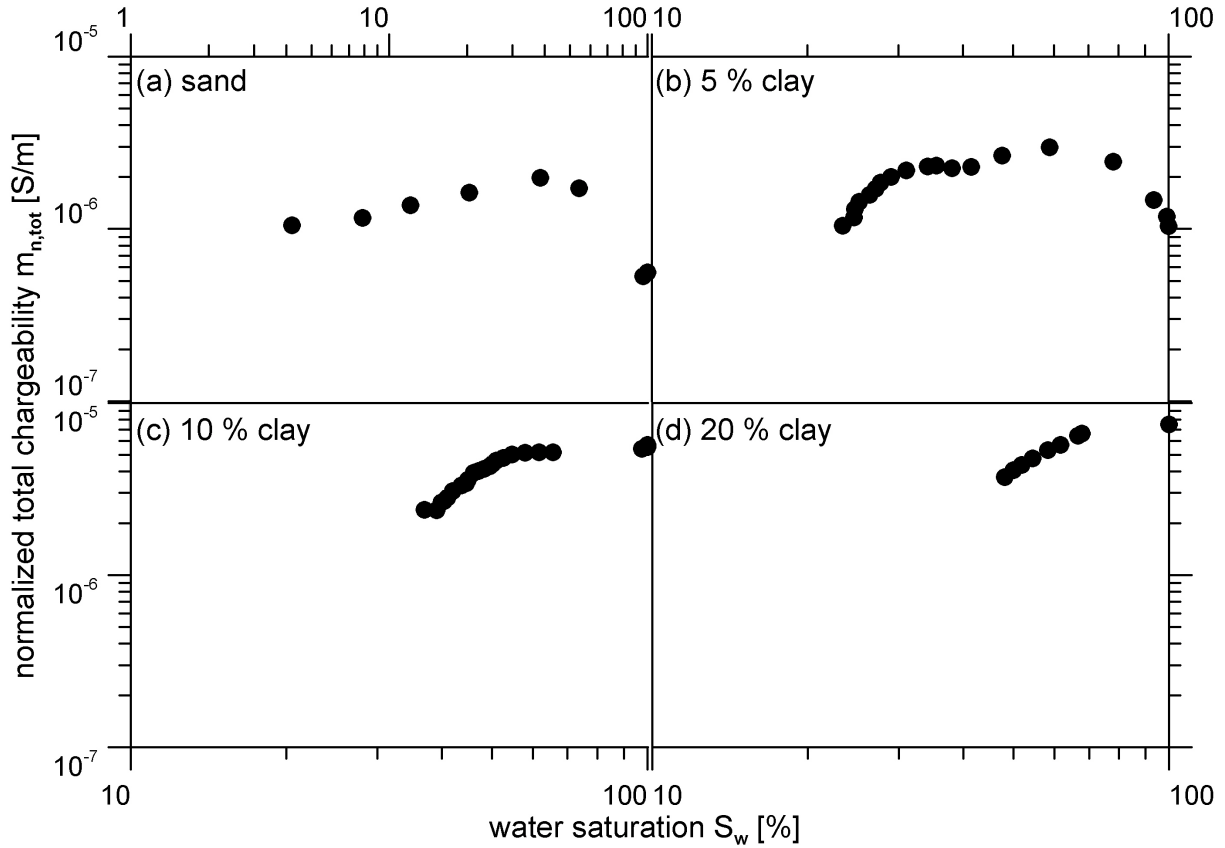


**Figure 3.8: Normalized total chargeability ( $m_{n,tot}$ ) of all samples as a function of water saturation.**

It is interesting to note that a maximum in  $m_{n,tot}$  at moderate saturation for the pure sand (Figure 3.8) occurred in a water saturation range where the relationship between  $\log(\sigma')$  and  $\log(S_w)$  also showed a change in slope because of the increasing importance of surface conductivity (Figure 3.2). This was also observed by Titov et al. (2004) for pure sands. However, the maximum in  $m_{n,tot}$  was at a water saturation of about 38% for the pure sand in this study, whereas the maximum in chargeability reported by Titov et al. (2004) occurred at a lower saturation of 18%. In addition, for the 5% sand-clay mixture two local maxima instead of one maximum were observed for  $m_{n,tot}$  (Figure 3.8). For the 10% and 20% sand-clay mixtures, a maximum in  $m_{n,tot}$  is not observed.

We propose the following conceptual model to explain the variation of  $\sigma'(\omega)$  and  $m_{n,tot}$  for the sand-clay mixtures. It is based on the assumption that  $\sigma'(\omega)$  and  $m_{n,tot}$  can be interpreted simply as a superpositioning of two individual conceptual models for the sand and clay fraction (both illustrated in Figure 3.9). The conceptual model of the sand fraction is based on the short-narrow pore model of Titov et al. (2002, 2004). This model proposes that the intergrain pore spaces act as large pores, while the grain contact regions act as narrow pores in a saturated porous medium (Figure 3.9a). As the electrical current follows the way of minimum resistance, most of it flows through the bulk solution and only a small amount of current flows through the polarizable part of the cells near the grain contacts. With decreasing

saturation, the largest pores are desaturated while water remains at the grain contacts. Therefore, the grain contact regions become the large pores, while the water films around the sand grains act as narrow pores (Figure 3.9c). Since the electrical current flow cannot by-pass the polarizable part of the cells near the grain contacts anymore, Titov et al. (2002, 2004) postulated that the chargeability must first increase with decreasing saturation. With a progressing decrease in water saturation, the amount of water in the grain contact regions is reduced, which results in a decrease of the difference between the effective pore diameters associated with grain contacts and water films, and thus to a decrease in chargeability with decreasing saturation (Figure 3.9d) as observed for all sand-clay mixtures (Figure 3.7a).

The conceptual model for the clay fraction (also Figure 3.9) is an attempt to explain the continuous decrease of  $\sigma''$  at 1 kHz observed in the presence of clay (Figure 3.7b). When the sand-clay mixtures are fully saturated, we speculate that the clay particles are loosely arranged in the water-filled pores (Figure 3.9a). Although such an arrangement is not typically observed for natural soils, we believe that this a realistic assumption for the packed sand-clay mixtures used in this study. With decreasing water saturation, the clay particles are rearranged into a smaller available water-filled pore volume (Figure 3.9b). Apparently, this rearrangement results in a decrease of the specific surface area of the clay minerals, and an associated decrease of  $\sigma''$  at a frequency of 1 kHz (Figure 3.7b).

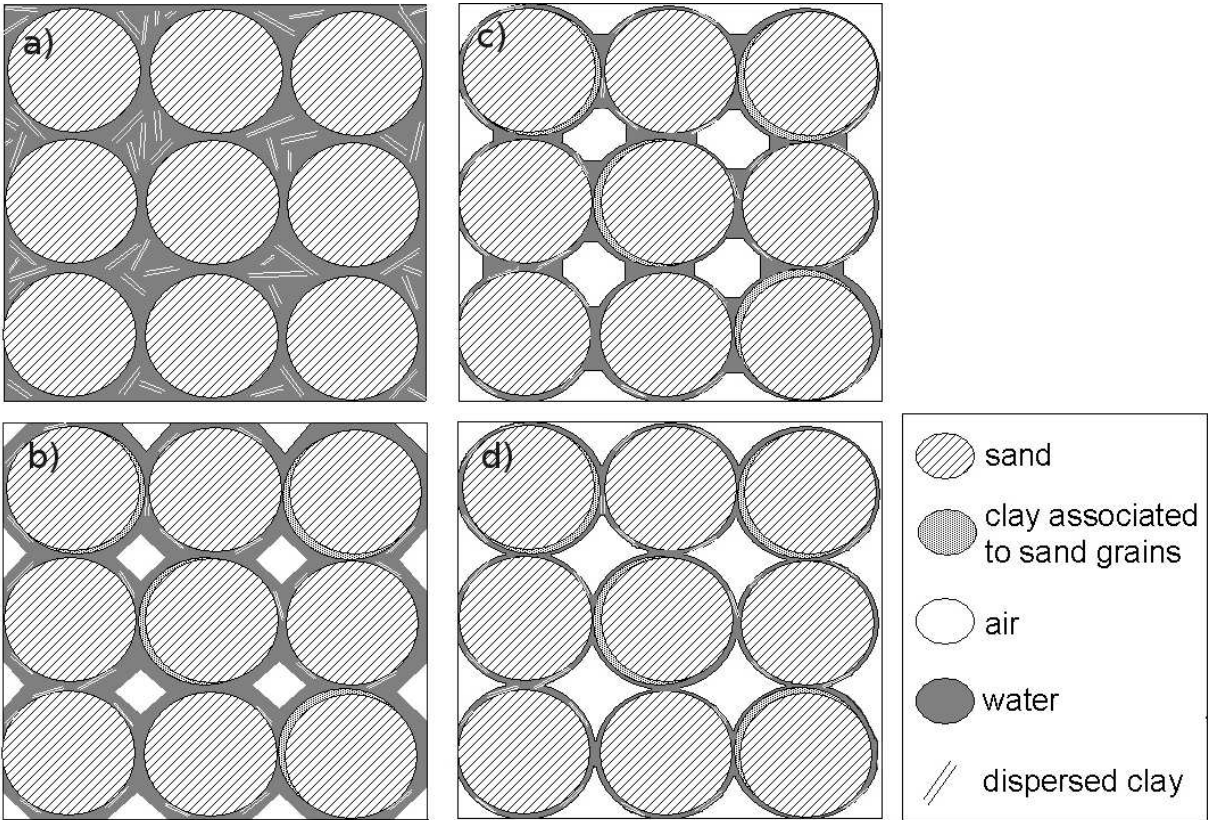


**Figure 3.9: Conceptual model for electrical response associated with unsaturated sand-clay mixtures. a) Full saturation: Intergrain pore spaces act as large pores, while the grain contact regions act as narrow pores. The clay minerals are mainly loosely arranged within the entire saturated pore space. b) Medium saturation: The clay minerals are rearranged into a smaller available saturated pore volume. Some of the clay particles are associated with the sand grains. c) Low saturation: Grain contact regions become the large pores, while the water films around the sand grains act as**

**narrow pores. d) Dry soil: The amount of water in the grain contact regions is reduced, resulting in a decreased difference between effective pore radii associated with grain contacts and water films.**

With increasing clay content, the polarization associated with the clay fraction increases. Therefore, we postulate that the maximum in  $m_{n,tot}$  associated with the sand fraction disappears for mixtures with high clay content because the initial increase in chargeability with decreasing saturation of the sand fraction is overwhelmed by the continuous decrease of chargeability with decreasing saturation for the clay fraction. In addition, we tentatively hypothesize that the stronger increase of  $m_{n,tot}$  with decreasing water saturation of the 5% sand-clay mixture is related to interaction of the sand grains with the clay minerals (Figure 3.9b-d). As argued above, desaturation is likely to go along with a reordering of the clay particles in the pore space, and we speculate that some of the clay became associated with the sand grains, thus leading to increased values of  $\sigma''$  at 0.01 Hz (Figure 3.7a) and a steeper increase of  $m_{n,tot}$  upon initial desaturation (Figure 3.8).

The relaxation time distribution obtained using the Debye decomposition procedure was interpreted using the relaxation time associated with the peak of the distribution ( $\tau_{peak}$ ). An example of how the relaxation time distribution changes with saturation is provided in Figure 3.10 for the 5% sand-clay mixture.

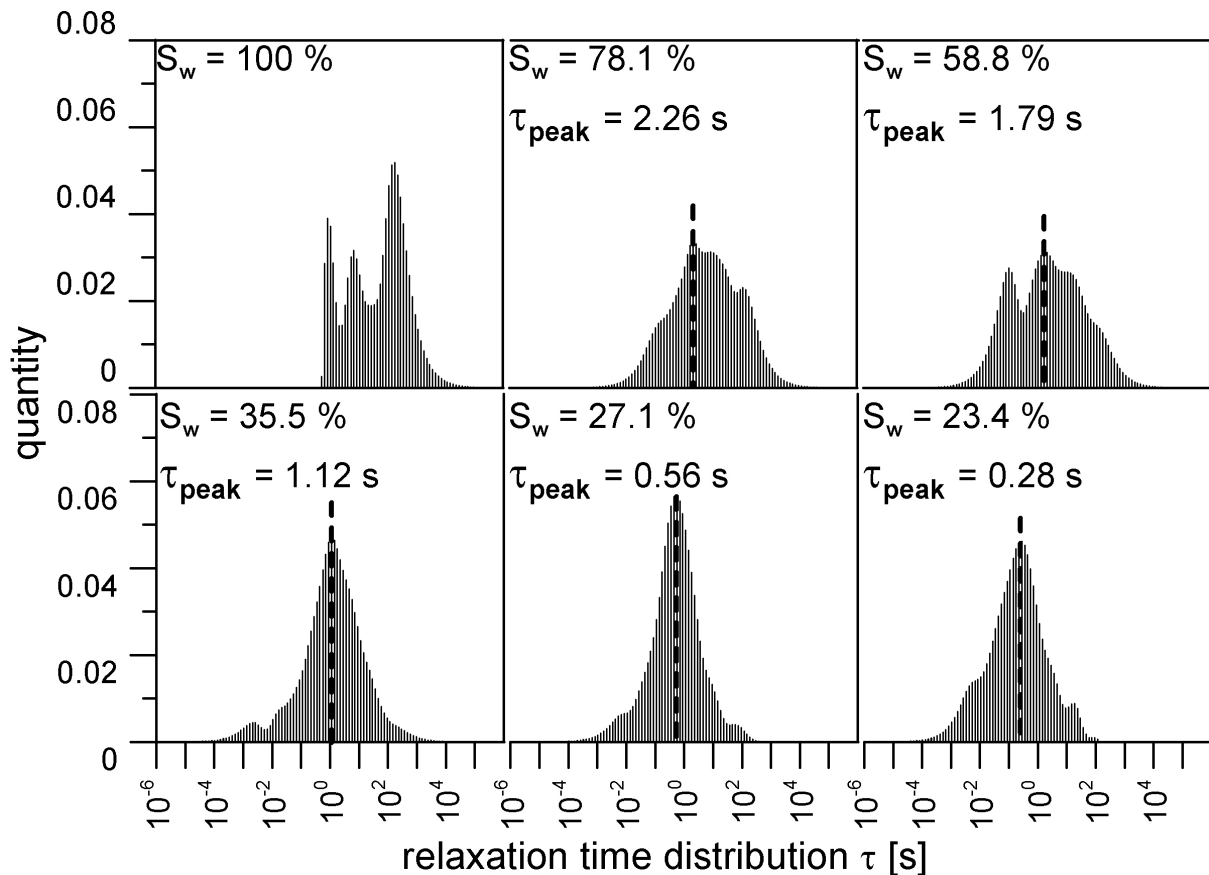


**Figure 3.10: Estimated peak relaxation time ( $\tau_{peak}$ ) from the  $\tau$  distribution obtained with Debye decomposition for different water saturations of the 5% sand-clay mixture.**

It should be noted that not all SIP measurements were included in the  $\tau_{peak}$  analysis because of the low polarizability that prohibited useful estimates of  $\tau_{peak}$  for high water saturations. For

the pure sand,  $\tau_{\text{peak}}$  varied in the range from 10 to 50 s and tended to decrease with saturation (Figure 3.11). The  $\tau_{\text{peak}}$  values obtained for the sand-clay mixtures ranged between 0.2 to 6 s, which is a wider range than for the pure sand, and strongly decreased with decreasing water saturation. The associated length scales according to Eqs. (3.5) and (3.7) vary from 0.28 mm to 0.99 mm for the pure sand sample and from 40  $\mu\text{m}$  to 343  $\mu\text{m}$  for the sand-clay mixtures. Although the length scale for sand approximately matches the sand grain size, the length scale for the sand-clay mixtures is in a size range where almost no grains are present (maximum of  $\sim 0.2\%$  for the 5% sand-clay mixture).

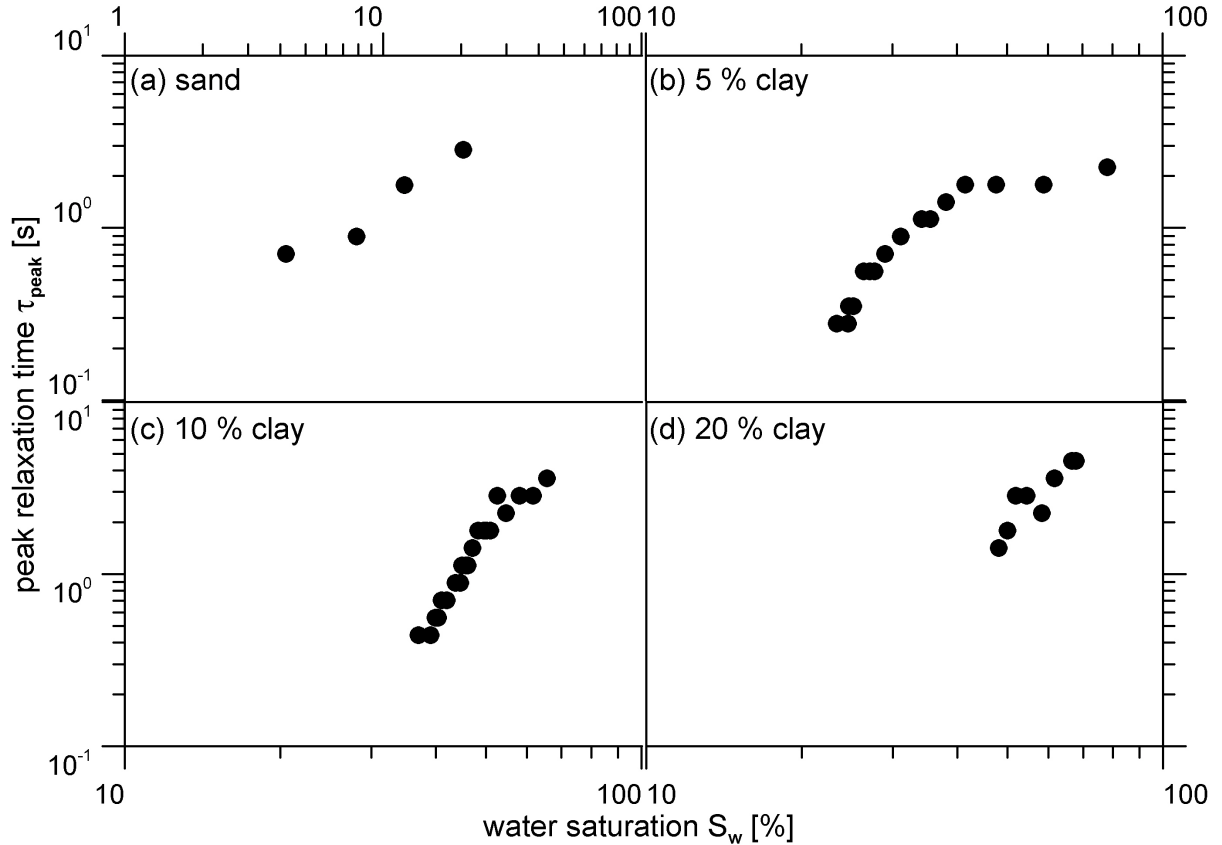


**Figure 3.11: Peak relaxation time ( $\tau_{\text{peak}}$ ) of all samples as a function of water saturation.**

The results for the dependence of  $\tau_{\text{peak}}$  on water saturation (Figure 3.11) are clearly not consistent with the measurements and model of Jougnot et al. (2010). Our data clearly show a decrease of  $\tau_{\text{peak}}$  with decreasing saturation, which is not consistent with models that assume that the relaxation time is closely associated with the dominant particle fraction and diffusion of ions in the Stern layer (e.g. Leroy et al., 2008; Jougnot et al., 2010). Our observations do agree with Binley et al. (2005) who also reported a decrease in relaxation time with decreasing saturation. Intuitively, the reduction in relaxation time with decreasing saturation can easily be explained by the fact that pore sizes that still contain water (and therewith polarization length scales) become smaller and smaller during desaturation (Kemna et al., 1999; Kemna, 2000; Binley et al., 2005). Therefore, we feel that these measurements on variably saturated sand-clay mixtures seem to indicate that the polarization processes determining the complex electrical conductivity are related to pore sizes and not grain sizes. This is further supported by the length scales associated with the relaxation times of the sand-clay mixtures, and the larger range of  $\tau_{\text{peak}}$  values for the sand-clay mixtures as compared to

the pure sand, which is a reflection of the wider range of pore diameters present in the sand-clay mixtures as compared to the pure sand, which only has a small range of pores.

### 3.4 Conclusions

We investigated the SIP properties of variably saturated sand and sand-clay mixtures using a novel measurement set-up allowing pressure drainage and SIP measurements with a high accuracy. The SIP spectra were interpreted by Debye decomposition, which provided a relaxation time distribution and a chargeability distribution that was converted to a normalized total chargeability ( $m_{n,tot}$ ). The results showed that  $m_{n,tot}$  of the fully saturated samples increased with increasing clay content due to the larger specific surface area of the clay minerals. Using this dependence, it might be possible to determine the clay content of different saturated materials from  $m_{n,tot}$ . In addition, we found that  $m_{n,tot}$  first increased and then decreased upon desaturation for the pure sand and the 5% sand-clay mixture. Just as Titov et al. (2004), we found that the maxima of  $m_{n,tot}$  coincided with changes in the slope of  $\log\sigma'$  versus  $\log S_w$  (i.e. changes in the saturation exponent). The  $m_{n,tot}$  values for the 10% and 20% sand-clay mixtures only decreased with saturation.

The behavior of  $\sigma''(\omega)$  and  $m_{n,tot}$  for the sand and sand-clay mixtures were explained using a superpositioning of two individual conceptual models for the sand and clay fraction. The conceptual model of the sand fraction is based on the short-narrow pore model of Titov et al., (2002, 2004), which explains the initial increase and subsequent decrease of  $m_{n,tot}$  with decreasing saturation. The conceptual model for the clay fraction assumes a rearrangement of the clay in the water-filled pore space with decreasing saturation, and an associated decrease in specific surface area and polarizability. This explains the decrease of  $m_{n,tot}$  with decreasing saturation for the 10% and 20% sand-clay mixtures

The relaxation time,  $\tau_{peak}$ , decreased strongly with decreasing water saturation for the sand-clay mixtures, but only showed a tendency to decrease for the pure sand. The decrease of  $\tau_{peak}$  with decreasing water saturation can intuitively be explained by the decrease of the sizes of the active pores during the desaturation process. The strong decrease in relaxation time in the sand-clay mixtures was attributed to the wider range of pores as compared to the pure sand. These results have implications for direct attempts to estimate saturated hydraulic conductivity from the relaxation time. In pure sand or sandstone with a narrow pore size distribution, it might, as a first approximation, be reasonable to use relaxation times determined on unsaturated samples to estimate saturated hydraulic conductivity. However, for samples with a wide pore size distribution, this will not be a reasonable approximation and clearly the relaxation times obtained for unsaturated samples should first be corrected to an equivalent relaxation time at saturation before an estimation of saturated hydraulic conductivity can be done. It might also be possible to relate the relaxation time for an unsaturated sample directly to the unsaturated hydraulic conductivity. This will be explored in a follow-up study.

Finally, the strong decrease of the peak relaxation time with decreasing water saturation suggests that the application of grain-size based mechanistic models, such as described by Jougnot et al. (2010) and Schmutz et al. (2010) do not capture the behavior of our samples because these models predict that relaxation time does not change with water saturation. Instead, mechanistic models that explain SIP properties from polarization in the pore space seem warranted to explain the measurements on variable saturated porous media presented here.



## 4 Electrical-hydraulic relationships of unsaturated sand-clay mixtures using spectral induced polarization<sup>‡</sup>

### 4.1 Introduction

Hydraulic conductivity is a key parameter in several branches of earth sciences and engineering, such as hydrogeology, soil science, geotechnics, and petroleum engineering. By controlling the magnitude of flow, the hydraulic conductivity is important for the protection of groundwater aquifers, the remediation of contaminated sites, and the long-term storage of toxic or radioactive materials to name but a few examples.

Saturated hydraulic conductivity depends both on porous medium properties, such as porosity, pore size, pore structure, and tortuosity (Dias et al., 2008), as well as on the properties of the fluid (i.e., density and viscosity). For the determination of the saturated hydraulic conductivity,  $K_s$ , two general approaches are available: an empirical and an experimental approach. The empirical approach attempts to estimate hydraulic conductivity from soil physical properties that are more widely available and easier to measure, such as pore size distribution (Shepherd, 1989), grain size distribution, and soil texture (Wösten et al., 2001; Vereecken et al., 2010). The experimental approaches are based on Darcy's law and can be classified in laboratory and field methods. These experiments typically use a hydraulic excitation of the system and the reaction of the system is interpreted in terms of saturated hydraulic conductivity using analytical or numerical modeling techniques (see for example Dane & Topp, 2002). However, a disadvantage of all experimental approaches is that they are time-consuming and supply only local information.

In the last two decades, geoelectrical methods with alternating current like Induced Polarization (IP) and Spectral Induced Polarization (SIP) have shown promising results to determine hydraulic properties of rocks (Börner et al., 1996) and unconsolidated sediments (Slater & Lesmes, 2002). These methods determine complex electrical resistivity for a single frequency (IP) or across a broad frequency range (SIP) from the ratio and phase shift between induced sinusoidal current signals and measured voltage signals. The real part of the complex electrical resistivity is a measure for ohmic conduction in the porous medium. The imaginary part of the electrical resistivity is a measure for polarization processes occurring in the sample. These polarization effects depend on the specific surface (e.g., Börner & Schön, 1991; (Weller et al., 2010, 2011), the cation exchange capacity (e.g. Vinegar & Waxman, 1984; Scott & Barker, 2006), grain size distribution (e.g. Revil & Florsch, 2010), pore size distribution (e.g., Titov et al., 2002; Binley et al., 2005), pore-throat size (Scott & Barker, 2003), tortuosity (e.g., Titov et al., 2002, 2004; Kruschwitz et al., 2010), electrical conductivity (e.g., Weller et al., 2010; Kruschwitz et al., 2010) and chemical composition of the pore fluid (Weller et al., 2010; Vaudelet et al., 2011a, 2011b).

In more detail, polarization effects in porous media can be understood as follows. Due to the application of electric current, ions are moved from their original position in the pore space and move in the direction of the electrical field. The distance that ions move away from their original position is the relaxation length and the time which is required to cover this distance is the relaxation time. Relaxation processes are governed by polarization mechanisms in the electrical double layer (*EDL*) occurring at the interface between the solid phase and the

---

<sup>‡</sup> Adapted from K. Breede, A. Kemna, O. Esser, E. Zimmermann, H. Vereecken, and J.A. Huisman. Electrical-hydraulic relationships of unsaturated sand-clay mixtures using spectral induced polarization. Will be submitted to Vadose Zone Journal

electrolyte. At this interface, an EDL consisting of the Stern layer and the diffuse layer is formed due to diffusive and electrostatic forces. In porous media like soils, the solid surface usually has a negative charge that is counterbalanced by the positive charge of the Stern and diffuse layer. The thickness of this electrical double layer usually remains thin with respect to the size of the pore throats and the grain size (Revil & Florsch, 2010).

There are different polarization mechanisms like electrode polarization, membrane polarization and interface polarization that might act in the mHz to kHz frequency range. The latter one, also called Maxwell-Wagner effect, is important at kHz frequencies and higher. For frequencies smaller than 1 kHz, polarization is related to redistribution of ionic charge in the EDL. There are two prevailing views concerning the dominant polarization mechanism for IP and SIP: the granular model (e.g., Lesmes & Morgan, 2001; Leroy et al., 2008; Revil & Florsch, 2010) and the pore model (e.g., Titov et al., 2002; Scott & Barker, 2003; Binley et al., 2005). The most recent version of the granular model assumes that polarization is rooted in tangential movement of ions in the Stern layer of the EDL (Revil & Florsch, 2010). For this model, relaxation time is related to the ion diffusion coefficient ( $D$ ) and the grain radius ( $R$ ), according to the equation of Schwarz (1962):

$$\tau = \frac{R^2}{2D} \quad (4.1)$$

The pore model is based on local ion concentration gradients occurring in areas of pore radii variation (Titov et al., 2004). For this model, the relaxation time is related to the ion diffusion coefficient ( $D$ ) and the characteristic diffusion length ( $l$ ) (Kormiltsev, 1963):

$$\tau = \frac{l^2}{4D} \quad (4.2)$$

If the narrow pore is much shorter than the large pore,  $l$  is equal to the length of the narrow pore (Titov et al., 2004).

In both models, electrical relaxation times are related to important characteristic length scales in porous media that are known to exert key controls on the hydraulic conductivity. Indeed, promising relationships between the electrical relaxation time and the saturated hydraulic conductivity have been observed for instance by Binley et al. (2005) and Kemna et al. (2005). Both studies suggested that the relaxation time distribution depends on the pore size distribution of the soil and that it might be possible to determine the unsaturated hydraulic conductivity from the relaxation time distribution. However, we are not aware of any studies correlating the relaxation time with the unsaturated hydraulic conductivity. In previous work (Breede et al., 2011), we presented a new measurement setup for joint hydraulic and electric measurements on unsaturated porous media. Measurements with a pure sand illustrated the ability of this new joint measurement setup for accurate SIP measurements on unsaturated porous media. Breede et al. (2012) studied the dependence of SIP on water saturation for a pure sand sample and three sand-clay mixtures. It could be shown that the peak relaxation time decreased with decreasing water saturation and that the frequencies for which phase maxima occurred could not be correlated to grain sizes that were available in the samples.

The aim of this study is to investigate relationships between SIP and the unsaturated hydraulic conductivity using the measurements previously analyzed in Breede et al. (2012) with respect to water content. The remainder of the paper is organized as follows. First, we present our experimental setup for combined electrical and hydraulic measurements and describe the sample properties and our experimental approach to characterize their hydraulic and electrical properties. Next, we discuss relationships between SIP and the unsaturated hydraulic

conductivity in the results and discussion section. In the final section, the main conclusions of our study are presented.

## 4.2 Materials and Methods

### 4.2.1 Measurement setup

Electrical and hydraulic measurements were conducted using a joint measurement setup that is described in detail by Breede et al. (2011). A simplified sketch of the set-up is shown in Figure 4.1. The measurement column consisted of three parts: a sample holder with a height of 10 cm and a diameter of 8 cm, which was located in-between two water reservoirs that were separated from the sample by ceramic plates with a thickness of 0.7 cm and a high air-entry pressure that ensured that they remained saturated throughout the experiment. Porous bronze plate electrodes for the current injection were located at the top of the upper water reservoir and the bottom of the lower reservoir. Two non-polarizable electrodes for the current measurement were located in the sample holder with the ceramic tip in direct contact with the sample to ensure a good contact even when the sample was relatively dry. Pressure was applied in several steps to the sample via a tube that was connected to the top of the sample through the top ceramic plate as is commonly done in so-called Multi-Step Outflow (MSO) experiments (for details see van Dam et al., 1994). The water outflow from the sample flowed into a burette, and the water height in the burette was recorded continuously so that the water content of the sample could be calculated at all times. The advantage of pressure drainage over evaporative drying is that the electrical resistivity of the pore fluid remains almost constant.

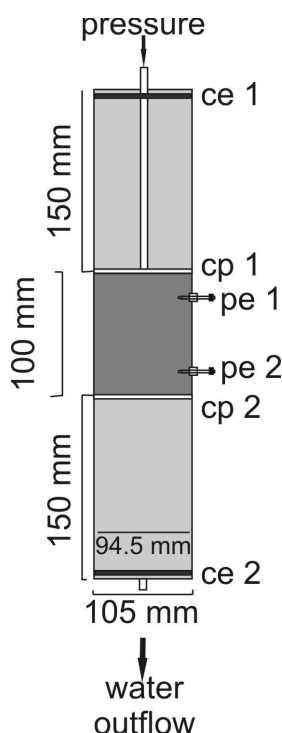


**Figure 4.1: Simplified sketch of the measurement column for joint hydraulic and electric measurements: Ce 1 and ce 2 are current electrodes being porous bronze plate electrodes. Cp1 and cp2 are ceramic plates with an air-entry pressure of 1 bar. Pe1 and pe2 are non-polarizable electrodes consisting of a Plexiglas tube filled with a calcium chloride solution and having a ceramic cone with an air-entry pressure of 1 bar.**

The electrical measurements were conducted with a high-accuracy electrical impedance spectrometer described by Zimmermann et al. (2008). A sinusoidal alternating current signal was injected at two the porous bronze plate electrodes and the voltage was measured between the two non-polarizing ceramic electrodes. This equipment allowed us to measure the complex electrical resistivity in a frequency range from 1 mHz to 45 kHz with a phase accuracy better than 0.1 mrad up to 1 kHz and 1 mrad above 1 kHz.

#### 4.2.2 Sample characterization

One pure sand and three additional artificially mixed sand-clay mixtures with 5, 10, and 20 weight-% clay were used for our study. The same pure quartz sand was used in all four samples and it had an average grain radius ( $r$ ) of 0.1 mm and a mass related specific surface ( $S_m$ ) of  $0.104 \text{ m}^2 \text{ g}^{-1}$ . The ‘clay’ fraction actually is a silty-clay mixture with 29% kaolinite, 18% illite, and 47% quartz. The mass related specific surface of the clay fraction was  $13.30 \text{ m}^2 \text{ g}^{-1}$ . Both specific surfaces were determined with the BET method (Brunauer et al., 1938). Important soil physical properties (porosity, bulk density, and pore-volume related specific surface,  $S_{por}$ ) are provided in Table 4.1.

**Table 4.1: Soil physical properties of the pure sand and the sand-clay mixtures.**

	Sand-clay mixtures			
	sand	5 % clay	10 % clay	20 % clay
Porosity [%]	39.02	36.98	34.87	34.30
bulk density [g/cm <sup>3</sup> ]	1.62	1.66	1.71	1.71
Calculated $S_{por}$ [ $\mu\text{m}^{-1}$ ]	0.43	3.44	6.55	13.70

#### 4.2.3 Experimental approach

The sand and clay material was mixed in a dry state and then moistened. The measurement column was filled with water to a height of about 2 cm and part of the moistened material was filled into the column. This procedure was repeated in steps of 2 cm until the sample holder was filled. During filling, it was made sure that the added sample material was below the water surface. In addition, air bubbles were removed by carefully drawing them up to the surface using a spoon. This packing procedure was used to achieve a fully saturated initial condition.

After sample preparation was completed, the sample holder was connected to the burette filled with water to the same height as the top of the sample. This resulted in a hydraulic equilibrium after waiting one day. Next, the soil column was also connected to the pressure supply and the pressure was increased in several steps corresponding to a classical Multi-Step Outflow method used to determine soil hydraulic properties (van Dam et al., 1994). Electrical SIP measurements were conducted almost every day. When water outflow approached zero and the SIP measurements of two consecutive days were the same, hydraulic equilibrium was assumed and the next pressure step was applied. The chosen pressure steps differed between the samples due to their different hydraulic properties. The pressure steps were not known in advance but were based on the measured outflow during the previous pressure steps. The

selected pressure steps are provided in Table 4.2 for the four samples. Note that not all spectra for all pressure steps are presented in the subsequent figures for reasons of clarity.

**Table 4.2: Pressure steps for all four samples.**

Samples	Applied pressures [mbar]
Pure sand	10, 40, 50, 52, 55, 60, 65, and 70
5% sand-clay mixture	40, 50, 55, 60, 65, 70, 75, 80, 85, 100, 120, 140, and 160
10% sand-clay mixture	10, 50, 70, 75, 80, 85, 90, 95, 100, 105, 110, 120, 130, 140, 155, 175, 200, 250, 300, 350, 400, 500, and 600
20% sand-clay mixture	10, 30, 40, 50, 80, 85, 100, 130, 140, 170, 200, 250, 300, 350, 425, 500, 550, and 600

#### 4.2.4 Data interpretation of electrical results

The complex electrical resistivity ( $\rho^*(\omega)$ ) can be written as consisting of a real part ( $\rho'$ ) and an imaginary part ( $\rho''$ ) or as resistivity amplitude ( $|\rho|$ ) and a phase angle ( $\varphi$ ) measured between the induced sinusoidal current signal and the measured voltage signal:

$$\rho^*(\omega) = \rho'(\omega) + i\rho''(\omega) = |\rho(\omega)| \cdot e^{i\varphi(\omega)}, \quad (4.3)$$

with  $i = \sqrt{-1}$  and  $\omega = 2\pi f$ . Here, we choose to express  $\rho^*(\omega)$  in terms of amplitude and phase angle, which can be calculated from the real and imaginary part of  $\rho^*(\omega)$  as follows:

$$|\rho(\omega)| = \sqrt{(\rho'(\omega))^2 + \rho''(\omega)^2} \text{ and} \quad (4.4)$$

$$\varphi(\omega) = \arctan\left[\frac{\rho''(\omega)}{\rho'(\omega)}\right] \approx \frac{\rho''(\omega)}{\rho'(\omega)}. \quad (4.5)$$

The approximation in Eq. (4.5) for the phase angle of the complex electrical conductivity is valid for small phase angles.

The  $\rho^*(\omega)$  data are commonly interpreted using phenomenological models, such as the Cole-Cole model (Cole & Cole, 1941). Recently, a new approach called Debye decomposition (Nordsiek & Weller, 2008) has increasingly been used for interpretation of  $\rho^*(\omega)$ . It is adapted from a similar analysis of time domain induced polarization by (Morgan & Lesmes, 1994). This approach regards the resistivity magnitude and phase angle spectra as a superposition of relaxation processes which can be described by  $N$  Debye models:

$$\rho^*(\omega) = \rho_0 \left( 1 - \sum_{k=1}^N m_k \left( 1 - \frac{1}{1 + i\omega\tau_k} \right) \right). \quad (4.6)$$

Using this approach,  $\rho^*(\omega)$  is characterized by the low-frequency resistivity,  $\rho_0$ , the distribution of chargeability,  $m_k$ , and the relaxation time distribution,  $\tau_k$ . We used the modified Debye decomposition procedure of Zisser et al. (2010) in which the relaxation time distribution is determined by normalizing the complex electrical resistivity to  $\rho_0$  and separating the resulting normalized complex resistivity in a real and an imaginary part. Zisser et al. (2010) also introduced a weighting factor ( $w$ ) between the imaginary part and real part

of the normalized resistivity. From numerical tests on synthetic data, the optimal weighting factor was found to be:

$$w = 0.6 \frac{\sum_{l=1}^p \rho'_{norm}(\omega_l)}{\sum_{l=1}^p \rho''_{norm}(\omega_l)}, \quad (4.7)$$

where  $p$  is the number of measured frequencies. The resulting linear equation system was solved using the constraint that no negative chargeability values are allowed. The inversion of the measured spectra into relaxation time distributions was done by using 100 logarithmically spaced relaxation times in the range from  $10^{-5}$  to  $10^5$  s. To remove the electromagnetic coupling effects and the effects of the contact impedance of the non-polarizing electrodes, the high-frequency part of the phase spectra was fitted with a Cole-Cole term and subsequently removed from the electrical spectra as proposed by Pelton et al. (1978). A potential disadvantage of this procedure is that not only the effects of electromagnetic coupling and contact impedances of the potential electrodes are removed, but that polarization of the sample in the kHz range (i.e. associated with small pores or clay particles and Maxwell-Wagner polarization) is also removed.

#### 4.2.5 Data interpretation for hydraulic measurements

Using inverse modeling, the unknown hydraulic parameters governing the processes and fluxes in the system are estimated with help of independent observations of the system. In the inversion process, the model parameters are adjusted to minimize the difference between observed and modeled values. We used HYDRUS-1D by Simunek et al. (2005) to model water flow using the Richards equation:

$$\frac{\partial \theta}{\partial t} = \frac{\partial}{\partial z} \left[ K(h) \frac{\partial}{\partial z} (h + z) \right], \quad (4.8)$$

where  $z$  is the axis in vertical direction,  $h$  is the matric potential,  $\theta$  is the water content, and  $K(h)$  is the unsaturated hydraulic conductivity. The Richards equation can be solved by defining the moisture retention characteristic, the hydraulic conductivity function, and the initial and boundary conditions. To describe the moisture retention characteristic and the hydraulic conductivity function, we used the single porosity Mualem - van Genuchten model (Mualem, 1976; van Genuchten, 1980):

$$S_r = \frac{\theta(h) - \theta_r}{\theta_s - \theta_r} = \left( 1 + |\alpha h|^n \right)^{-m}, \quad (4.9)$$

$$K(h) = K_s \left( \frac{\theta(h) - \theta_r}{\theta_s - \theta_r} \right)^{1/2} \left( 1 - \left( 1 - \left( \frac{\theta(h) - \theta_r}{\theta_s - \theta_r} \right)^{1/m} \right)^m \right)^2, \quad (4.10)$$

where  $K_s$  is the saturated hydraulic conductivity,  $S_r$  is the relative saturation,  $\theta_r$  is residual water content,  $\theta_s$  is the water content at full saturation,  $\alpha$  is the inverse of the air-entry value,  $n$  is a shape parameter related to the pore size distribution, and  $m = 1 - 1/n$ . To model our MSO experiments, the upper boundary condition was defined as a no flow boundary and a time-variable pressure head was applied to the bottom of the sample to simulate outflow (i.e. the applied pressure at the top of the sample was transformed into suction at the bottom and then normalized to the area of the soil column). The initial conditions were set to static equilibrium with a water level at the top of the soil sample. No hysteresis effects were considered.

The model domain of 10.7 cm was discretized in 108 nodes with a denser spacing in the lower part of the model domain. We considered two materials in the simulation: the 10 cm thick sample (sand or sand-clay mixture) and the bottom ceramic plate of 0.7 cm. It was necessary to include the ceramic plate in the simulation because it has a relatively low hydraulic conductivity that affected the outflow of the sample, especially when the sample was near to saturation (also see Breede et al., 2011). The saturated hydraulic conductivity of the ceramic plate was determined independently in a falling-head experiment (Head, 1982) and  $\theta_r$  and  $\theta_s$  were determined by saturating the ceramic plate and weighting it before and after it was dried for 24h at 105°C. Furthermore,  $\alpha$  was set to a very low value of 0.00049 cm<sup>-1</sup> to ensure that the ceramic plate remained saturated throughout the simulation.

We decided to fix  $\theta_s$  of the sample to the measured porosity value during inverse modeling. This is a reasonable assumption given the careful sample preparation that avoided air entrapment. In addition,  $K_s$  was independently determined using a falling-head experiment prior to drainage of the sample and fixed to this value. The objective function used during inverse modeling contained two types of information. First, the difference between measured outflow,  $q^*$ , and simulated outflow,  $q$  (in m) for  $j$  measurements was considered. Second, two independently measured points of the water retention characteristic determined with a pressure plate extractor (for 3 and 15 bar) were included in the objective function. Therefore, the objective function OF to be minimized during the parameter estimation procedure can be written as:

$$OF(b, q, p) = \sum_{j=1}^{n_b} \bar{v}_j [q_j^* - q_j]^2 + 2[\theta_{3bar}^* - \theta_{3bar}]^2 + 2[\theta_{15bar}^* - \theta_{15bar}]^2 \quad (4.11)$$

To minimize the objective function, the Levenberg-Marquardt nonlinear minimization method was used (Marquardt, 1963). The initial parameter estimates that were used to start the optimization are summarized in Table 4.3.

**Table 4.3: Initial parameter estimates of the sample material for the optimization during the modeling with HYDRUS-1D.  $\theta_s$  is the saturated water content,  $\theta_r$  is the residual water content,  $\alpha$  is the inverse of the air-entry-pressure,  $n$  is a shape parameter related to the pore size distribution, and  $K_s$  is the saturated hydraulic conductivity.**

	Sand-clay mixtures			
	sand	5 % clay	10 % clay	20 % clay
$\theta_s$ [m <sup>3</sup> m <sup>-3</sup> ] (fixed value)	0.390	0.370	0.349	0.343
$\theta_r$ [m <sup>3</sup> m <sup>-3</sup> ]	0.045	0.087	0.145	0.137
$\alpha$ [cm <sup>-1</sup> ]	0.022	0.030	0.017	0.015
$n$	19.00	3.00	4.91	2.00
$K_s$ [cm d <sup>-1</sup> ] (fixed value)	720.00	9.12	3.96	0.48

### 4.3 Results and Discussion

The results for the MSO experiments for the pure quartz sand and the three sand-clay mixtures are presented in Figure 4.2.

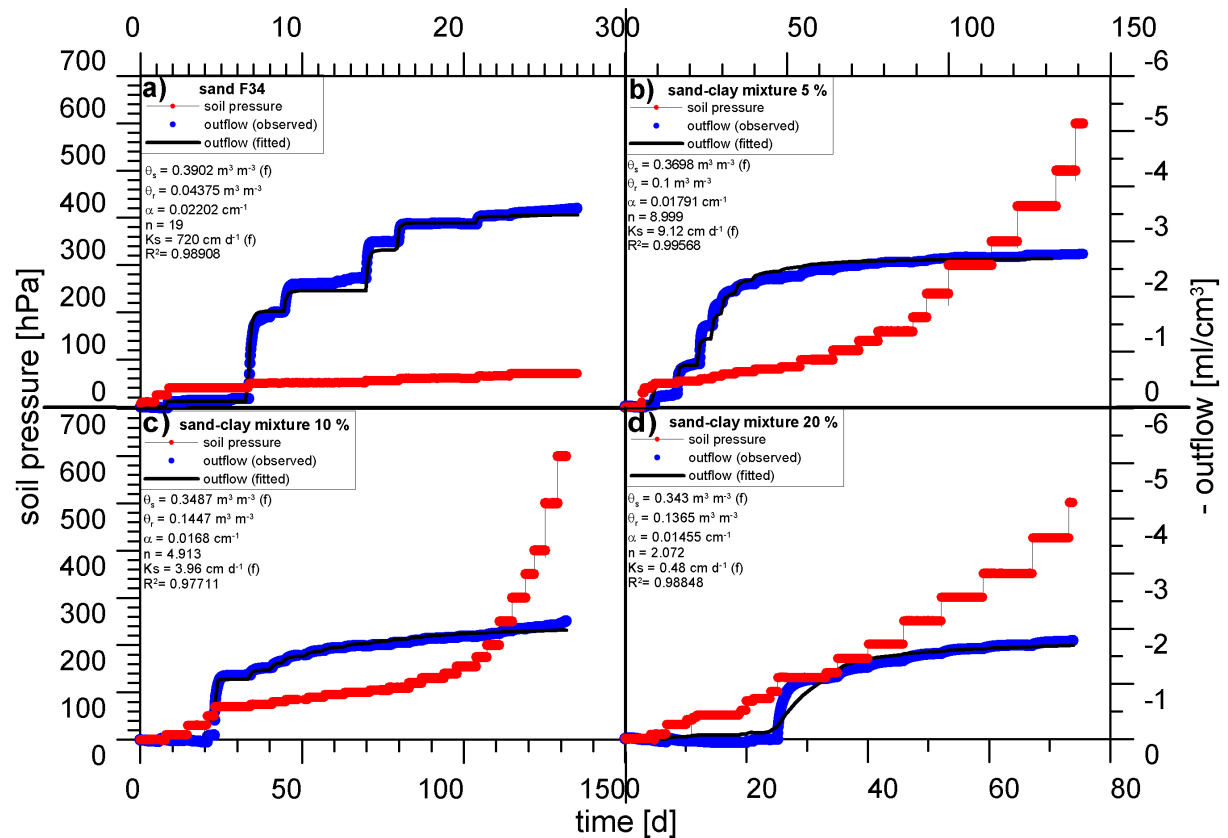


**Figure 4.2:** Outflow experiments for a) pure sand b) 5% sand-clay mixture c) 10% sand-clay mixture, and d) 20% sand-clay mixture.

With increasing clay content, higher pressures are needed to desaturate the sample. In addition to the applied pressure and the observed outflow, the simulated outflow curves based on the best fitting Mualem-Van Genuchten model parameters (Table 4.4) are also presented. In most cases, the simulated outflow matched the observed outflow very well. The simulations for the pure sand showed some deviations from the measured outflow, which was attributed to irregularities in the pressure regulation and the high  $n$  value ( $n = 19$ ) of the fit. However, we were not able to fit the MSO data of the 20% sand-clay mixture properly with the Mualem-Van Genuchten model because it was not possible to describe the early-time MSO data. Thus, we decided to not consider pressure steps below 130 mbar in the inversion. This implies that the hydraulic conductivity is underestimated for pressure steps lower than 130 mbar, i.e. near full saturation.

**Table 4.4: Mualem-van Genuchten parameter obtained by inverse modeling with HYDRUS 1D.  $\theta_s$  – saturated water content,  $\theta_r$  – residual water content,  $\alpha$  - inverse of air entry value,  $n$  – n parameter,  $K_s$  – saturated hydraulic conductivity,  $R^2$  – coefficient of determination.**

	Sand-clay mixtures			
	sand	5 % clay	10 % clay	20 % clay
$\theta_s$ [ $\text{m}^3 \text{m}^{-3}$ ] (fixed value)	0.390	0.370	0.349	0.343
$\theta_r$ [ $\text{m}^3 \text{m}^{-3}$ ]	0.044	0.100	0.145	0.137
$\alpha$ [ $\text{cm}^{-1}$ ]	0.022	0.018	0.017	0.015
$n$	19.00	9.00	4.91	2.07
$K_s$ [ $\text{cm d}^{-1}$ ] (fixed value)	720.00	9.12	3.96	0.48
$R^2$	0.989	0.996	0.977	0.989

Since we waited for approximate hydraulic equilibrium after each pressure step, points of the water retention curves can also be determined directly from the data. These points are shown in Figure 4.3 together with the water retention curves obtained by inverse modeling.

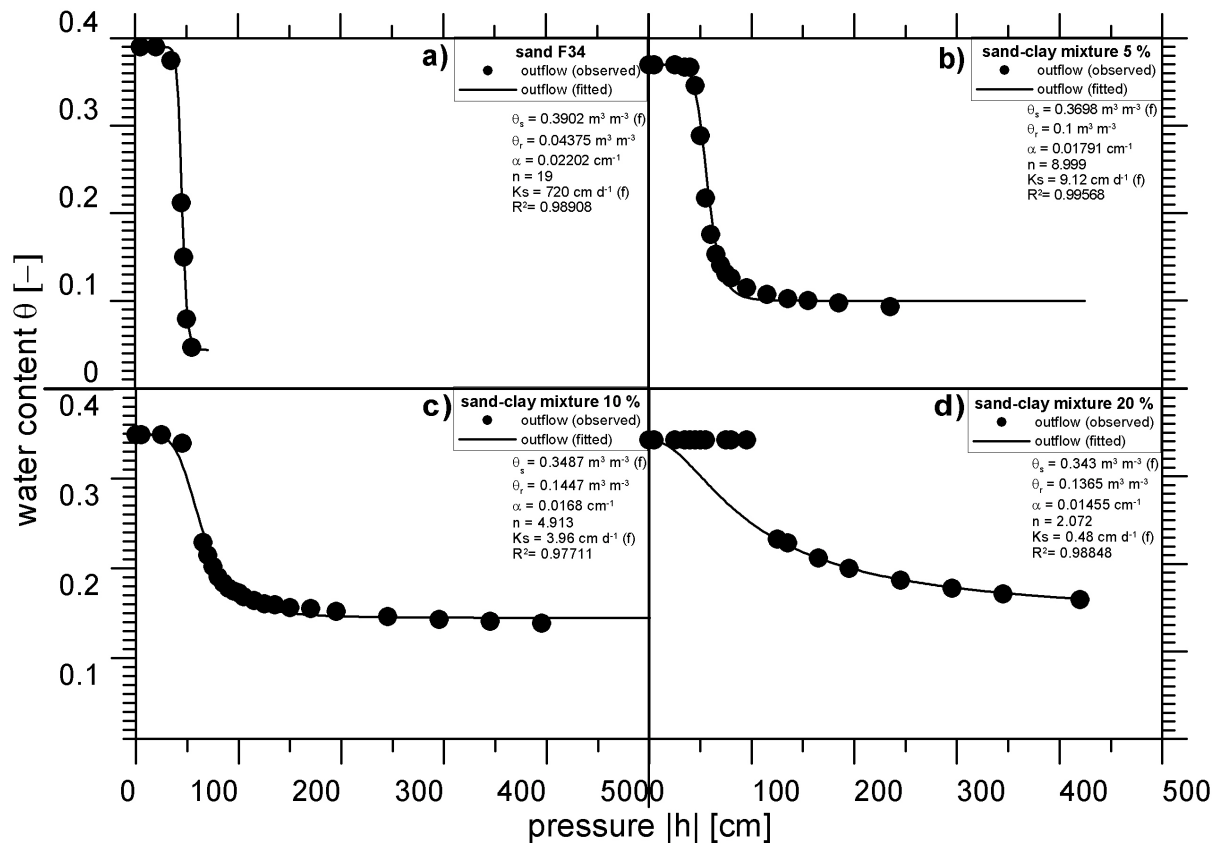


**Figure 4.3: Retention curves for a) pure sand b) 5% sand-clay mixture c) 10% sand-clay mixture, and d) 20% sand-clay mixture.**

There are some deviations in the lower part of the retention curves indicating that the Mualem – van Genuchten model might not be able to describe the outflow data for high pressures. In addition, the high air-entry pressure of the 20% sand-clay mixture in combination with the quick drop in water content for higher pressure could not be reproduced with the Mualem-van Genuchten model.

The hydraulic parameters obtained by inverse modeling (Table 4.4) seem consistent and plausible. The saturated water content was determined from the porosity, which decreased with increasing clay content indicating that the clay partly filled up the pores of the sand matrix. The  $K_s$  of the samples was also determined independently in a falling-head experiment and decreased with increasing clay content as would be expected because increasing clay content lowers the largest pore sizes that control  $K_s$ . The fitted residual water content of the sand is within the expected range with a value of 0.04. With increasing clay content, the fitted residual water content increased, which again is reasonable because more water is expected to be adsorbed to the grains due to the increase in surface area with increasing clay content. The fitted  $\alpha$  (inverse of air-entry pressure) decreased with increasing clay content. This is due to the fact that higher pressures have to be applied to inject air into the much smaller pores of the sand-clay mixtures. Finally, the fitted n-parameter decreased with increasing clay content indicating that the width of the pore size distribution increased with increasing clay content.

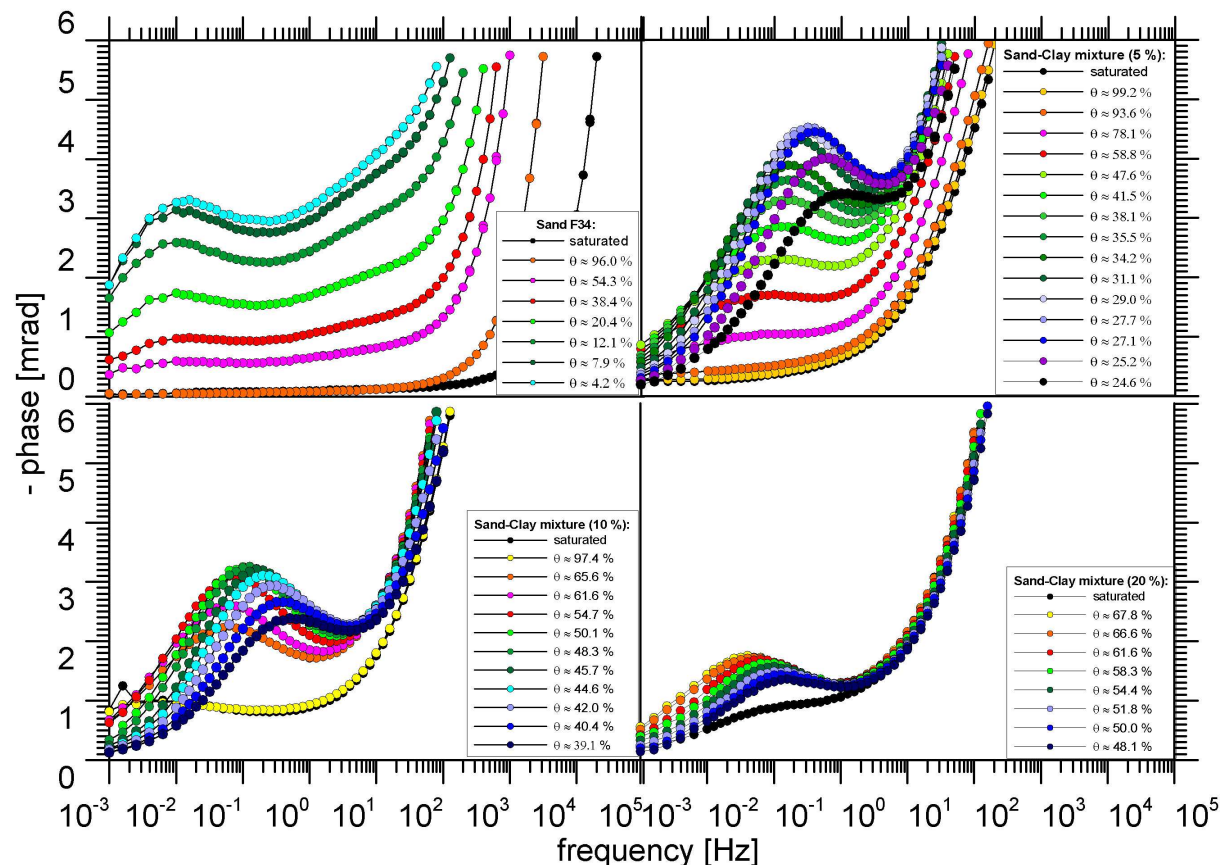


**Figure 4.4: Electrical phase spectra for a) pure sand b) 5% sand-clay mixture c) 10% sand-clay mixture, and d) 20% sand-clay mixture.**

The electrical phase spectra of all samples in dependence of the water saturation are shown in Figure 4.4. The variation of the real and imaginary part of the electrical conductivity, the total

chargeability, and the relaxation time as a function of water saturation were discussed in detail in an earlier paper (Breede et al., 2012) and will not be repeated here. In the same paper, we fitted the real part of the electrical conductivity using the model of Jougnot et al. (2010) based on Revil et al. (2007) for variably saturated porous media:

$$\sigma' = \frac{1}{F} \sigma_w S_w^e + \left( \frac{F-1}{F} \right) \sigma_s', \quad (4.12)$$

where  $F$  is the formation factor,  $\sigma_w$  is the conductivity of the pore fluid,  $S_w$  is the water saturation,  $e$  is the saturation exponent, and  $\sigma_s'$  is the real part of the surface conductivity. The fitted petrophysical parameters for all four samples are summarized in Table 4.5.

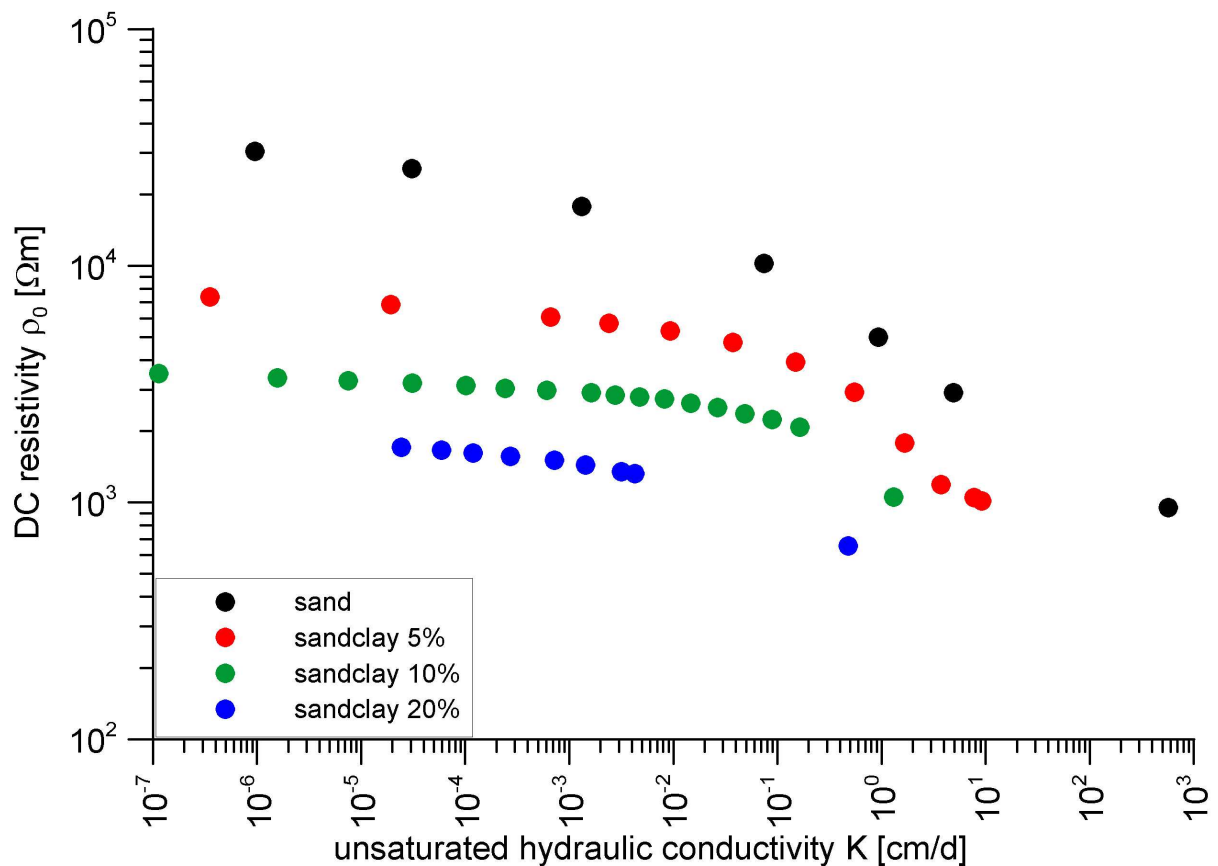
**Table 4.5: Petrophysical parameters fitted using the model of Jougnot et al. (2010).**

	Sand-clay mixtures			
	sand	5% clay	10% clay	20% clay
Formation factor, $F$ [-]	3.69	4.13	4.40	3.70
Saturation exponent, $e$ [-]	1.77	1.86	1.91	3.70
Surface conductivity, $\sigma_s'$ [ $\text{Sm}^{-1}$ ]	0.0005	0.0006	0.0021	0.0088

The main features of the electrical spectra shown in Figure 4.4 can be summarized as follows. The pure sand shows a constant phase angle for full saturation (see Figure 4.4a) up to 100 Hz. With decreasing water saturation, the phase increased and a slight maximum occurred at a frequency of about 10 mHz. Using equation (4.1), this frequency can be related to a grain size of about 0.36 mm, which corresponds reasonably with the mean sand grain size. A change in the slope of the phase spectra at about 10 Hz indicated another relaxation frequency. This frequency corresponds to a grain size of about 0.011 mm. However, this grain size fraction was not present in the well-sorted sand material. Therefore, this polarization is attributed to second-order heterogeneities corresponding to the roughness of the sand grains, as previously observed for glass beads by Leroy et al. (2008). A maximum phase of about 3.3 mrad was obtained for a water saturation of 4%.

The behavior of the phase spectra in dependence of the water saturation is much more complex for the 5% sand-clay mixture (Figure 4.4b). The phase of the fully saturated sample again showed a constant phase angle, although the phase increase at higher frequencies occurred at lower frequencies than for the pure sand. We attribute this early increase to the clay minerals, which are known to affect the phase at frequencies around 1 kHz. With decreasing water saturation, the phase increased and a maximum appeared at about 0.1 Hz for a water saturation of about 59%. With further decrease in saturation, the phase increased further and the peak in the phase shifted to higher frequencies. At a water saturation of about 28%, the maximum phase of 4.5 mrad was reached. The spectra belonging to this water saturation occurred at a pressure of about 120 mbar. For saturations below 28%, the phase decreased with decreasing water saturation, although the peak continued to shift to higher frequencies, i.e. lower relaxation times. This shift to lower relaxation time was also observed by Binley et al. (2005).

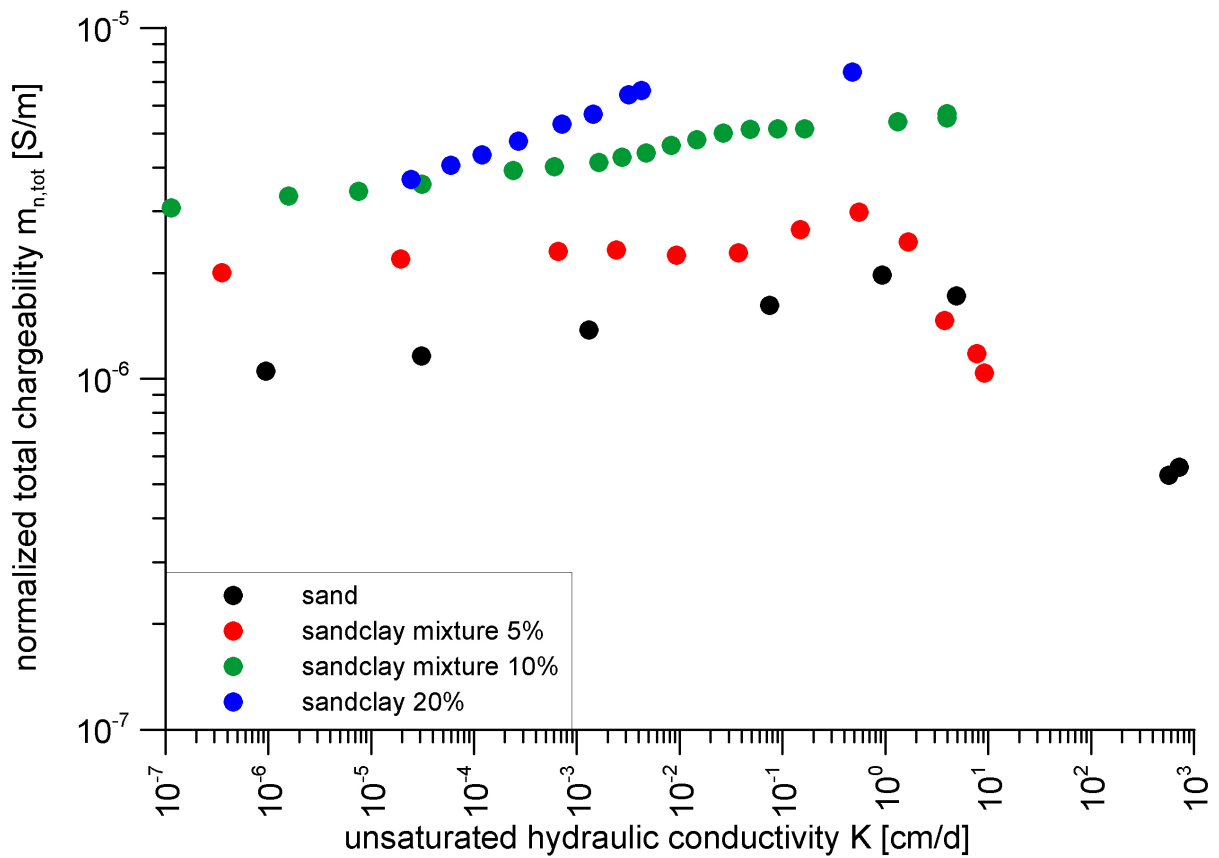
The behavior for the 10% sand-clay mixture is similar to the 5% sand-clay mixture (see Figure 4.4c), although the water saturation where the peak in the phase was highest occurred at a saturation of  $\sim 47\%$  for a pressure of 110 mbar. The associated maximum phase was only 3.3 mrad. At first sight, the behavior of the phase spectra for the 20% sand-clay mixture (Figure 4.4d) seemed different. For example, a slightly increasing phase angle instead of a constant phase angle was obtained at full saturation although the observed increase in phase angle was less than 1 mrad. Directly after the pressure step of 130 mbar, a considerable amount of water drained out of the sample and the phase increased abruptly and showed a peak at a frequency of about 0.03 Hz and a maximum phase value of 1.75 mrad. With further decreasing water saturation, the phase decreased and again the phase maximum shifted to higher frequencies. This initial increase and subsequent decrease of the phase maximum is consistent with the other two sand-clay mixtures. In all three sand-clay mixtures, the change from an increasing to a decreasing phase maximum with decreasing saturation occurred in a relatively small pressure range between 110 – 130 mbar.



**Figure 4.5: DC resistivity  $\rho_0$  which was achieved by the Debye Decomposition versus the unsaturated hydraulic conductivity.**

In the remainder of this paper, we focus on the relationship between electrical parameters and the unsaturated hydraulic conductivity. Figure 4.5 shows the DC resistivity  $\rho_0$  obtained from the Debye decomposition as a function of the unsaturated hydraulic conductivity. Obviously,  $\rho_0$  increased with decreasing  $K$  due to the decreasing water saturation. However, no clear and consistent relationship between  $\rho_0$  and  $K$  was observed.  $\rho_0$  at full saturation was the same for all materials except the 20% sand-clay mixture, while  $K_s$  was considerably different. The similar values of  $\rho_0$  for different amounts of clay content imply that it is not possible to determine  $K$  or  $K_s$  from DC resistivity alone. In addition,  $\rho_0$  increased with decreasing clay content at partial saturation, i.e. lower hydraulic conductivity. The increase in  $\rho_0$  with decreasing saturation also varied considerably between the samples. We compared our

relationships between the DC resistivity and the unsaturated hydraulic conductivity with other findings in the literature. For example, Doussan & Ruy (2009) proposed three different approaches to determine the unsaturated hydraulic conductivity from electrical measurements. Similar to our findings, they were not able to estimate the unsaturated hydraulic conductivity from the DC resistivity alone, but added additional information like the surface conductivity and the saturated hydraulic conductivity. We applied the simplified approach of Doussan & Ruy (2009) that relies on a minimum amount of additional information to our data. However, the hydraulic conductivity estimates from this approach did not agree with the unsaturated hydraulic conductivity estimates from the HYDRUS-1D modeling. Other approaches to determine the saturated hydraulic conductivity like the Kozeny-Carman equation or the PARIS equation (Pape et al., 1987) also require additional information, such as the specific surface or the imaginary component of the complex electrical resistivity. However, these approaches could also not be successfully applied to our samples.



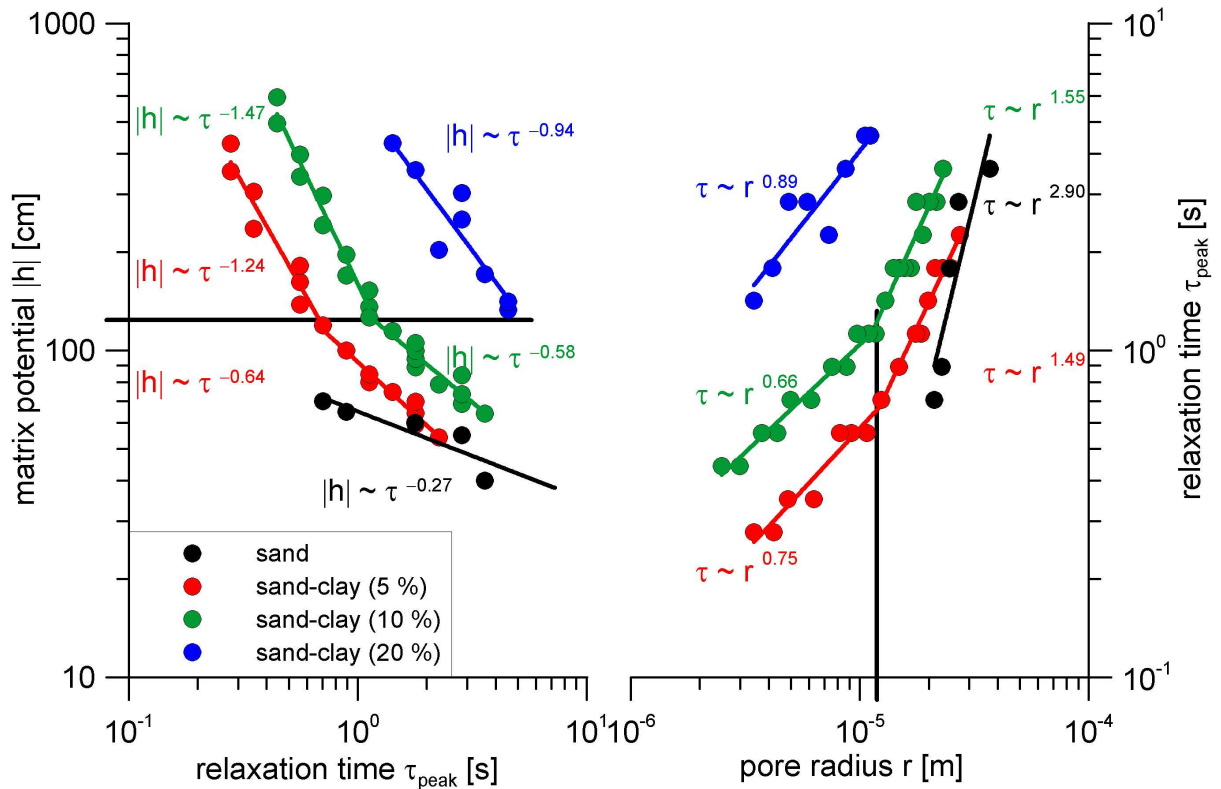
**Figure 4.6: Normalized total chargeability achieved by the Debye Decomposition versus the unsaturated hydraulic conductivity.**

Figure 4.6 shows the normalized total chargeability  $m_{n,tot}$  as a function of the unsaturated hydraulic conductivity. The normalized total chargeability is the total chargeability of the sample normalized by the DC resistivity and reflects the polarization of the whole sample:

$$m_{n,tot} = \frac{\sum_{k=1}^n m_k}{\rho_0} \quad (4.13)$$

We observed that the behavior of the relationship between  $m_{n,tot}$  and  $K$  is very similar to the relationship between  $m_{n,tot}$  and the water saturation  $S_w$  (not shown, see Breede et al., 2012). The normalized total chargeability of the sand and the 5% sand-clay mixture first increased and then decreased with decreasing  $K$  and  $S_w$ . The 10% sand-clay mixture first showed a decrease followed by a slight increase and then  $m_{n,tot}$  decreased again with decreasing  $K$ . A

maximum in  $m_{n,tot}$  was not observed for the 20% sand-clay mixture. It can also be seen in Figure 4.6 that the chargeability increased with increasing clay content. We are not aware of other studies correlating  $m_{n,tot}$  with the unsaturated hydraulic conductivity. However, since  $m_{n,tot}$  is closely related to the imaginary part of the electrical resistivity (e.g., Weller et al., 2010), which was previously related to hydraulic conductivity using empirical models (e.g. PARIS equation), relationships might have been observed. However, given the complex behaviour of  $m_{n,tot}$  in Figure 4.6, it has to be concluded that it is not possible to deduce the unsaturated hydraulic conductivity from this parameter.



**Figure 4.7:** (a) Matrix potential versus peak relaxation time. (b) Relaxation time versus pore radius.

Figure 4.7a shows the matrix potential  $|h|$  versus the peak relaxation time for all samples. Please note that some electrical measurements near saturation are not displayed because the peak relaxation time could not be determined accurately due to the small phase values and the nearly constant phase angle behavior. Figure 4.7a shows that the matrix potential is related to  $\tau_{peak}$  as follows:

$$\log(|h|) \sim b_1 * \log(\tau) \quad (4.14)$$

However, we obtained two different relationships, one for  $|h| \leq 120$  cm with  $b_1$  higher than -0.7 and one for  $|h| \geq 120$  cm with  $b_1$  lower than -0.9. For sand,  $b_1$  was determined only for  $|h| \leq 120$  cm because the highest applied pressure was 70 mbar. For the 20% sand-clay mixture,  $b_1$  was determined only for  $|h| \geq 120$  cm. Assuming that soil can be represented as a bundle of capillary tubes as a first (rough) approximation, the matrix potential can be converted to an equivalent pore radius using the following equation:

$$r = \frac{2\gamma \cos \beta}{d \cdot g \cdot |h|} \quad (4.15)$$

where  $\gamma$  is the liquid-air surface tension,  $\beta$  is the contact angle,  $g$  is the gravitational acceleration,  $r$  is the equivalent radius of a tube, and  $d$  is the density of liquid. Figure 4.7b

shows the relationship between  $\tau_{peak}$  and this equivalent pore radius. The observed power-law relationship can be described by:

$$\log(\tau_{peak}) \sim b_2 \cdot \log(r). \quad (4.16)$$

The observed change in slope of the power-law relationships now occur at an equivalent radius of 12.5  $\mu\text{m}$ . We found an approximately quadratic dependence between the peak relaxation time and equivalent pore radius for big pores  $\geq 12.5 \mu\text{m}$ . We assume that this quadratic dependence was related to diffusion processes in big pores, as is consistent with current modeling paradigms for SIP. We found a nearly linear dependence between  $\tau_{peak}$  and  $r$  for pores  $< 12.5 \mu\text{m}$ . This low value of the power law exponent might suggest that different relaxation processes dominate for small pores. Although there is some consistency in the slope of the power-law relationships, the strong difference in offset between the four samples illustrated in Figure 4.7 also indicates that  $\tau_{peak}$  is not solely dependent on the pore radius and that other factors also need to be considered (i.e. clay content, pore size distribution).

Although a quadratic dependence between characteristic length scale and relaxation time is the basis of both the granular and the pore model for relaxation processes in porous media, other dependencies have also been proposed. For example, a linear dependence for simple geometries was already proposed by O'Konski (1960). Chelidze & Gueguen (1999) hypothesized that the relaxation time is linear when the particles are large and quadratic when they are small because diffusion as the cause of the quadratic dependence must become inefficient at large distances. However, this observation does not apply to our findings since we observed a quadratic dependence for large pores. The range of exponents found in experimental data is even wider. An exponent close to 1 was found by Klein & Sill (1982) and Binley et al. (2005). An exponent of 2 was found in several studies (Revil & Florsch, 2010 and Titov et al., 2002). Kemna et al. (2005) even found an exponent between 2.59 and 5.75 dependent on the electrical conductivity of the pore fluid. Kruschwitz et al. (2010) summarized the findings of different authors and found an exponent of 2.97 for large pore sizes, while they could not find any correlation for small pore sizes. Wong (1979) found an exponent of one for small grain sizes and an exponent of two for larger grain sizes which is in agreement with our findings. The results presented here clearly indicate complex relaxation processes that are not consistent with current IP models.

The observed power law relationship between peak relaxation time and matric potential directly implies a power law relationship between unsaturated hydraulic conductivity and peak relaxation time. This can be illustrated by the following simplification of the Mualem-van Genuchten model

$$\Theta = (\alpha h)^{-m} \quad (4.17)$$

for values of  $h$  considerably larger than the air entry pressure. Following the Mualem theory with  $m = 1-1/n$ , it follows that (van Genuchten, 1980):

$$K(h) = (\alpha h)^{-2 - \frac{5(n-1)}{2}} \quad (4.18)$$

After some mathematical manipulation, the following expression that relates  $\log(K)$  to  $\log(h)$  can be derived:

$$\log K(h) = (-2 - 2.5(n-1))\log \alpha + (-2 - 2.5(n-1))\log h. \quad (4.19)$$

Substitution of eq. (4.14) into this equation results in:

$$\log K(h) \sim b_1 (-2.5(n-1) - 2) \cdot \log(\tau_{peak}), \quad (4.20)$$

which shows that the power law relationship between peak relaxation time and unsaturated hydraulic conductivity has a slope that depends on  $b_1$  and the  $n$  parameter of the Mualem-van Genuchten model, which is a measure of the width of the pore size distribution.

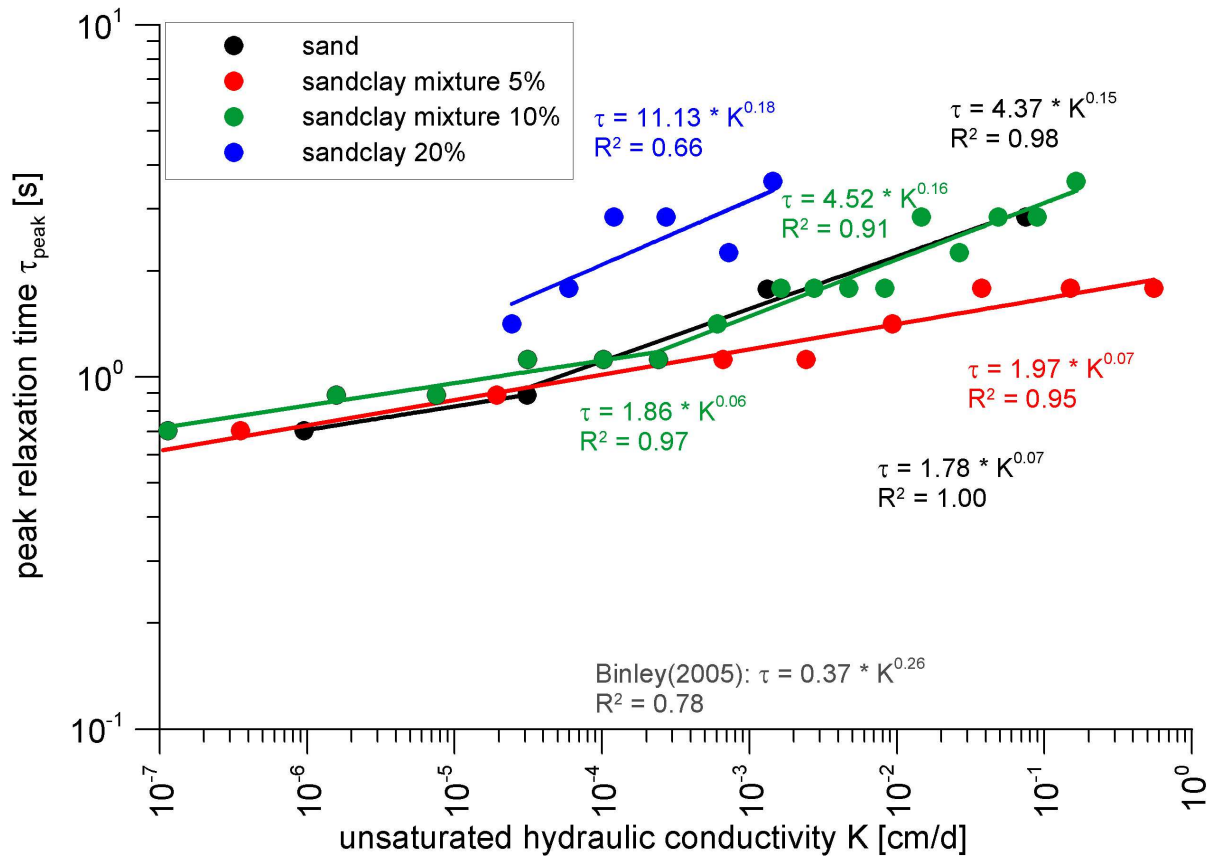


**Figure 4.8: Peak relaxation time versus the unsaturated hydraulic conductivity.**

Figure 4.8 shows the peak relaxation time in dependence of the unsaturated hydraulic conductivity. With decreasing  $K$ , the peak relaxation time decreased. The power law relationship between  $\tau_{peak}$  and  $K$  provided in Eq. (4.20) can be further simplified to:

$$\log(\tau_{peak}) \sim b_3 \cdot \log(K). \quad (4.21)$$

Since the values for  $b_1$  were different for different pressure ranges, a change in slope is observed in Figure 8 for the 5% and 10% sand-clay mixtures. In addition, the fitted value of  $n$  decreased with increasing clay content (Table 4.4), which explains the increase of  $b_3$  (see Table 4.6) with exception of the pure sand.

**Table 4.6: Coefficients  $b_3$  for  $h \leq 120$  cm ( $b_{3,a}$ ) and  $h \geq 120$  cm ( $b_{3,b}$ ).**

Samples	$b_{3,a}$	$b_{3,b}$
Sand	0.15	0.07
5 % sand-clay	0.07	0.03
10 % sandclay	0.16	0.06
20 % sand-clay	0.18	—

This indicates that the relationship between relaxation time and hydraulic conductivity depends on the width of the pore size distribution. Kemna (2000) suggested a linear dependence between relaxation time and unsaturated hydraulic conductivity based on the theoretical proportionality of both parameters on the square of an effective length scale.

Kemna et al. (2005) found a power law relationship with an exponent of 1.78 for five pure sands of varying grain size. However, Binley et al. (2005) found a power law relationship between the relaxation time and the unsaturated hydraulic conductivity with a power-law exponent of 0.26 for 28 sandstone cores from three lithologic formations. This finding is close to our results with an exponent of about 0.17 for matric potentials smaller than 120 cm.

#### **4.4 Conclusions**

In this work, we investigated the relationship between SIP parameters like DC resistivity, normalized total chargeability, and peak relaxation time and the unsaturated hydraulic conductivity for a pure sand and three different sand-clay mixtures. We found that the DC electrical resistivity increased with decreasing unsaturated hydraulic conductivity due to the decreasing water saturation. Surprisingly, the resistivity was the same for the sand and the 5%, and 10% sand-clay mixtures at full saturation although the saturated hydraulic conductivity was different. This leads to the conclusion that no useful relationships between DC electrical resistivity and unsaturated hydraulic conductivity could be found for our data.

The relationship between the normalized total chargeability and the unsaturated hydraulic conductivity was similar to the relationship between normalized total chargeability and water saturation. As expected, the chargeability increased with increasing clay content. However, no consistent relationships between normalized total chargeability and unsaturated hydraulic conductivity could be identified.

We found that the peak relaxation time is proportional to the matric potential and thus to the pore size. However, the exponent of the observed power-law relationship was different for matric potentials smaller than 120 cm and matric potentials larger than this critical value. This exponent was close to 1 for absolute matric potentials larger than 120 cm and varied near 2 for absolute matric potentials smaller than 120 cm. Assuming a simplified capillary tube model, an absolute matric potential of 120 cm corresponds to a pore radius of 12.5  $\mu\text{m}$ . We attribute the quadratic dependence to diffusion processes in big pores, as is typically assumed in current SIP modeling approaches. The observed low exponent for small pores was tentatively attributed to a hitherto unknown relaxation process that warrants more investigation.

The observed relationship between matric potential and peak relaxation time directly implies a power-law relationship between the peak relaxation time and the unsaturated hydraulic conductivity that depends on the  $n$  parameter of the Mualem – van Genuchten model. Thus, we conclude that it might be possible to estimate the unsaturated hydraulic conductivity from SIP measurements using the peak relaxation time. However, additional information like the pore size distribution seems to be necessary.



## 5 Conclusions and Outlook

### 5.1 Final Conclusions

Groundwater is an important resource for humanity because it is used for instance as drinking water and for agricultural usage. However, it is endangered by contaminants and overuse. Soils act as filter, buffer, and storage for groundwater and thus flow and transport processes in soils are of importance. Geophysical methods provide information about the heterogeneity and soil structure, texture, and composition and are often used for hydrological applications. Especially electrical methods like SIP have recently been investigated for the determination of hydraulic properties of saturated and unsaturated porous media. The overall aim of this thesis was to establish an approach for the determination of unsaturated hydraulic conductivity from SIP measurements. This involved three specific aims: (1) to develop a new joint measurement setup for hydraulic and electrical measurements (2) to investigate the dependence of the SIP response on water content, (3) to investigate the dependence of SIP on unsaturated hydraulic conductivity and properties.

The newly designed measurement setup for simultaneous measurements of hydraulic properties and complex electrical resistivity showed accurate and reproducible results for hydraulic and electrical measurements on low polarizable porous media like pure quartz sand. The high measurement accuracy was achieved by using appropriate dimensions for the newly constructed measurement cell, a high-accuracy electrical impedance spectrometer, and newly designed non-polarizable ceramic electrodes. Two different measurement cells were constructed and tested: one for non-shrinking soil like sand with very high accuracy of electric measurements and another one for mildly-shrinking soils like sand-clay mixtures. The accuracy of the electrical measurements with the measurement cell for shrinking soils was not as good as for the other measurement cell, but the adjustable upper part of the measurement cell allowed to expand the pressure range for electrical measurements on shrinking soils. Test measurements showed that the ceramic plates have no influence on the electric measurements but have to be taken into account for the modeling of the hydraulic results with HYDRUS-1D. The newly designed non-polarizable ceramic electrodes were compared to stainless steel potential electrodes. The electromagnetic coupling effects for the stainless steel electrodes were at higher frequencies than for the ceramic electrodes for full saturation. However, the ceramic electrodes showed better results for partial saturation.

Using the joint measurement setup and measurement columns developed in the first part of the thesis, combined electrical and hydraulic measurements were conducted on four different samples: a pure quartz sand and three sand-clay mixtures with 5%, 10%, and 20% clay content. These samples were investigated in dependence of the water content. The SIP results of these four mixtures were interpreted using a Debye decomposition approach. The resulting Debye parameter like DC electrical resistivity, normalized total chargeability and peak relaxation time were investigated in dependence of the water saturation. The real part of the electrical conductivity or DC electrical resistivity was the same at full saturation for all samples except the 20% sand-clay mixture. The normalized total chargeability of the fully saturated samples increased with increasing clay-content due to the larger specific surface area of the clay minerals implying that it might be possible to estimate the clay content from this parameter. A conceptual model combining two individual models for sand and clay fraction was proposed to explain the behavior of the imaginary part of the complex electrical conductivity for 10 mHz and 1 kHz and the behavior of the normalized total chargeability. The model for the sand fraction is based on the short-narrow pore model of Titov et al. (2002), which also predicts that the chargeability is first increasing and then decreasing with

decreasing water saturation. The model for the clay fraction was based on the observed continuous decrease of the imaginary part of the electrical conductivity at 1 kHz, which was explained by rearrangement of the clay particles in the pore volume due to the decreasing amount of water in the pore space. The strong decrease of the peak relaxation time with decreasing water saturation for all sand-clay mixtures can be intuitively explained by the decrease of the size of the hydraulically active pores during the desaturation process. All SIP parameters correlated strongly with water. This implies that water content has to be taken into account for the determination of unsaturated hydraulic properties in the vadose zone from SIP measurements and the distribution of the unsaturated hydraulic conductivity from EIT measurements. In addition, the dependence of the relaxation time on water content cannot be explained by existing grain size models. Thus, more research is necessary to better understand the polarization processes of porous media.

In the fourth chapter of the thesis, we investigated the dependence of the Debye parameters on the unsaturated hydraulic conductivity. The same DC electrical resistivity was measured for the sand and two of three sand-clay mixtures, although they possessed widely different saturated hydraulic conductivities. Thus, additional information in form of clay content or pore size distribution has to be accounted for to determine the saturated or even unsaturated hydraulic conductivity from DC electrical resistivity. No consistent relationships could be found between normalized total chargeability and unsaturated hydraulic conductivity. However, we did find a power-law relationship between the peak relaxation time and the matric potential. This seems to suggest that the peak relaxation time is dependent on the pore size distribution and not the grain size distribution. However, the slope of these curves was different whether the matric potential is above or below a critical matric potential of -120 cm. For matric potentials above this value, we obtained a quadratic dependence, which is consistent with theories that attempt to relate SIP to diffusion processes around a grain or within pores. For matric potentials smaller than -120 cm, we observed a linear relationship indicating a hitherto unknown relaxation process.

As a direct consequence of the relation between the peak relaxation time and the matric potential, we also found power-law relationships between the peak relaxation time and the unsaturated hydraulic conductivity. Using an approximation of the Mualem-van Genuchten model, we derived an empirical relationship between the peak relaxation time and the unsaturated hydraulic conductivity. This empirical relationship is dependent on the  $n$ -parameter of the Mualem-van Genuchten model that reflects the width of the pore size distribution. Thus, we conclude that it might be possible to estimate the unsaturated hydraulic conductivity from SIP measurements using the peak relaxation time. However, additional information like the pore size distribution seems to be necessary.

## **5.2 Outlook**

### **5.2.1 Further laboratory studies using SIP**

We found power-law relationships with different exponents between the relaxation time and the matric potential, respectively between relaxation time and unsaturated hydraulic conductivity for matric potentials above and below -120 cm. Thus, the sample base should be extended by (1) using sands with different average grain sizes and (2) using sand-clay mixtures with different clay types. Thus, it can be investigated if this critical matric potential is related to the average sand grain size or the clay type.

In addition, further experiments on artificial samples and sieved soils are required to further investigate this dependency for a wide range of pore size distributions. Artificial samples have the advantage that they are easier to understand because its composition and grain size distribution can easily be determined. In addition, measurements on natural soils are usually containing additional material like humic substances which can cause additional polarization processes that are not easily understood and would complicate the interpretation of the SIP response. However, it is possible that the observed results are specific to the artificially mixed sand-clay samples and that they are caused by reorientation of the clay particles in the pore space. This would probably not be the case for natural soil samples. Thus, additional SIP experiments on natural soils in the laboratory would be a next step to investigate the power-law relationship between relaxation time and matric potential, respectively between relaxation time and unsaturated hydraulic conductivity. If the experiments are done in the laboratory, influences on the SIP response like temperature and water content can be better controlled. In addition, the data base should be extended by specifically using samples with a wider pore-size distribution and a wider range of saturated hydraulic conductivities. Thus, it could be investigated if the above mentioned power-law relationships for matric potentials below and above -120 cm are also valid for a wider range of saturated hydraulic conductivities.

SIP experiments on artificial mixtures and natural soils combined with NMR measurements would be sensible to further investigate the probable relationship between NMR and SIP relaxation times. Both parameters are probably a measure of the pore size distribution. Thus, a confirmation of the pore size distribution achieved from SIP with NMR might show if the SIP relaxation time is really a measure of the pore size distribution.

### **5.2.2 Laboratory EIT experiments**

EIT experiments on natural soil samples in lysimeters could be an important step towards field experiments. Due to the larger scale of such lysimeter experiments, structural and textural heterogeneity of the soil could be better investigated. The proposed EIT experiments could be combined with infiltration experiments and a color tracer. Thus not only the heterogeneity but also the heterogeneous water flow through the soil column could be investigated. Using steady-state flow experiments, such a set-up could also be used to directly establish a relationship between the peak relaxation time and the unsaturated hydraulic conductivity.

### **5.2.3 Step to the field**

The accuracy of field and borehole SIP and EIT devices has to be improved to allow accurate SIP measurements on natural soils in the field. If this can be achieved, it would be possible to confirm the findings of this thesis on the field-scale. Field EIT experiments on well

investigated field sites should be a first step. Thus the observed EIT results could be compared with the already existing knowledge about the subsurface. In addition, surface EIT measurements could be combined with SIP borehole measurements or other additional surface and borehole geophysical methods like GPR. Thus a better spatial resolution and characterization of the subsurface could be achieved.

#### **5.2.4 Simulations**

Our measurement results cannot be explained or simulated by existing models. Thus, a new model is needed taking account for the decreasing peak relaxation time with decreasing water saturation and decreasing unsaturated hydraulic conductivity. For the latter one, the model has also to account for the two different relaxation processes that were found for our experiments: a quadratic relationship between peak relaxation time and matric potentials for matric potentials above -120 cm and a linear relationship for matric potentials below -120 cm. Thus, the dependence on the matric potential has also to be considered for this model. Another problem for our SIP measurement results was the high-frequency response of the clay minerals at about 1 kHz. Signals at such frequencies are often ignored or fitted by a Cole-Cole term for instance to subtract it from the phase spectrum in order to delete the electromagnetic coupling effects. Either approach results in ignoring signals coming from clay minerals that often occur at such high frequencies. Thus a model is needed to fit the electromagnetic coupling effects alone without high-frequency effects coming from the sample.

## References

### 6 Literaturverzeichnis

- Bauer, J., Weihermüller, L., Huisman, J., Herbst, M., Graf, A., Sequaris, J., et al. (2012). Inverse determination of heterotrophic soil respiration response to temperature and water content under field conditions. *Biogeochemistry*, 108, p. 119-134.
- Binley, A., Cassiani, G., & Deiana, R. (2010). Hydrogeophysics opportunities and challenges. *Bollettino di Geofisica Teorica ed Applicata*, 51, p. 267-284.
- Binley, A., Slater, L. D., Fukes, M., & Cassiani, G. (2005). Relationship between spectral induced polarization and hydraulic properties of saturated and unsaturated sandstone. *Water Resources Research*, 41, W12147.
- Börner, F. D., Schopper, J. R., & Weller, A. (1996). Evaluation of transport and storage properties in the soil and groundwater zone from induced polarization measurements. *Geophysical Prospecting*, 44, p. 583-601.
- Börner, F., & Schön, J. (1991). A relation between the quadrature component of electrical conductivity and the specific surface area of sedimentary rocks. *The Log Analyst*, 32, p. 612-613.
- Breede, K., Kemna, A., Esser, O., Zimmermann, E., Vereecken, H., & Huisman, J. (2011). Joint measurement setup for determining spectral induced polarization and soil hydraulic properties. *Vadose Zone Journal*, 10, p. 716-726.
- Breede, K., Kemna, A., Esser, O., Zimmermann, E., Vereecken, H., & Huisman, J. (2012). Spectral induced polarization measurements on variably saturated sand-clay mixtures. *Near Surface Geophysics*. In review process.
- Brovelli, A., Cassiani, G., Dalla, E., Bergamini, F., Pitea, D., & Binley, A. (2005). Electrical properties of partially saturated sandstones: Novel computational approach with hydrogeophysical applications. *Water Resour. Res.*, 41.
- Brunauer, S., Emmet, P., & Teller, E. (1938). Adsorption of gases in multimolecular layers. *Journal of the American Chemical Society*, 60(2), p. 309-319.
- Butler, J. J. (1998). *The Design, Performance, and Analysis of Slug Tests*. Lewis Pub.
- Butler, J. J., McElwee, C. D., & Liu, W. (1996). Improving the quality of parameter estimates obtained from slug tests. *Ground Water*, 34, p. 480-490.
- Carman, P. C. (1997). Fluid flow through granular beds. *Chemical engineering research & design*, 75, p. S32-S48.
- Cassiani, G., Kemna, A., Villa, A., & Zimmermann, E. (2009). Spectral induced polarization for the characterization of free phase hydrocarbon contamination of sediments with low clay content. *Near Surface Geophysics*, 7, p. 547-562.
- Chelidze, T., & Gueguen, Y. (1999). Electrical spectroscopy of porous rocks: a review - I Theoretical models. *Geophysical Journal International*, 137, p. 1-15.
- Chen, J., Kemna, A., & Hubbard, S. (2008). A comparison between Gauss-Newton and Markov-chain Monte Carlo - based methods for inverting spectral induced-polarization data for Cole-Cole parameters. *Geophysics*, 73, p. F247-259.
- Chen, Y., & Or, D. (2006). Geometrical factors and interfacial processes affecting complex dielectric permittivity of partially saturated porous media. *Water Resour. Res.*, 42.
- Cole, K., & Cole, R. (1941). Dispersion and absorption in dielectrics, vol. I. Alternating current field. *Journal of Chemical Physics*, 9, p. 341-351.
- Cosenza, P., Ghorbani, A., Florsch, N., & Revil, A. (2007). Effects of drying on the low-frequency electrical properties of Tournemire argillites. *Pure Appl. Geophys.*, 164, p. 2043-2066.
- Dahlin, T., Leroux, V., & Nissen, J. (2002). Measuring techniques in induced polarization imaging. *J. Appl. Geophys.*, 50, p. 279-298.

- Dane, J. H., & Topp, G. C. (2002). *Methods of soil analysis Part 4 Physical methods*. Madison, WI, USA: Soil Science Society of America, Inc.
- de Lima, O. A., & Niwas, S. (2000). Estimation of hydraulic parameters of shaly sandstone aquifers from geoelectrical measurements. *J. Hydrology*, 235, p. 12-26.
- Dias, R., Fernandes, C., Teixeira, J., Mota, M., & Yelshin, A. (2008). Permeability analysis in bisized porous media: Wall effect between particles of different size. *Journal of Hydrology*, 349, p. 470-474.
- Doussan, C., & Ruy, S. (2009). Prediction of unsaturated soil hydraulic conductivity with electrical conductivity. *Water Resources Research*, 45.
- Dukhin, S., & Shilov, V. (1974). *Dielectric phenomena and the double layer in disperse systems and polyelectrolytes*. New York: John Wiley & Sons.
- Ghorbani, A., Cosenza, P., Ruy, S., Doussan, C., & Florsch, N. (2008). Non invasive monitoring of water infiltration in a silty clay loam soil using Spectral Induced Polarization. *Water Resources Research*, 44, W08402.
- Hazen, A. (1893). Some Physical Properties of Sands and Gravels with Special Reference to their Use in Filtration. 34, p. 539-556. Massachusetts State Bureau of Health, Publ. Doc.
- Head, K. (1982). *Manual of soil laboratory testing* Vol. 2. Pentech Press.
- Hördt, A., Blaschek, R., Kemna, A., & Zisser, N. (2007). Hydraulic conductivity estimation from induced polarisation data at the field scale - the Krauthausen case study. *Journal of Applied Geophysics*, 62, p. 33-46.
- Huntley, D. (1986). Relations between permeability and electrical resistivity in granular aquifers. *Groundwater*, 24, p. 446-474.
- Jougnot, D., Ghorbani, A., Revil, A., Leroy, P., & Cosenza, P. (2010). Spectral induced polarization of partially saturated clay rocks: a mechanistic approach. *Geophys. J. Int.*, 180, p. 210-224.
- Jougnot, D., Revil, A., & Leroy, P. (2009). Diffusion of ionic tracers in the Callovo-Oxfordian clay-rock using the Donnan equilibrium model and the formation factor. *Geochimica et Cosmochimica Acta*, 73, p. 2712-2726.
- Keller, G. (1953). Effect of wettability on the electrical resistivity of sand. *Oil and Gas Journal*, 51, p. 62-65.
- Kemna, A. (2000). *Tomographic inversion of complex resistivity - theory and application*, Ph.D. thesis. Bochum Ruhr-Univ., Germany.
- Kemna, A., Binley, A., & Slater, L. (2004). Crosshole IP imaging for engineering and environmental applications. *Geophysics*, 69, p. 97-107.
- Kemna, A., Binley, A., Ramirez, A., & Daily, W. (2000). Complex resistivity tomography for environmental applications. *Chem. Eng. J.*, 77, p. 11-18.
- Kemna, A., Münch, H., Titov, K., Zimmermann, E., & Vereecken, H. (2005). Relation of SIP relaxation time of sands to salinity, grain size and hydraulic conductivity: 4pp. *Extended Abstracts: Near Surface 2005 - 11th European Meeting of Environmental and Engineering Geophysics P054*.
- Kemna, A., Räckers, E., & Dresen, L. (1999). Field application of complex resistivity tomography. *Proceedings of the 69th Annual International Meeting*. p. 331-334. Society of Exploration Geophysics, Expanded Abstracts.
- Klein, J., & Sill, W. (1982). Electrical properties of artificial clay bearing sandstones. *Geophysics*, 47, p. 1593-1605.
- Kormiltsev, V. (1963). O vzbuzhdenii i spade vyzv annoy polarizatsii v kapilliarnoi srede (On the excitation and decay of induced polarization in a capillary medium). (In Russian.). *Sov. Solid Earth Phys.*, 11, p. 1658-1666.
- Kosinski, W., & Kelly, W. (1981). Geoelectrical soundings for predicting aquifer properties. *Ground Water*, 19, p. 163-171.

- Kruschwitz, S. (2008). *Assessment of the complex resistivity behaviour of salt affected building materials: Ph.D. diss.* Federal Institute for Materials Research and Testing (BAM), Germany.
- Kruschwitz, S., Binley, A., Lesmes, D., & Elshenawy, A. (2010). Textural controls on low-frequency electrical spectra of porous media. *Geophysics*, 75(4), p. 113-123.
- Lambot, S., Slob, E., Rhebergen, J., Lopera, O., Jadoon, K., & Vereecken, H. (2009). Remote estimation of the hydraulic properties of a sand using full-waveform integrated hydrogeophysical inversion of time-lapse, offground GPR data. *Vadose Zone J.*, 8, p. 743-754.
- Leij, F. J., Russell, W. B., & Lesch, S. M. (1997). Closed-Form Expressions for Water Retention and Conductivity Data. *Groundwater*, 35, p. 848-858.
- Leroy, P., Revil, A., Altmann, S., & Tournassat, C. (2007). Modeling the composition of the pore water in a clay rock geological formation (Callovo-Oxfordian, France). *Geochimica et Cosmochimica Acta*, 71, p. 1087-1097.
- Leroy, P., Revil, A., Kemna, A., Cosenza, P., & Ghorbani, A. (2008). Complex conductivity of water-saturated packs of glass beads. *J. Colloid Interface Sci.*, 321, p. 103-117.
- Lesmes, D., & Frye, K. (2001). Influence of pore fluid chemistry on the complex conductivity and induced polarization responses of Berea sandstone. *Journal of Geophysical Research*, 106, p. 4079-4090.
- Lesmes, D., & Morgan, F. (2001). Dielectric spectroscopy of sedimentary rocks. *J. Geophys. Res.*, 106, p. 13329-13346.
- Lyklema, J. (1995). *Fundamentals of Interface and Colloid Science*. London, U.K.: Elsevier.
- Lyklema, J. (2002). Specificity in the statics and dynamics of surface-confined ions. *Molecular Physics*, 100, p. 3177-3185.
- Madden, T., & Cantwell, T. (1967). Induced polarization, a review. *Mining geophysics 2*, p. 373-400.
- Marquardt, D. (1963). An Algorithm for least-squares estimation of nonlinear parameters. *Journal of the Society for Industrial and Applied Mathematics*, 11(2), p. 431-441.
- Maxwell, J. (1893). *Treatise on Electricity and Magnetism* 2nd ed., Oxford: Clarendon.
- Mboh, C., Huisman, J., & Vereecken, H. (2011). Feasibility of Sequential and Coupled Inversion of Time Domain Reflectometry Data to infer soil hydraulic parameters under falling head infiltration. *Soil Science Society of America Journal*, 75, p. 775-786.
- Morgan, F., & Lesmes, D. (1994). Inversion for dielectric relaxation spectra. *J. Chem. Phys.*, 100, p. 671-561.
- Morrison, R. (1998). *Grounding and shielding techniques*. New York: John Wiley & Sons.
- Mualem, Y. (1976). A new model for predicting the hydraulic conductivity of unsaturated porous media. *Water Resources Research*, 12, p. 513-522.
- Münch, H., Kemna, A., Herbst, M., Zimmermann, E., & Vereecken, H. (2005). Multi-step outflow experiments to link soil hydraulic properties with electrical characteristics. *Proc. Workshop on HYDRUS Applications*, 19, p. 42-45. held at Dept. of Earth Sciences, Utrecht Univ., October.
- Nordsiek, S., & Weller, A. (2008). A new approach to fitting induced polarization spectra. *Geophysics*, 73, p. F235-F245.
- O'Konski, C. (1960). Electrical properties of macromolecules V. *Theory of ionic polarization in polyelectrolytes*, p. 605-619.
- Olhoeft, G. (1985). Low-frequency electrical properties. *Geophysics*, 50, p. 2492-2503.
- Pape, H., & Vogelsang, D. (1996). Fractal evaluation of induced polarization logs in the KTB-Oberpfalz HB. *Geologisches Jahrbuch*, 54(E), p. 3-27.
- Pape, H., Riepe, L., & Schopper, J. (1982). A pigeon-hole model for relating permeability to specific surface. *The Log Analyst*, 23, p. 5-13.

- Pape, H., Riepe, L., & Schopper, J. R. (1987). Interlayer conductivity of rocks - A fractal model of interface irregularities for calculating interlayer conductivity of natural porous mineral systems. *Colloids and Surfaces*, 27, p. 97-122.
- Pelton, W., Ward, S., Hallof, P., Sill, W., & Nelson, P. (1978). Mineral discrimination and removal of inductive coupling with multifrequency IP. *Geophysics*, 43, p. 588-609.
- Press, W., Teukolsky, S., Vetterling, W., & Flannery, B. (1992). *Numerical recipes in FORTRAN the art of scientific computing*. Cambridge University Press.
- Purvance, D., & Andricevic, R. (2000). On the electrical hydraulic conductivity correlation in aquifers. *Water Resources Research*, 36, p. 2905-2913.
- Revil, A., & Florsch, N. (2010). Determination of permeability from spectral induced polarization in granular media. *Geophys. J. Int.*, 181, p. 1480-1498.
- Revil, A., & Linde, N. (2006). Chemico-electromechanical coupling in microporous media. *Journal of Colloid and Interface Science*, 302(2), p. 682-694.
- Revil, A., Karoulis, M., Johnson, T., & Kemna, A. (2012). Review: Some low-frequency electrical methods for subsurface characterization and monitoring in hydrogeology. *Hydrogeology Journal*, 20, p. 617-658.
- Revil, A., Linde, N., Cerepi, A., Jougnot, D., Matthai, S., & Finsterle, S. (2007). Electrokinetic coupling in unsaturated porous media. *J. Colloid Interface Sci.*, 313, p. 315-327.
- Richards, L. A. (1931). Capillary conduction of liquids through porous mediums. *Physics*, 1, p. 318-333.
- Rubin, Y., & Hubbard, S. (2005). *Hydrogeophysics*. P.O. Box 17, 3300 AA Dordrecht, The Netherlands: Published by Springer.
- Ruffet, C., Darot, M., & Gueguen, Y. (1995). Surface conductivity in rocks: a review. *Surveys in Geophysics*, 16, p. 83-105.
- Sanchez-Vila, X., Meier, P. M., & Carrera, J. (1999). Pumping tests in heterogeneous aquifers: An analytical study of what can be obtained from their interpretation using Jacob's method. *Water Resources Research*, 35, p. 943-952.
- Scheffer, & Schachtschabel. (2010). *Lehrbuch der Bodenkunde*. Heidelberg: Spektrum Akademischer Verlag.
- Schmutz, M., Revil, A., Vaudelet, P., Batzle, M., Femenia Vinao, P., & Werkema, D. (2010). Influence of oil saturation upon spectral induced polarization of oil-bearing sands. *Geophys. J. Int.*, 183, p. 211-224.
- Schwarz, G. (1962). A theory of the low frequency dielectric dispersion of colloidal particles in electrolyte solutions. *J. Phys. Chem.*, 66, p. 2636-2642.
- Scott, J., & Barker, R. (2003). Determining throat size in Permo-Triassic sandstones from low frequency electrical spectroscopy. *Geophysical Research Letters*, 30.
- Scott, J., & Barker, R. (2005). Characterization of sandstone by electrical spectroscopy for stratigraphical and hydrogeological investigations. *Q J Eng Geol Hydrogeol*, 38, p. 143-153.
- Scott, J., & Barker, R. (2006). Pore geometry of Permo-Triassic sandstone from measurements of electrical spectroscopy. In R. Barker, & J. Tellam (Hrsg.), *Fluid Flow and Solute Movement in Sandstones: The Onshore UK Permo-Triassic Red Bed Sequence*, 263, p. 65-81. London: Geological Society, London, Special Publications.
- Sen, P. (1997). Resistivity of partially saturated carbonate rocks with microporosity. *Geophysics*, 62, p. 415-425.
- Shepherd, R. (1989). Correlations of permeability and grain size. *Ground Water*, 27(5), p. 633-638.
- Simunek, J., van Genuchten, M., & Sejna, M. (2005). *HYDRUS-1D, V3.00, Code for simulating the one dimensional movement of water, heat and multiple solutes in variably-saturated porous media*. Riverside, USA.

- Simunek, J., Wendroth, O., & van Genuchten, M. (1999). Estimating unsaturated soil hydraulic properties from laboratory tension disc infiltrometer experiments. *Water Resources Research*, 35, p. 2965-2979.
- Slater, L. (2006). Near Surface electrical characterization of hydraulic conductivity from petrophysical properties to aquifer geometries - a review. *Surv. Geophys.*, 28, p. 169-197.
- Slater, L. (2007). Near surface electrical characterization of hydraulic conductivity: From petrophysical properties to aquifer geometries - A review. *Surv. Geophys.*, 28, p. 169-197.
- Slater, L., & Binley, A. (2006). Synthetic and field based electrical imaging of a zerovalent iron barrier: implications for monitoring long-term barrier performance. *Geophysics*, 71, p. B129-137.
- Slater, L., & Lesmes, D. (2002). Electrical-hydraulic relationships observed for unconsolidated sediments. *Water Resources Research*, 38, p. 3101-3110.
- Slater, L., Ntarlagiannis, D., & Wishart, D. (2006). On the relationship between induced polarization and surface area in metal-sand and clay-sand mixtures. *Geophysics*, 71, p. A1-A5.
- Sweeney, S., & Jennings, H. (1960). Effect of wettability on the electrical resistivity of carbonate rock from a petroleum reservoir. *Journal of Physical Chemistry*, 64, p. 551-553.
- Titov, K., Kemna, A., Tarasov, A., & Vereecken, H. (2004). Induced polarization of unsaturated sands determined through Time Domain Measurements. *Vadose Zone Journal*, 3, Article Number. 11601168.
- Titov, K., Komarov, V., Tarasov, V., & Levitski, A. (2002). Theoretical and experimental study of time domain induced polarization in water saturated sands. *J. Appl. Geophys.*, 50, p. 417-433.
- Ulrich, C., & Slater, L. (2004). Induced polarization measurements on unsaturated, unconsolidated sands. (Geophysics, Hrsg.) *Geophysics*, 69, p. 762-771.
- van Dam, J. C., Stricker, J. M., & Droogers, P. (1994). Inverse method for determining soil hydraulic functions from multi step outflow experiments. *Soil Sci. Soc. Am. J.*, 58, p. 647-652.
- Van Genuchten, M. (1980). A closed-form equation for predicting the hydraulic conductivity of unsaturated soils. *Soil Sci. Soc. Am. J.*, 44, p. 892-898.
- van Genuchten, M. T. (1980). A closed form equation for predicting the hydraulic conductivity of unsaturated soils. *Soil Sci. Soc. Am. J.*, 44, p. 892-898.
- Vanhala, H. (1997). Mapping oil-contaminated sand and till with the spectral induced polarization (SIP) method. *Geophys. Prosp.*, 45, p. 303-326.
- Vaudelet, P., Revil, A., Schmutz, M., Franceschi, M., & Begassat, P. (2011a). Changes in induced polarization associated with the sorption of sodium, lead, and zinc on silica sands. *Journal of Colloid and Interface Science*, 360, p. 739-752.
- Vaudelet, P., Revil, A., Schmutz, M., Franceschi, M., & Begassat, P. (2011b). Induced polarization signatures of cations exhibiting differential sorption behaviors in saturated sands. *Water Resources Research*, 47.
- Vereecken, H., Binley, A., Cassiani, G., Revil, A., & Titov, K. (2006). *Applied Hydrogeophysics*. P.O. Box 17, 3300 AA Dordrecht, The Netherlands: Published by Springer.
- Vereecken, H., Kemna, A., Tillmann, A., Vanderborght, J., & Verweerd, A. (2005). Hydrogeophysical characterization of subsurface solute transport at the Krauthausen test site: experiments and numerical modeling. In G. Nutzmann, P. Viotti, & Aagaard (eds.), *In: Reactive Transport in Soil and Groundwater - Processes and Models*, p. 221-237. Springer.

- Vereecken, H., Weynants, M., Javaux, M., Pachepsky, Y., Schaap, M. G., & van Genuchten, M. T. (2010). Using Pedotransfer Functions to Estimate the van Genuchten - Mualem Soil Hydraulic Properties: A Review. *Vadose Zone Journal*, 9, p. 795-820.
- Vinegar, H., & Waxman, M. (1984). Induced polarization of shaly sands. *Geophysics*, 49(9), p. 1267-1287.
- Wagner, K. (1924). Erklärung der Dielektrischen Nachwirkungsvorgänge aufgrund Maxwellscher Vorstellungen. *Arch. Electrotech.*, 2, p. 371-381.
- Waxman, M., & Smits, L. (1968). Electrical conductivities in oil bearing shaly sands. *Soc. Petroleum Eng. J.*, 8, p. 107-122.
- Weller, A., Breede, K., Slater, L., & Nordsiek, S. (2011). Effect of changing water salinity on complex conductivity spectra of sandstones. *Geophysics*, 76(5), p. 315-327.
- Weller, A., Slater, L., Nordsiek, S., & Ntarlagiannis, D. (2010). On the estimation of specific surface per unit pore volume from induced polarization: A robust empirical relation fits multiple data sets. *Geophysics*, 75.
- Williams, K., Kemna, A., Wilkins, M., Druhan, J., Arntzen, E., N'Guessan, A., et al. (2009). Geophysical monitoring of coupled microbial and geochemical processes during stimulated subsurface bioremediation. *Environ. Sci. Technol.*, 43, p. 6717-6723.
- Wong, J. (1979). An electrochemical model of the induced-polarization phenomenon in disseminated sulphide ores. *Geophysics*, 44(7), p. 1245-1265.
- Worthington, P., & Collar, F. (1984). Relevance of induced polarization to quantitative formation evaluation. *Marine and Petroleum Geology*, 1, p. 14-26.
- Wösten, J., Pachepsky, Y., & Rawls, W. (2001). Pedotransfer functions: bridging the gap between available basic soil data and missing soil hydraulic characteristics. *Journal of Hydrology*, 251(3-4), p. 123-150.
- Zimmermann, E., Kemna, A., Berwix, J., Glaas, W., Münch, H., & Huisman, J. (2008). A high-accuracy impedance spectrometer for measuring sediments with low polarizability. *Meas. Sci. Technol.*, 19: 105603.
- Zisser, N., Kemna, A., & Nover, G. (2010). Relationship between low-frequency electrical properties and hydraulic permeability of low-permeability sandstones. *Geophysics*, 75, p. E131-E141.